Internal Tides and Resonance

by

Simon

S. Wotherspoon, B.Sc.(Hons)

in the Department of Mathematics

submitted in fulfilment of the requirements
for the degree of
Doctor of Philosophy.

graduated 1996

University of Tasmania

February, 1995.

I declare that this thesis contains no material which has been accepted for the award of any other higher degree or graduate diploma in any tertiary institution, and that, to the best of my knowledge and belief, this thesis contains no material previously published or written by another person, except when due reference is made in the text of the thesis.

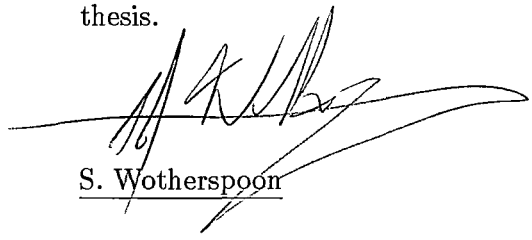

S. Wotherspoon

Abstract

This thesis is a study of resonant internal tide motion.

One common linear inviscid model represents the motion in terms of a two dimensional stream function satisfying a standard second order hyperbolic equation. This model is examined in detail and it is shown that existing solution techniques can be extended and unified with the classical theory of a single complex variable. This results in a number of new theoretical devices for the solution of the model, including *c-conformal mapping* — a mapping procedure that shares many of the traits of classical conformal mapping, and *c-analytic continuation* — a procedure for extending the domain of a solution analogous to standard analytic continuation.

These techniques are applied to a study of the model on closed basins. A crucial distinction relating to the geometry of the corners of the basin is noted, and the importance of energy sources and sinks is recognized. The analysis is found both to support the conjectures of other researchers that the existence of resonant motion may be predicted through an analysis of the characteristic coordinates of the inviscid model, and to demonstrate that the inviscid model is an inadequate vehicle for the study of internal tides on basin topographies.

A viscous form of the linear model is then discussed and a number of numerical solution techniques suitable for basin topographies are devised. The first of these is a straightforward application of standard collocation methods, but is found to be computationally expensive. A simpler, more efficient family of techniques based on the theory of c-analytic continuation is then derived. These methods are seen to be a natural extension of a Fourier series technique successfully employed by other authors.

The predictions of the linear models are then compared with the results of laboratory experiments. Resonance effects are seen to play a major role in determining the motion of the fluid. However, the strongly resonant motions predicted by the linear models are not observed, and, in general, the agreement between model and data is poor. This is attributed to both the sensitivity of the problem and the difficulty associated with modelling the external forcing.

The large amplitude strongly resonant motions predicted by the linear models prompt a study of nonlinear internal tide dynamics. A nonlinear model based on the Navier Stokes equations is considered, and numerical solutions are obtained via finite differences. These solutions show that for strongly resonant motion the "Rigid Lid" approximation commonly imposed at the free surface is inadequate and must be replaced with a more accurate nonlinear boundary condition.

Acknowledgements

I would like to express my sincere gratitude to John Donaldson and Peter Craig for their patience and guidance during the course of this work. I have received much support and encouragement from the entire Mathematics Department of the University of Tasmania, but I would especially like to thank both David Paget and Tim Stokes for many interesting and illuminating discussions. I would also like to thank Bruce Brown and Desmond Fearnley Sander for their consistent support, Kym Hill for his valuable technical assistance, and Tim Lamb for all the hangovers.

Contents

Chapter 1

Introduction

Internal tides, that is, internal waves of tidal frequency, were first observed by Helland–Hansen and Nansen in 1909 in the Norwegian Sea (Baines[2]). Internal tides have since been observed in numerous locations, and are often found to constitute a dominant feature of the water motion over continental shelves and slopes. However, due to the relatively short spatial scale of internal tides, obtaining detailed observational data is both difficult and expensive, hence the importance of mathematical models of this phenomena.

Theoretical models of internal tide motion have been based largely on the assumption of a two–dimensional, linear, inviscid motion.

The first theoretical study of internal tide generation was undertaken by Rattray[39], who examined the generation of internal tides at a stepped shelf in terms of a two layer model.

Subsequent investigations have largely involved a continuously stratified fluid, and a variety of approaches have been taken. Several authors, notably Larsen[28], Rattray, Dworski and Kovala[40] and Prinsenberg and Rattray[38], have employed a Fourier series method, however this procedure is limited to topographies that are piecewise linear. Sandstrom[41] extends this approach to more general topographies, by using a more sophisticated series representation based on the theory of

characteristics. The method of Baines[1, 2, 3] is also based on characteristics, and involves recasting the problem in terms of a Fredholm integral equation. A third procedure based on characteristics is that of Craig[14, 13], who numerically integrates along the characteristics co–ordinates of the system. Other authors have taken a more traditional finite difference approach, amongst these are Chuang and Wang[9], Cushman–Roisin *et al.*[17] and Tverberg *et al.*[45].

These theoretical studies of internal tide motion have largely concentrated on the generation of internal tides at the continental slope, where internal tides are believed to be generated through the interaction of the surface tide and the bottom topography. As Baines[2] describes, "The motion of the surface tide over bottom topography creates horizontal density gradients in the stratified ocean which are unbalanced, and therefore act to generate internal waves of the same frequency".

An important aspect of the internal tide problem is the so–called "radiation condition". Since only a finite segment of the shelf topography is considered, an appropriate boundary condition must be imposed at the two lateral boundaries open to the ocean (see Figure 1.1). Lighthill[31] has shown the appropriate condition is a radiation condition, which requires that at this boundary the baroclinic component of the motion must consist only of waves with an outwardly directed group velocity. This ensures that all of the observed baroclinic motion has been generated within the region, as opposed to having propagated in through a lateral boundary.

The primary thrust of this current work derives from the work of Cushman–Roisin*et al.*[17] on internal tide motion in a fjord.

In modelling the fjord, Cushman–Roisin *et al.*[17] ignore the radiation condition altogether, and instead treat the mouth of the fjord as a reflecting boundary. In effect, the fjord is modelled as a closed basin. These authors attempt to model the fjord with a common inviscid model of internal tide motion, but encounter serious difficulties in obtaining numerical solutions to the model, and find it nec-

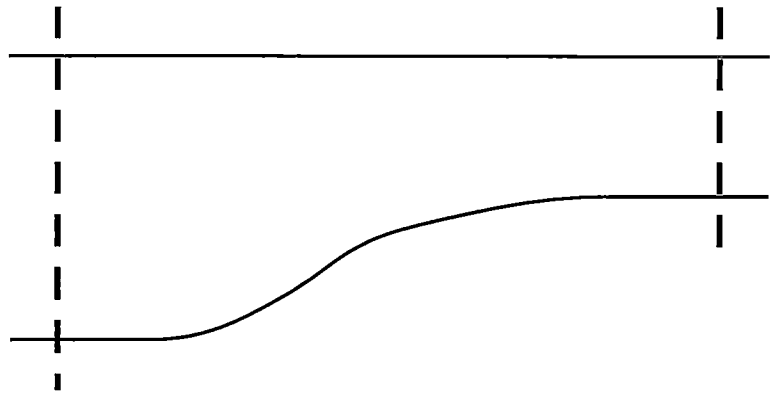

Figure 1.1: When modelling a shelf topography, only a finite segment of the topography is considered and an appropriate boundary condition must be imposed at the lateral boundaries (dashed).

essary to re–introduce viscous terms to ensure the convergence of their numerical method. They attribute these difficulties to the existence of resonant solutions, and conjecture that certain configurations of characteristics give rise to resonant solutions.

This thesis investigates the work of Cushman–Roisin *et al.*[17] in more detail, examining the behaviour of both inviscid and viscous models on basin topographies. This necessitates the development of several new analytic and numerical techniques for the internal tide problem, as many of the existing theoretical tools derive from studies of an inviscid model posed on a shelf topography and are unsuited to a study of basin topographies. Furthermore, is shown that the common linear models of internal tide motion break down for strongly resonant motions, prompting a study of nonlinear internal tide dynamics.

To obtain data against which the performance of the various models may be evaluated, a number of laboratory experiments were conducted. Correspondingly, many of the procedures developed here are primarily geared towards reproducing the results of the laboratory experiments, rather than to a more general oceanographic context. So for example, as Coriolis effects are negligible on the time scale

of the laboratory experiments, these are largely neglected throughout. Furthermore, it is to be intuitively expected that any complete description of resonant internal tide motion must account for three dimensional effects, but for simplicity, the scope of the current work is restricted to two dimensional models. While this is almost certainly not the full picture, it is nonetheless, a beginning.

The thesis is structured as follows.

Chapter 2 derives from the Navier Stokes equations, the four major models of internal tide motion considered in later chapters. This serves to both consolidate notation and to show the inter–relations between the four models.

The simplest of the four models is common in the literature, and describes the motion in terms of a standard two dimensional linear hyperbolic equation. Chapter 3 considers the basic properties of this model, laying the theoretical foundation on which subsequent chapters build. This chapter develops a new body of theory that extends the methods of Craig[14, 13] and Sandstrom[41], unifying these with the classical theory of a single complex variable. In particular, two major tools are developed:

- c–analytic continuation, a method for extending the domain of definition of a solution of the inviscid model, analogous to the analytic continuation of a harmonic function, and

- c–conformal mapping, a general mapping procedure under which the form of the inviscid model remains invariant, analogous to the conformal mapping of Laplace's equation.

The next three chapters all rely upon the theory of Chapter 3, but to a large degree are mutually disjoint and may be read independently.

Chapter 4 is a detailed investigation of the inviscid model on basin topographies like that considered by Cushman–Roisin *et al.*[17]. It is immediately seen that this problem is not well posed and the need for a viscous model is recognized. In general the results of this chapter support the conclusions of Cushman–Roisin

et al.[17], although certain small inconsistencies are noted. Although it could be argued that this chapter is more detailed than necessary, it is this chapter that the author finds the most intriguing of all.

Chapter 5 examines an approximation employed by both Cushman–Roisin *et al.*[17] and Tverberg *et al.*[45] in implementing their respective finite difference schemes. It is first demonstrated that this approximation introduces numerical effects that can contaminate the physical solution, an alternative procedure based on c–conformal mapping is then proposed and a numerical method for generating the necessary c–conformal maps is devised. This new procedure has the advantage that it may be implemented as a preprocessing stage, allowing existing solution methods to be applied largely unaltered.

Motivated by the need to model the tank experiments, Chapter 6 develops and compares a number of new techniques for solving the viscous model of internal tide motion on a basin topography. The first of these is a straightforward application of collocation methods, but this method is found to be computationally expensive. Following this a variety of more efficient methods based on the theory of c–analytic continuation and a perturbation technique due to Craig[16] are devised. Craig's method is a two stage process. The first stage seeks only to model viscous effects at the boundary, with viscous effects through the water column being modelled in the second stage of the procedure. A successful method based on the first stage of Craig's method is devised, but it is found that the second stage of Craig's process is flawed, and an alternative technique is devised to represent viscous effects in the water column.

Chapter 7 then applies these methods to modelling the tank experiments. The results of this comparison establish the importance of resonance and indicate the need for a non–linear model of internal tide motion. This taken up in Chapter 8 where a finite difference method is used to compare a non–linear model with its linear counterpart.

Finally, the thesis concludes with brief summary of the major results in Chap-

ter 9.

Chapter 2

Derivation of Equations

In the absence of Coriolis effects, internal tide motion may be completely described by the two dimensional incompressible Navier Stokes Equations. However, due to the intractable nature of the Navier Stokes equations, it is common to introduce a series of approximations to reduce the equations to a more amenable form. This chapter derives from the Navier Stokes equations the major models of internal tide motion discussed in subsequent chapters.

2.1 The Incompressible Navier Stokes Equations

Using alphabetic subscripts to denote differentiation, in two dimensions the incompressible Navier Stokes equations(Landau and Lifschitz[27])) may be written

$$u_t + uu_x + wu_z = -\frac{p_x}{\rho} + \nu\nabla^2 u \tag{2.1}$$

$$w_t + uw_x + ww_z = -\frac{p_z}{\rho} + \nu\nabla^2 w - g \tag{2.2}$$

$$\rho_t + u\rho_x + w\rho_z = 0 \tag{2.3}$$

$$u_x + w_z = 0, \tag{2.4}$$

where p, ρ, g, u and w denote respectively the pressure, density, gravitational acceleration, and the horizontal and vertical components of fluid velocity, and it

has been assumed that the z ordinate is oriented vertically.

These equations must be supplemented by an appropriate set of boundary conditions. At a solid boundary these conditions amount to a zero flux boundary condition plus an appropriate frictional condition. Let $\underline{v} \equiv (u, w)$ denote the vector velocity, and $\underline{t}$ and $\underline{n}$ denote respectively the unit tangent and unit normal vectors at a point p on the boundary. Then the first of these conditions can be expressed as

$$\underline{v} \,.\, \underline{n} = 0, \tag{2.5}$$

representing the fact that there can be no flow through a solid boundary. In relation to the tank experiments, two forms of frictional boundary condition will be considered: a zero slip condition

$$\underline{v} \,.\, \underline{t} = 0, \tag{2.6}$$

where the tangential component of velocity vanishes at the boundary representing a perfectly adhesive interaction between fluid and surface, and a zero stress condition

$$\nabla(\underline{v} \,.\, \underline{t}) \,.\, \underline{n} \equiv \frac{\partial}{\partial n}(\underline{v} \,.\, \underline{t}) = 0, \tag{2.7}$$

where the normal derivative of the tangential component of velocity vanishes at the boundary representing an idealized interaction that is perfectly frictionless. For oceanographic applications a linear slip condition (Brink[6]) is more appropriate.

As the normal component of velocity will vanish at a solid boundary, Equation (2.3) requires no boundary condition.

Neglecting frictional and surface tension effects, at the fluid/atmosphere interface – the so called "free surface", the boundary conditions are given by (LeBlond and Mysak[30])

$$\zeta_t + u\zeta_x = w \qquad \text{on } z = \zeta(x, t), \tag{2.8}$$

where $z = \zeta(x,t)$ represents the position of the free surface. This condition expresses the fact that the position of the free surface is determined solely by the fluid velocity there, and implies that a parcel of fluid that initially lies on the surface must remain on the surface. Thus for a fluid that is initially only stratified in the vertical direction, the density boundary condition at the free surface must be

$$\rho = \rho_0(\zeta_0) \qquad \text{on } z = \zeta(x,t), \tag{2.9}$$

where $\rho_0(z)$ represents the hydrostatic density distribution, and ζ_0 represents the position of the free surface when the fluid is at rest. This must be further supplemented by a zero stress condition indicating the absence of frictional stresses from the atmosphere, and the obvious pressure condition

$$p = p_{atmospheric} \qquad \text{on } z = \zeta(x,t). \tag{2.10}$$

Equations (2.1) – (2.4) together with the boundary conditions (2.5) – (2.10) constitute one of two models of internal tide motion that will be considered in Chapter 8.

2.2 Linearized Navier Stokes Equations

To reduce the above equations to a more amenable form, it is first assumed that the amplitude of the motion is small. This allows the model to be linearized through a straightforward perturbation expansion.

Consistent with the assumption of a small amplitude motion, the quantities

u, w, p, ρ and ζ are expanded in the form

$$u = \epsilon u_1 + O(\epsilon^2) \tag{2.11}$$

$$w = \epsilon w_1 + O(\epsilon^2) \tag{2.12}$$

$$p = p_0 + \epsilon p_1 + O(\epsilon^2) \tag{2.13}$$

$$\rho = \rho_0 + \epsilon \rho_1 + O(\epsilon^2) \tag{2.14}$$

$$\zeta = \zeta_0 + \epsilon \zeta_1 + O(\epsilon^2) \tag{2.15}$$

where ϵ is a small parameter related to the amplitude of the motion. Substituting (2.11) – (2.15) into (2.1) – (2.8) and equating coefficients of ϵ^0 leads to the familiar hydrostatic equations

$$0 = p_{0x} \tag{2.16}$$

$$0 = p_{0z} - \rho_0 g \tag{2.17}$$

plus the condition at the free surface that

$$\zeta_{0t} = 0. \tag{2.18}$$

Similarly, equating coefficients of ϵ^1 in (2.1) – (2.4) leads to the linearized Navier Stokes equations

$$\rho_0 u_t = -p_x + \nu \rho_0 \nabla^2 u \tag{2.19}$$

$$\rho_0 w_t = -p_z + \nu \rho_0 \nabla^2 w - \rho' g \tag{2.20}$$

$$\rho'_t + w\rho_{0z} = 0 \tag{2.21}$$

$$u_x + w_z = 0, \tag{2.22}$$

where numeric subscripts on u_1, w_1 and p_1 have been dropped for convenience, and ρ_1 has been rewritten as the more notationally conventional ρ'.

Taking Taylor expansions and equating coefficients of ϵ^1, the free surface

conditions (2.10) – (2.10) reduce to

$$\zeta_t = w \qquad \text{on } z = \zeta_0 \tag{2.23}$$

$$p_t = -p_{0z}\zeta \qquad \text{on } z = \zeta_0 \tag{2.24}$$

$$\rho_t = -\rho_{0z}\zeta \qquad \text{on } z = \zeta_0, \tag{2.25}$$

where again, numeric subscripts on w_1 and ζ_1 have been dropped for notational convenience.

It common to simplify the surface conditions even further, requiring that the baroclinic component of the motion satisfy the more stringent

$$w = 0 \qquad \text{on } z = \zeta_0, \tag{2.26}$$

so that w on $z = \zeta_0$ is determined entirely by the barotropic forcing. This is called the "Rigid Lid Approximation", and must be justified by noting that the wavelength of surface tides is much longer than the wavelength of internal tides of the same frequency (Gill[21]). This approximation corresponds to replacing the upper free surface with a "rigid lid", so that the effects of surface elevation are then represented as pressure and density fluctuations at the new fixed surface.

Equations (2.19) – (2.22) together with the rigid lid condition (2.26) and appropriate boundary conditions at the solid boundaries constitute the second model of internal tide motion that will be considered in Chapter 8.

2.3 The Wave Equation

Equations (2.19) – (2.22) may be further reduced to a single fifth order equation expressed in terms of a stream function $\Psi(x, z, t)$.

Eliminating terms in p and ρ from (2.19) – (2.21) yields

$$\rho_0(w_{xtt} - u_{ztt}) - g\rho_{0z}w_{xt} = \nu\rho_0\nabla^2(w_{xt} - u_{zt}), \tag{2.27}$$

where terms involving ρ_{0z} and u have been neglected under the Boussinesq approximation(Spiegel and Veronis[42]), which states that density variations are

small in relation to inertial effects, but must be retained in terms pertaining to buoyancy.

The complete system of equations describing the motion now consists of equations (2.27), (2.22) and (2.26) together with the boundary conditions at the solid boundaries. These equations may be simplified further by introducing the time dependent stream function $\Psi(x, z, t)$ defined by

$$u = -\Psi_z \qquad w = \Psi_x, \tag{2.28}$$

and the Buoyancy or Brunt-Väisälä frequency N defined by

$$N^2 = -\frac{\rho_{0z}}{\rho_0} g. \tag{2.29}$$

Applying these definitions to (2.27) yields

$$\nabla^2 \Psi_{tt} + N^2 \Psi_{xx} = \nu \nabla^4 \Psi_t. \tag{2.30}$$

Note that equation (2.22) is satisfied automatically as a result of (2.29).

If it is assumed that the motion is temporally periodic, a time independent stream function $\psi(x, z)$ may be introduced, defined by

$$\Psi(x, z, t) = e^{-i\omega t} \psi(x, z) \tag{2.31}$$

and equation (2.30) reduces to

$$(N^2 - \omega^2)\psi_{xx} - \omega^2 \psi_{zz} = -i\omega\nu \nabla^4 \psi. \tag{2.32}$$

To formulate the boundary conditions in terms of ψ, again let $\underline{t}$ and $\underline{n}$ denote the unit tangent and unit normal vectors at a point p on the boundary, and let

$$\underline{k} = \underline{n} \times \underline{t}. \tag{2.33}$$

denote a unit vector perpendicular to both $\underline{t}$ and $\underline{n}$. Then (2.28) can be represented as

$$\underline{v} = \underline{k} \times \nabla \Psi \tag{2.34}$$

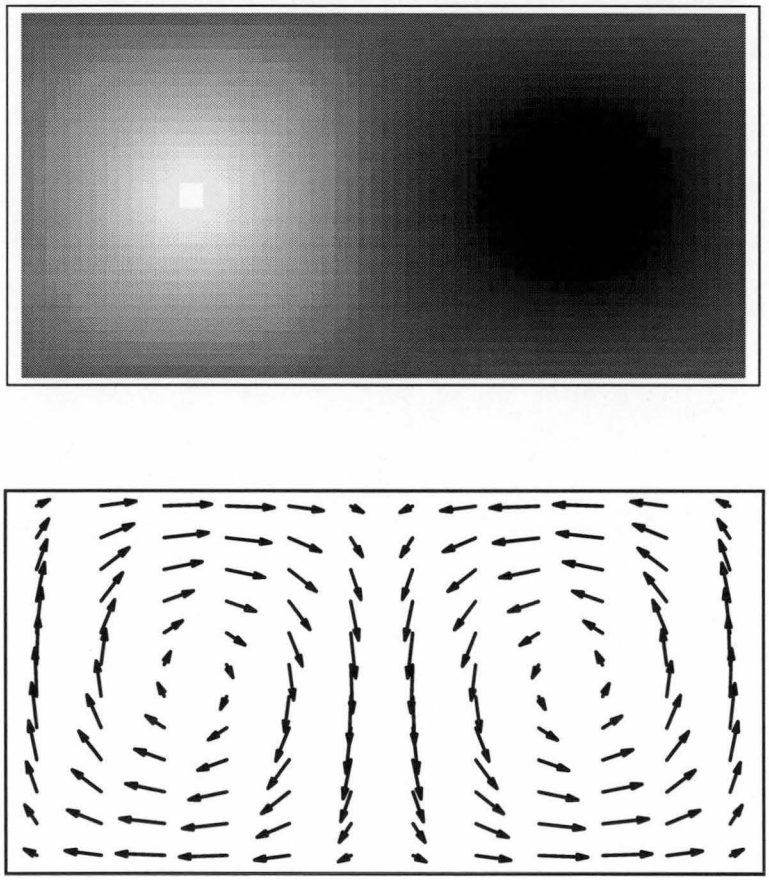

Figure 2.1: Interpretation of the time independent stream function. The upper diagram shows a density plot of $\psi(x, z) = \sin x \sin z$. The lower diagram shows the corresponding velocity field $(u, w) = (-\psi_z, \psi_x)$.

and the zero flux boundary condition (2.5) becomes

$$(\nabla\Psi) \,.\, \underline{t} = 0, \tag{2.35}$$

which can be integrated to yield

$$\Psi = a \tag{2.36}$$

on the boundary, where a is a constant usually chosen as zero.

Similarly, the zero slip condition (2.6) becomes

$$(\underline{k} \times \nabla\Psi) \,.\, \underline{t} \equiv \underline{n} \times \nabla\Psi = 0 \tag{2.37}$$

and the zero stress condition (2.7) becomes

$$\nabla(\nabla\Psi \,.\, \underline{n}) \,.\, \underline{n} \equiv \frac{\partial^2\Psi}{\partial n^2} = 0, \tag{2.38}$$

where $\partial/\partial n$ represents the directional derivative taken normal to the boundary. In view of (2.31), it is easily shown ψ satisfies a similar set of boundary conditions.

The final stage of the derivation involves a simple non–dimensionalization argument. For a shelf topography, the horizontal length scale is typically of the order of several hundred kilometres, while the maximum depth is of the order of one kilometre. For a fjord like that discussed by Cushman–Roisin *et al.*[17] and Tverberg *et al.*[45], the typical horizontal length scale is of the order of $30km$ while the maximum depth is of the order of $200m$. Thus performing a standard dimensional analysis it is found that the terms in Equation (2.32) scale such that

$$\psi_{zzzz} \gg \psi_{xxzz} \gg \psi_{xxxx}, \tag{2.39}$$

and that these terms are much smaller in magnitude than the other terms in the equation.

Thus for a shelf or fjord, the reduced equation

$$(N^2 - \omega^2)\psi_{xx} - \omega^2\psi_{zz} = -i\omega\nu\psi_{zzzz} \tag{2.40}$$

represents a good viscous approximation to (2.32), while a reasonable inviscid approximation is given by

$$\psi_{xx} - c^2\psi_{zz} = 0 \tag{2.41}$$

where

$$c^2 = \frac{\omega^2}{N^2 - \omega^2}. \tag{2.42}$$

In both these cases the corresponding viscous boundary conditions must be appropriately modified to suit the approximation.

The approximations taken in deriving Equations (2.41) and (2.40) are well founded for a shelf or fjord, but are much less justified for the tank experiments described in Chapter 7.2, where there is not such a large discrepancy in horizontal and vertical length scales. Nevertheless, these approximations will be adhered to for the sake of uniformity, and Equations (2.41) and (2.40) together with appropriate boundary conditions form the two major models of internal tide motion that will be considered in the first few chapters.

Finally, it should be noted that the inviscid model admits one small generalization. If Coriolis effects are incorporated into the model, the form of equation (2.41) remains invariant, except that c is now defined as

$$c^2 = \frac{\omega^2 - f^2}{N^2 - \omega^2}. \tag{2.43}$$

The details of this derivation may be found in Craig[14]. Unfortunately Coriolis effects can not be incorporated into the viscous models so easily.

This completes the derivation of the four main models of internal tide motion that will be discussed. The chapter concludes by introducing the radiation boundary condition.

2.4 The Radiation Boundary Condition

So far, only boundary conditions for a solid boundary or at the free surface have been considered. But when modelling the generation of internal tides at the continental slope, only a finite segment of the topography is considered and an appropriate boundary condition must be imposed at the lateral boundaries open to the ocean (see Figure 1.1).

Lighthill[31, 32] has shown that the appropriate boundary condition in this case is a radiation boundary condition, which requires that at these boundaries, the motion consist only of waves with an outwardly directed group velocity together with any external forcing. Thus energy can only enter the region through the external forcing, and any wave motion present at this boundary must have been generated within the region, rather than externally.

The most common implementation of this condition is a straightforward translation of the above. The motion at the boundary is resolved into a sum of travelling waves and it is required that only those waves with an outwardly directed group velocity be present in this sum. However, Baines[1, 2] presents an alternative formulation of the radiation condition based on certain invariance properties of the Hilbert transform.

Chapter 3

The Wave Equation

In the simplest model of inviscid internal tide motion derived in the previous chapter the motion is represented in terms of a stream function satisfying a standard two dimensional wave equation. This model has been studied by many authors in relation to internal tide motion near the continental shelf, and in this context is reasonably well understood. More recently however, several authors have attempted to apply this same model to internal tide motion in a basin. In this context the stream function must satisfy a wave equation formulated as a Dirichlet problem, and it has long been known that such problems are often not well posed (Tikhonov[44]). It is the primary purpose of this and the following chapter to investigate this simple model of inviscid internal tide motion and its application to basin topographies.

This chapter develops the theoretical framework used in later chapters to treat the inviscid internal tide problem. This framework is based on the theory of characteristics and the classical theory of a single complex variable, borrowing heavily from the techniques of Craig[14] and Sandstrom[41] for the solution of the internal tide problem on shelf topographies. In particular, three main tools are developed:

- a general solution of the two dimensional wave equation,

- a method of extending the domain of definition of these solutions similar to the analytic continuation of a harmonic function, and
- a general mapping procedure under which the form of the wave equation is invariant, analogous to the conformal mapping of Laplace's equation.

The chapter begins with a restatement of the model for the purpose of clarifying notation, and then a numerical solution of the inviscid internal tide problem for a stepped shelf topography is derived. This is an important example, for it exposes several of the subtler traits of the model and motivates much of the theory to be introduced in later sections.

Both the theory developed in this chapter and the techniques of Craig and Sandstrom stem from the theory of characteristics, and the chapter continues with a brief review of that component of the theory of characteristics germane to the inviscid internal tide problem. This leads naturally to a local form of the general solution of the wave equation, which is then extended to a global representation. This extension necessitates the introduction of several technical definitions that will play a major role in both this and subsequent chapters.

The next section introduces the methods of Craig and Sandstrom for shelf topographies. Craig's method follows almost immediately from the theory presented in the preceding section; Sandstrom's approach is more complicated, and only a relatively brief exposition is given.

Then follows the major component of the chapter. In this section an analogy is demonstrated between the methods of Craig and Sandstrom and the classical theory of a single complex variable. In particular, processes corresponding to analytic continuation and conformal mapping are derived, although it is demonstrated that these processes are not as powerful as their classical counterparts. The techniques described in this section form the basis of much of the analysis of subsequent chapters.

Throughout the chapter it is assumed that the buoyancy frequency of the fluid

is independent of depth, for this greatly simplifies the analysis of the characteristics. The chapter ends by briefly indicating how the theory may be extended to encompass the more general case in which the buoyancy frequency is a function of depth.

3.1 The Model

Consider an open region Ω with boundary $\partial\Omega$. As described in the previous chapter, inviscid internal tide motion on Ω may be described by a time independent stream function $\psi(x,z)$ satisfying the two dimensional wave equation

$$\psi_{xx} - c^2\psi_{zz} = 0, \tag{3.1}$$

where

$$c^2 = \frac{\omega^2 - f^2}{N^2 - \omega^2} \tag{3.2}$$

and ω is the tidal frequency, f the Coriolis parameter, N the Buoyancy frequency and x and z are Cartesian co-ordinates oriented in the onshore horizontal and vertical directions respectively. In general N and hence c are functions of z, but initially only the case of constant c is discussed, treatment of the more general case is deferred until later in the chapter.

The horizontal and vertical fluid velocities $u(x,z,t)$ and $w(x,z,t)$ corresponding to $\psi(x,z)$ are determined from the relations

$$u(x,z,t) = \Re\{-e^{-\imath\omega t}\psi_z(x,z)\}, \qquad w(x,z,t) = \Re\{e^{-\imath\omega t}\psi_x(x,z)\}, \tag{3.3}$$

where $\Re\{s\}$ denotes the real part of a complex value s.

At the upper surface of the fluid co-ordinates are chosen so that $z = 0$ represents the mean position of the free surface, and a "rigid lid" approximation (LeBlond and Mysak[30]) is adopted. The bottom topography is represented as $z = h(x)$, the bottom boundary condition being

$$\psi(x,h(x)) = 0, \tag{3.4}$$

while at the upper surface the appropriate condition is

$$\psi(x,0) = B(x,0), \tag{3.5}$$

where $B(x,z)$ represents the appropriate barotropic forcing.

At lateral boundaries open to the ocean it is required that ψ satisfy a radiation condition, that is, ψ must consist of an appropriate forcing function plus a sum of outgoing plane waves.

A region Ω will be described as a *shelf region* if it possesses at least one lateral radiating boundary open to the ocean and its bounding topography is monotonic, otherwise it will be described as a *basin*. A basin that possesses no lateral boundaries open to the ocean will be described as *closed*, in the sense that internal wave energy cannot radiate out of the region. This definition of a shelf region is clearly too restrictive, but will suffice for the purposes of the current work.

3.2 Solution for a Stepped Shelf

As a general introduction to the inviscid internal tide problem this section derives a numerical solution for a stepped shelf topography. This example highlights many features of the inviscid model as well as introducing one of the basic numerical techniques employed in later chapters.

The numerical solution is obtained via a boundary collocation method. The solution is represented as a linear combination of functions that satisfy (3.1) but not necessarily the appropriate boundary conditions. The coefficients in this sum are then chosen so that the boundary conditions are satisfied at some finite set of points on the boundary. This procedure is effectively the method of Rattray *et al.*[40], except that a collocation procedure replaces the Galerkin technique employed by those authors.

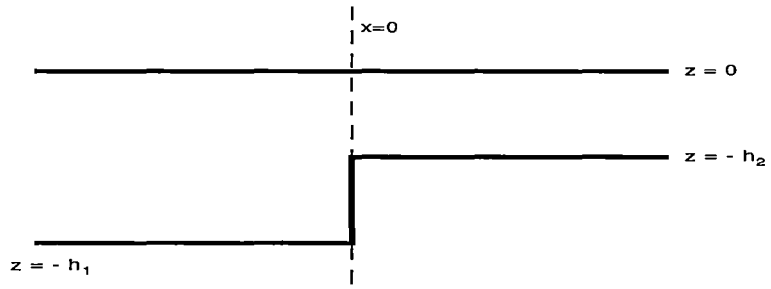

Figure 3.1: A stepped shelf.

Let the bottom topography of the shelf be defined by $z = h(x)$ where

$$h(x) = \begin{cases} -h_1 & \text{if } x < 0 \\ -h_2 & \text{if } x \geq 0 \end{cases} \tag{3.6}$$

and $h_1 > h_2 > 0$, as shown in Figure 3.1. The boundary conditions on ψ at the lower and upper boundaries are given by (3.4) and (3.5), with $B(x, z)$ taken as the barotropic forcing function derived by Craig[14]

$$B(x, z) = -i\omega\zeta_0(x - L)(1 - z/h(x)), \tag{3.7}$$

where ζ_0 represents the barotropic surface tidal amplitude at the coast $x = L$. On each of the regions $x < 0$ and $x > 0$ it is required that ψ satisfy the radiation condition. That is, on these regions ψ must be representable as a forcing component plus a sum of outgoing plane waves.

On the region $x < 0$ a solution of (3.1) satisfying all of the above conditions is given by

$$\psi_1(x, z) = -i\omega\zeta_0(x - L)(1 - z/h_1) + \sum_{n=1}^{\infty} a_n e^{-icn\pi x/h_1} \sin(n\pi z/h_1). \tag{3.8}$$

Similiarly, a solution satisfying the above conditions on $x > 0$ is given by

$$\psi_2(x, z) = -i\omega\zeta_0(x - L)(1 - z/h_2) + \sum_{n=1}^{\infty} b_n e^{icn\pi x/h_2} \sin(n\pi z/h_2). \tag{3.9}$$

In each of these expansions the first term represents the barotropic forcing function and the second a sum of outgoing plane waves, thus satisfying the radiation condition.

A solution valid on the entire region is obtained by matching these two solutions along $x = 0$. The a_n and b_n must be chosen such that the three conditions

$$\psi_1(0, z) = 0 \qquad \text{for } -h_1 \leq z \leq -h_2 \tag{3.10}$$

$$\psi_1(0, z) = \psi_2(0, z) \qquad \text{for } -h_2 < z < 0 \tag{3.11}$$

$$\psi_{1x}(0, z) = \psi_{2x}(0, z) \qquad \text{for } -h_2 < z < 0 \tag{3.12}$$

are satisfied. The first of these conditions enforces the bottom boundary condition (3.4) while the second and third conditions ensure the solution satisfies Equation (3.1) across the line segment $\{(0, z) \mid -h_2 < z < 0\}$.

In principle this leads to an infinite system of linear equations for the a_n and b_n. An approximate solution may be obtained via collocation. The collocation technique proceeds by approximating the expansions of ψ_1 and ψ_2 by truncated expansions and requiring the approximate solution to satisfy the boundary conditions at only a finite number of points on $x = 0$.

First ψ_1 and ψ_2 are approximated by the truncated forms

$$\psi_1(x, z) = -i\omega\zeta_0(x - L)(1 - z/h_1) + \sum_{n=1}^{N_1+N_2} a_n e^{-icn\pi x/h_1} \sin(n\pi z/h_1) \tag{3.13}$$

and

$$\psi_2(x, z) = -i\omega\zeta_0(x - L)(1 - z/h_2) + \sum_{n=1}^{N_2} b_n e^{icn\pi x/h_2} \sin(n\pi z/h_2). \tag{3.14}$$

Then a system of linear equations for the a_n and b_n is constructed by requiring that Condition (3.10) be satisfied at N_1 collocation points on the line segment $\{(0, z) \mid -h_1 < z < -h_2\}$ and that Conditions (3.11) and (3.12) be satisfied at N_2 collocation points on the segment $\{(0, z) \mid -h_2 < z < 0\}$. The resulting system of linear equations for the $N_1 + 2N_2$ coefficients may then be inverted by standard methods.

The accuracy of the method is dependent on the choice of the $N_1 + 2N_2$ collocation points. Given the simple nature of the boundary in the step problem, the obvious course is to distribute the collocation points evenly, with N_1 and N_2 chosen approximately in the ratio h_1/h_2. For more general topographies the optimal choice of collocation points is not so clear, proves to be a recurring difficulty.

Setting $c = 1$, $L = 5$, $h_1 = 2$ and $h_2 = 1$ results in the solution depicted in Figure 3.2. Note that the numerical solution appears to be converging to a function that is not continuously differentiable, and so the horizontal and vertical fluid velocities are not defined at every point in the domain. Not being twice differentiable, such a function cannot, in the classical sense, be considered a solution of Equation (3.1). Nevertheless, these functions represent useful idealizations, and will be examined in more detail in the following section.

3.3 The Theory of Characteristics

This section introduces the basic concepts of characteristic theory and develops the theoretical foundation on which the remainder of the chapter is constructed. The section begins by defining the characteristic co-ordinates of an arbitrary second order quasi linear partial differential equation. It is then demonstrated that in terms of its characteristic co-ordinates, Equation (3.1) may be easily integrated to yield an expression for its general solution. However, due to the manner in which the constants of integration are introduced there exist instances for which this solution will not suffice, and a corrected form of the solution is proposed. Finally, it is noted that when expressed in terms of its characteristic co-ordinates, Equation (3.1) admits additional solutions that are not sufficiently differentiable to be considered solutions of (3.1) in the classical sense. It is argued that this arises from the assumption of inviscid motion, and that in some instances such solutions may be considered idealized representations of viscous phenomena.

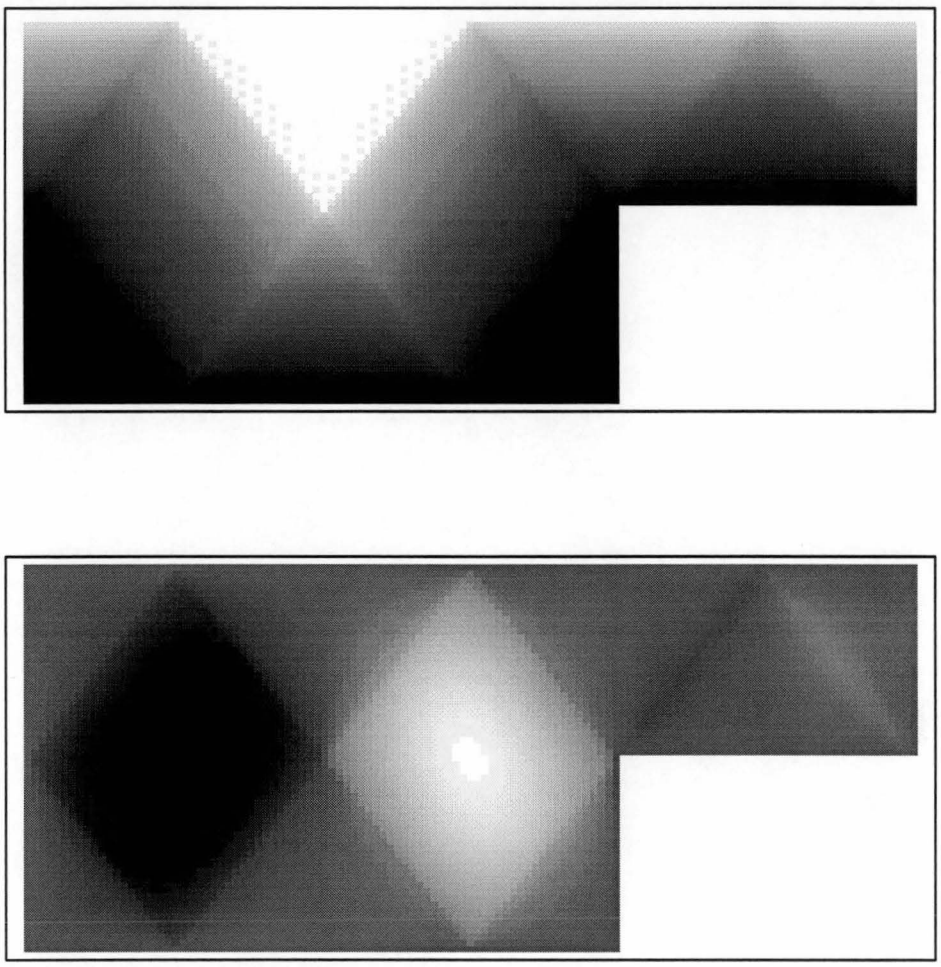

Figure 3.2: Solution of the inviscid internal tide problem for a stepped topography subject to a barotropic forcing of the form (3.7) with $h_1 = 1$, $h_2 = 0.5$, $c = 1$ and $L = 5$. The upper diagram depicts $\Re\{\psi\}$ and the lower diagram $\Im\{\psi\}$.

This leads to the notion of strong and weak solutions of Equation (3.1).

As described in Garabedian[20], a second order quasi-linear partial differential equation of the form

$$A(x,z)u_{xx} + B(x,z)u_{xz} + C(x,z)u_{zz} = F(u, u_x, u_z, x, z) \tag{3.15}$$

with F possibly non-linear, may be reduced to one of three canonical forms through the introduction of a new set of co-ordinates

$$\xi = \xi(x,z), \qquad \eta = \eta(x,z), \tag{3.16}$$

defined by the two first order equations

$$\frac{\eta_x}{\eta_z} = \frac{-B + \sqrt{B^2 - 4AC}}{2A}, \tag{3.17}$$

$$\frac{\xi_x}{\xi_z} = \frac{-B - \sqrt{B^2 - 4AC}}{2A}. \tag{3.18}$$

Definition 1 (Characteristics.). *The new co-ordinates $\xi(x,z)$ and $\eta(x,z)$ defined by Equations (3.17) and (3.18) are called the* characteristic co-ordinates *for Equation (3.15), and curves of constant ξ or η are called* characteristics. *When it is necessary to make the distinction, curves of constant ξ will be called C^+–*characteristics, *and curves of constant η will be called C^-–*characteristics.

There is a sense in which characteristics may be regarded as a natural co-ordinate system for (3.15). For a more complete discussion of the theory of characteristics the reader is referred to Jeffrey and Tanuiti[24].

If c is constant, the characteristic co-ordinates for Equation (3.1) are

$$\xi = x - z/c, \qquad \eta = x + z/c \tag{3.19}$$

and the corresponding characteristics are all lines in the xz plane with gradient $\pm c$. (Strictly, the characteristics are only defined in the region for which Equation (3.1) is defined, but for the purposes of this chapter the definition will be extended to the whole plane.)

Transforming to characteristic co-ordinates reduces Equation (3.1) to the canonical form

$$\psi_{\xi\eta} = 0. \tag{3.20}$$

In this form the equation may be immediately integrated to yield the general solution

$$\psi(\xi, \eta) = f(\xi) + g(\eta)$$

or equivalently in xz co-ordinates

$$\psi(x, z) = f(x - z/c) + g(x + z/c). \tag{3.21}$$

However, there exists an important class of topographies for which this solution fails to be sufficiently general. The solution obtained in the previous section (Fig. 3.2) provides a convenient example.

Consider Equation (3.20) defined on a region Ω for which there exist characteristics which intersect the boundary $\partial\Omega$ more than twice, such as depicted in Figure 3.3. Since ψ needs only satisfy (3.20) in Ω and the characteristic enters Ω more than once, it is permissible to introduce more than one constant of integration when integrating (3.20) along this characteristic. Thus in Figure 3.3 it is not necessary that $f(\xi)$ take the same value on AB as CD. This may be verified through an analysis of the solution for the stepped shelf (Fig. 3.2) derived in the previous section.

Denote the value of ψ at a point R by $\psi(R)$ and the value of a function f on a characteristic PQ by $f(PQ)$. Applying (3.21) to Figure 3.3 generates the following system of linear equations

$$f(AB) + g(FB) = \psi(B) \tag{3.22}$$

$$f(CD) + g(CE) = \psi(C) \tag{3.23}$$

$$f(EF) + g(CE) = \psi(E) \tag{3.24}$$

$$f(EF) + g(FB) = \psi(F). \tag{3.25}$$

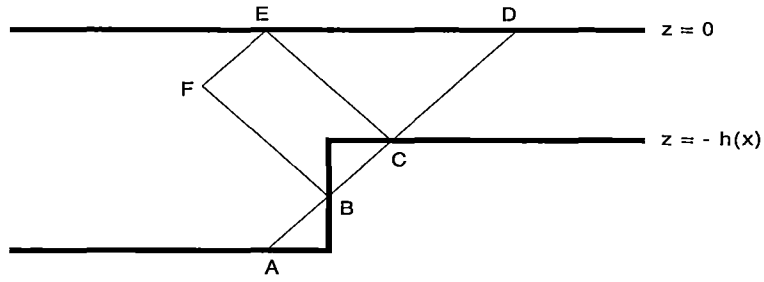

Figure 3.3: Extending characteristics through the boundary.

If $f(AB) = f(CD)$ then this set of linear equations may be solved to yield

$$\psi(F) = \psi(B) + \psi(E) - \psi(C). \tag{3.26}$$

Consider this identity in relation to the solution for the stepped topography obtained in the previous section. Since $\psi = 0$ on the bottom boundary the above condition implies $\psi(F) = \psi(E)$, but examination of Figure 3.2 shows that this is not the case. (This is most apparent from considering the imaginary component of the solution). Thus by contradiction $f(AB) \neq f(CD)$ and the solution shown in Figure 3.2 cannot be represented in the form (3.21).

It is clear then that the general solution (3.21) proposed above is too restrictive and must be amended, define:

Definition 2 (Characteristic Convexity). *A region Ω with boundary $\partial\Omega$ is said to be* characteristically convex *if every characteristic passing through Ω intersects $\partial\Omega$ at most twice.*

Definition 3 (Characteristic Forms). *A function ψ is said to be a* characteristic form *or* c–form *on Ω if on every characteristically convex subset of Ω, ψ may be represented in the form (3.21) where f and g are arbitrary functions of a single variable.*

As differing constants of integration can only be introduced on regions that are not characteristically convex, it is clear that any solution of Equation (3.20) on a region Ω may be represented as a c–form on Ω.

Yet it is still not possible to equate c–forms with the general solution of (3.1), since there is no requirement that a c–form be differentiable. In deriving Equation (3.20) from Equation (3.1) the existence of the second order derivatives of ψ is implicitly assumed, yet Equation (3.20) admits solutions that are not twice differentiable. For (3.21) to be a solution of (3.20) it is only necessary that one of f and g (depending on the order of differentiation) be continuously differentiable, while to be a solution of (3.1) both f and g must be continuously twice differentiable functions. Thus not all solutions of (3.20) are solutions of (3.1) in the classical sense.

Nevertheless such solutions may often be regarded as useful idealizations, arising from the assumption of inviscid motion. To accommodate such idealizations the following definitions are made:

Definition 4 (Singular c–forms.). *A c–form ψ is said to be* singular *at a point p contained in a region Ω if there exists a characteristically convex subset Ω' of Ω containing p such that when ψ is represented in form (3.21) on Ω', either of the component functions f or g possesses an non-integrable singularity at p. A c–form ψ is said to be* singular *in a region Ω if Ω contains a point p at which ψ is singular.*

Definition 5 (Weak and Strong Solutions.). *A function ψ defined on an open region Ω is said to be a* weak solution *of Equation (3.1) on Ω if it may be represented as a non-singular c–form on Ω. If in addition, when ψ is represented as a c–form, both its characteristic functions f and g are continuously twice differentiable functions on Ω then ψ is said to be a* genuine *or* strong solution *of Equation (3.1) on Ω.*

Thus the non-differentiable function proposed in the previous section as the solution of the internal tide problem for the step is a weak solution of Equation (3.1).

As discussed by Lax[29], the above definition is equivalent to requiring that a weak solution need only satisfy (3.1) in the sense of distribution theory (Jones[25]), whereas a strong solution will satisfy (3.1) in the classical sense. Singular c–forms must be excluded since they cannot be represented as distributions nor are they differentiable at the singularity.

It is important to note that not all weak solutions are physically realizable. Weak solutions must be interpreted in light of the assumption of inviscid motion; only strong solutions are unconditionally valid solutions of (3.1). In the following chapter an example will be given of a weak solution that is nowhere differentiable, such a solution can have no physical meaning and must be discarded. The primary purpose of introducing the notion of weak solutions is to defer the decision of whether a solution is physically reasonable to the last possible moment, rather than discard potentially useful solutions from the outset.

In later sections it will be necessary to distinguish those c–forms ψ which can be expressed in the form (3.21) on the whole of Ω. In anticipation, define

Definition 6 (Uniformity). *A c–form ψ is said to be* uniform *on Ω if on Ω, ψ may be represented in the form (3.21) where f and g are arbitrary functions of a single variable.*

Trivially, any c–form is uniform on a characteristically convex domain. The solution for the step problem derived in the previous section provides an example of a c–form that is not uniform.

3.4 Numerical Techniques - Shelf Regions

In this section two methods for solving the inviscid internal tide problem on a shelf region are described: those of Craig and Sandstrom. These methods are based on the theory of characteristics, and there is a sense in which they can be viewed as natural generalizations of the boundary collocation method used in Section 3.2.

The method proposed by Craig follows almost immediately from the theory of the previous section, and is presented first. Sandstrom's is considerably more complex and is only discussed briefly. In the next section it will be shown that this method is equivalent to a mapping technique similar to the conformal mapping techniques commonly applied to the solution of Laplace's equation. Variations on both these techniques will play an important part in the analysis of the next chapter.

3.4.1 Craig's Method

Neglecting for the moment the differentiability conditions a c–form must satisfy in order to be regarded as a solution of Equation (3.1), solving the internal tide problem on a region Ω becomes the problem of determining a c–form on Ω that satisfies the required boundary conditions on $\partial\Omega$. Craig has developed a simple numerical technique for solving this problem in the case when the bottom topography is essentially monotonic and the region possesses at least one radiating boundary.

To expedite the discussion of Craig's method, it is necessary to introduce two simple definitions.

Definition 7 (Characteristic Path, Circuit). *A sequence of segments of characteristics contained in $\Omega \cup \partial\Omega$ such that the intersection of each successive pair of segments lies on $\partial\Omega$ is a* characteristic path *on Ω. The notation $ABCD\ldots Z$ denotes the characteristic path with vertices A, B, C, D..., Z. A path of the form $ABCD\ldots ZA$ is a* characteristic circuit.

Consider the characteristic paths depicted in Figure 3.4. In Figure 3.4(a) the slope of the boundary is everywhere less than $\|c\|$ and the characteristic path "traverses" the region of variable topography. But in Figure 3.4(b) the slope of the boundary exceeds $|c\|$ at B and the characteristic path is "reflected" at this point. These two cases must be distinguished.

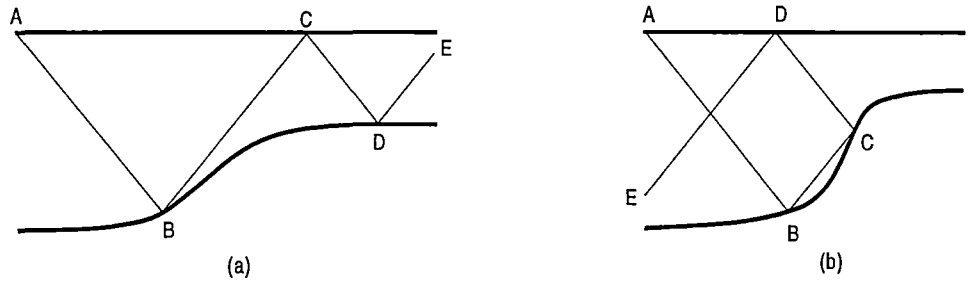

Figure 3.4: Characteristic Paths.

Definition 8 (Subcritical and Supercritical Slopes.). *Let the slope of the boundary at a point P be s. If $s < \|c\|$ then the boundary is said to be* subcritical *at P, if $s > \|c\|$ then the boundary is said to be* supercritical *at P, and if $s = \|c\|$ then the boundary is said to be* critical *at P.*

To illustrate Craig's method consider once more the topography depicted in Figure 3.4(a). As in Section 3.2 let the boundary conditions on ψ at the lower and upper boundaries be given by (3.4) and (3.5), where $B(x,z)$ is the barotropic forcing function derived in Craig[14]

$$B(x,z) = -i\omega\zeta_0(x-L)(1-z/h(x)). \tag{3.27}$$

At the left and right lateral boundaries a radiation condition is imposed. As in the case of the stepped topography ψ may be represented in the region of constant depth on the left as

$$\psi(x,z) = -i\omega\zeta_0(x-L)(1-z/h_1) + \sum_{n=1}^{\infty} a_n e^{-icn\pi x/h_1}\sin(n\pi z/h_1). \tag{3.28}$$

Rewriting this in the form (3.21) yields

$$\psi(\xi,\eta) = f(\xi) + g(\eta)$$

where

$$f(\xi) = \frac{-i\omega\zeta_0}{4h_1}[2(h_1 - cL)\xi + c\xi^2 - 2h_1L] + \frac{1}{2i}\sum_{n=0}^{\infty} a_n e^{-icn\pi\xi/h_1}, \tag{3.29}$$

$$g(\eta) = \frac{-i\omega\zeta_0}{4h_1}[2(h_1 + cL)\eta - c\eta^2 - 2h_1L] - \frac{1}{2i}\sum_{n=0}^{\infty} a_n e^{-icn\pi\eta/h_1}. \tag{3.30}$$

As discussed by Craig the introduction of the constant $n = 0$ term is essential for the convergence of the method. By a similar argument, on the region of constant depth on the right,

$$\psi(\xi, \eta) = f(\xi) + g(\eta)$$

where

$$f(\xi) = \frac{-i\omega\zeta_0}{4h_2}[2(h_2 - cL)\xi + c\xi^2 - 2h_2L] + \frac{1}{2i}\sum_{n=0}^{\infty} b_n e^{icn\pi\xi/h_2}, \tag{3.31}$$

$$g(\eta) = \frac{-i\omega\zeta_0}{4h_2}[2(h_2 + cL)\eta - c\eta^2 - 2h_2L] - \frac{1}{2i}\sum_{n=0}^{\infty} b_n e^{icn\pi\eta/h_2}. \tag{3.32}$$

As in the previous section, denote the value of ψ at a point R by $\psi(R)$ and the value of a function f on a characteristic PQ by $f(PQ)$. Applying (3.21) to the characteristic path $ABCDE$ depicted in Figure 3.4(a) generates the following linear equations

$$g(AB) + f(BC) = \psi(B) \tag{3.33}$$

$$f(BC) + g(CD) = \psi(C) \tag{3.34}$$

$$g(CD) + f(DE) = \psi(D), \tag{3.35}$$

which may be solved to yield

$$g(AB) + f(DE) = \psi(B) - \psi(C) + \psi(D). \tag{3.36}$$

Since the C^--characteristic AB passes through the region of constant depth on the left, $g(AB)$ may be expressed in terms of the a_n using (3.30). Similarly, since

the C^+–characteristic DE passes through the region of constant depth on the right, $f(DE)$ can be expressed in terms of the b_n using (3.31).

In this manner an equation relating the a_n, the b_n and the values of ψ at the boundary points B, C and D may be generated . The procedure is essentially the same for a characteristic path that does not traverse the region but is reflected by a supercritical boundary, the difference being that the equation generated will involve only the a_n or the b_n depending upon which region of constant depth contains the path's endpoints. In principle a countably infinite number of such paths could be considered, generating an infinite system of linear equations for the a_n and b_n.

Craig's method consists of generating a finite number of these paths and approximating the infinite trigonometric series in (3.29) – (3.32) by their truncated forms so that the resulting linear system is invertible. This may be regarded as a natural extension of the boundary collocation technique used in Section 3.2, where the simple mode matching collocation Conditions (3.10) – (3.12) have been replaced by the more generic technique described above. Indeed, it can be shown that Condition (3.10) is equivalent to Craig's method applied to a characteristic path that has been reflected by the supercritical component of the stepped topography while Conditions (3.11) and (3.12) correspond to the condition determined from a characteristic path that traverses the step.

The major difficulty associated with Craig's method is the optimal choice of the characteristic paths used in generating the system of linear equations. This problem is equivalent to the problem of optimally choosing collocation points in the boundary collocation technique.

As stated, Craig's procedure is not directly applicable in the presence of characteristic circuits or in the absence of a radiating boundary, and hence is unsuited to the problem of closed basins. Nevertheless, in the next chapter a variation on this method will prove to be a useful tool for establishing the existence of certain types of solutions on closed basins.

3.4.2 Sandstrom's Method

Like Craig's method, the method proposed by Sandstrom[41] may also be regarded as a natural extension to the simple boundary collocation technique applied in Section 3.2. Due to the length and depth of Sandstrom's original paper, only a brief review of Sandstrom's major results are given.

Sandstrom begins by considering the internal tide problem for a topography that is everywhere subcritical, demonstrating that for such a topography it is possible to generate a set of eigenfunctions of Equation (3.1) satisfying homogeneous boundary conditions for that topography.

Sandstrom begins by considering Equation (3.1) for a topography that is everywhere subcritical, and demonstrates how a set of eigenfunctions of the problem satisfying a homogeneous boundary condition can be generated.

Let Ω denote the region bounded above by $z = 0$ and bounded below by a subcritical topography $z = h(x)$. Consider any characteristic path defined on Ω and label consecutive intersections of this path with the surface as x_i, x_{i+1}, ...; Sandstrom defines the mapping T which takes x_n to x_{n+1},

$$Tx_n = x_{n+1}, \tag{3.37}$$

and defines a *T-periodic function* as any function f for which

$$f(Tx) = f(x) \tag{3.38}$$

Introducing the *phase function* $S(x)$ defined by

$$S(Tx) = S(x) + 1, \tag{3.39}$$

Sandstrom shows that the functions

$$e_k(x) = e^{2ki\pi S(x)} \qquad k = 0, 1, 2 \ldots \tag{3.40}$$

are T-periodic and orthogonal under the inner product

$$\langle f, g \rangle = \int_a^b f(\tau) g^*(\tau) S'(\tau) d\tau \tag{3.41}$$

where p^* represents the complex conjugate of the complex value p and $b = T^n a$ for any integer n, where powers of T have the obvious meaning.

Since the topography is assumed everywhere subcritical, Ω must be characteristically convex and an arbitrary solution ψ of Equation (3.1) may be written in the form

$$\psi(x,z) = f(x - z/c) + g(x + z/c). \tag{3.42}$$

Sandstrom demonstrates that the functions

$$\psi_k(x,z) = e_k(x - z/c) - e_k(x + z/c) \tag{3.43}$$

are solutions of (3.1) satisfying the homogeneous boundary condition $\psi = 0$ on $z = h(x)$ and $z = 0$. These functions may be regarded as the natural eigenfunctions for this topography in the same sense in which the travelling wave solutions

$$\exp(-in\pi(cx - z)/h) - \exp(-in\pi(cx + z)/h) \tag{3.44}$$

may be regarded as the natural eigenfunctions for a channel of constant depth h.

In a similar manner Sandstrom shows that

$$\psi(x,z) = \zeta_0(1 + S(x + z/c) - S(x - z/c)) + \sum_{k=-\infty}^{k=\infty} a_k \psi_k(x,z) \tag{3.45}$$

is a solution of (3.1) satisfying the boundary conditions $\psi = \zeta_0$ on $z = 0$ and $\psi = 0$ on $z = h(x)$. To solve the inviscid internal tide problem the coefficients a_k must be chosen so that ψ satisfies a radiation condition at the open boundaries.

To extend this technique to more general domains, Sandstrom treats an arbitrary topography as a set of subcritical topographies separated by supercritical topographies. This leads to a matching procedure similar to that employed in Section 3.2. Once more the major difficulty is in obtaining the coefficients of the eigenfunction expansion; Sandstrom uses a matrix method based on the orthogonality properties of the sequence $\{e_k(x)\}$, but equally well some form of boundary collocation could be applied. As it is necessary to apply this matching procedure

at every point where the topography changes from subcritical to supercritical or vice versa, Sandstrom's technique becomes awkward for regions which frequently vary between subcritical and supercritical.

The crucial component of Sandstrom's method is the derivation of the phase function $S(x)$. In his original paper Sandstrom provides phase functions appropriate to particular examples, referring to the work of Manton and Mysak[33] for a general method of obtaining a phase function for an arbitrary subcritical topography.

Representing the lower boundary as $z = h(x)$ Equation (3.39) can be reformulated as

$$S(x - h(x)/c) - S(x + h(x)/c) = 1. \tag{3.46}$$

Manton and Mysak solve this functional equation by replacing $1/c$ with λ and expanding in a Taylor series in λ about the point $\lambda = 0$. After some algebraic manipulation, this results in a power series solution for $S(x)$.

In principle Sandstrom's method is applicable to closed basins. Indeed, Sandstrom gives an example of a solution for a closed basin in his original paper, commenting that the physical interpretation of such solution is unclear. However, as will be shown in the next chapter, the procedure devised by Manton and Mysak for obtaining $S(x)$ will not converge for closed basins, and an alternative approach must be devised.

3.5 Complex Variable Theory

Upon setting $c = i$ the wave Equation (3.1) reduces to Laplace's equation in two dimensions. In this section it is demonstrated that the connection between these two equations is not just superficial, and that it is possible to construct a theoretical framework for Equation (3.1) which parallels the complex variable techniques (Carrier[8]) commonly applied to the solution of Laplace's equation.

Several authors, for example Hurley[23] and Larsen[28], have already presented solution techniques based on the standard methods of classical complex variable theory. The approach taken here is in an entirely different vein.

The section begins by demonstrating that it is possible to uniquely extend a solution of Equation (3.1) defined on a characteristically convex region in a manner analogous to the analytic continuation of a solution of Laplace's equation. It is then shown that this procedure forms the basis of a simple solution procedure similar to that described by Colton [12, 11] for elliptic systems, based on the Runge approximation theory. The section concludes by developing a mapping procedure under which the form of Equation (3.1) is invariant. This procedure strongly parallels the classical theory of conformal mapping for Laplace's equation.

3.5.1 Analytic Continuation

In this section a process for extending the definition of an arbitrary c–form defined on a region Ω to a larger region $\tilde{\Omega}$ containing Ω is described. The correspondence with the standard process of analytic continuation is clear. Although of only minor interest in itself, as shown in the next section this procedure forms the basis of an elegant solution technique for the inviscid internal tide problem on characteristically convex regions.

Consider an arbitrary c–form ψ defined on some characteristically convex open region Ω with boundary $\partial\Omega$ and let AB, BC, CD and DA denote the four characteristics tangent to $\partial\Omega$ that bound Ω, as depicted in Figure 3.5. Since Ω is characteristically convex, ψ may be represented in Ω in the form (3.21) where f is defined in the interval delimited by the C^+–characteristics AD and BC, and g is defined in the interval delimited by the C^-–characteristics AB and CD. Clearly then, (3.21) may be used to uniquely extend the definition of ψ to the open rectangle $ABCD$. In a similar fashion, the definition of an arbitrary c–form

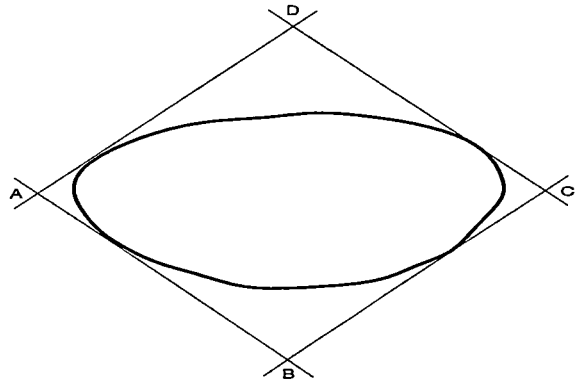

Figure 3.5: Unique C–Analytic Continuation.

ψ defined on the closure $\Omega \cup \partial\Omega$ of Ω may be uniquely extended to the closed rectangle $ABCD$.

Definition 9 (Unique C–Analytic Continuation.). *The extension of an arbitrary c–form ψ defined on some characteristically convex region Ω defined by the above process will be called the* unique c–analytic continuation *of ψ, and the domain of definition of this continuation will be called the* unique continuation domain.

The use of the terminology "unique c–analytic continuation" is to stress the similarities between this process and the classical process of analytic continuation, and is not intended to imply that the the resulting c–form is analytic.

Because it extends the definition of ψ to a region that is (in terms of the characteristic co–ordinates) rectangular, for the purposes of the next section this definition will prove somewhat inconvenient. Suppose instead that Ω is a characteristically convex region which takes the line $z = 0$ as one of its boundaries, as shown in Figure 3.6, and extend the definition of ψ along the line $z = 0$ in some arbitrary fashion. Once more the definition of ψ may be extended to $ABCD$. But because ψ is defined on the line $z = 0$, an extension of ψ to the rectangle $A'BC'D'$ can also be determined.

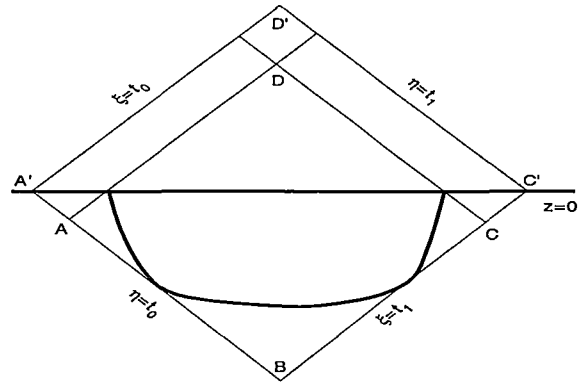

Figure 3.6: C–Analytic Continuation.

Representing ψ in the form (3.21), the values of f on the interval bounded by AD and $A'D'$ may be deduced from the values of g on Ω and the values taken by ψ on the line $z = 0$. Similarly, the values of g on the interval bounded by CD and $C'D'$ may be deduced from the values of f on Ω and the values taken by ψ along the line $z = 0$. In terms of the characteristic co–ordinates, the new region $A'BC'D'$ will be a square (since $z = 0$, the diagonal of $A'BC'D'$, represents the line $\eta = \xi$ in the characteristic co–ordinate frame), and can be represented in the form

$$\{(\xi, \eta) \mid t_0 < \xi < t_1,\ t_0 < \eta < t_1\} \tag{3.47}$$

for some t_0, t_1. This continuation to a square region will prove to be more useful than the continuation to a rectangular region defined by unique c–analytic continuation.

Definition 10 (C–Analytic Continuation.). *The extension of an arbitrary c–form ψ defined on some characteristically convex region Ω defined by the above process will be called the* c–analytic continuation *of ψ and the union $A'C' \cup \partial\Omega$ will be called the* augmented boundary. *The domain of definition of this continuation will be called the* continuation domain.

The c–analytic continuation of a c–form ψ is dependent upon the method

used to extend the definition of ψ on the line $z = 0$, and hence is only unique for a given extension of ψ.

These definitions lead to a very simple solution method for inviscid internal tide problem on characteristically convex regions similar to a technique applied to the solution of elliptic problems on simply connected regions.

3.5.2 The Runge Approximation Property

For elliptic problems on simply connected regions there exists an elegant solution technique based on the Runge approximation property. In this section it is shown that a similar technique may be applied to Equation (3.1) on any characteristically convex region.

As described in some detail by Colton[12, 11],

Definition 11 (Runge Approximation Property). *If $L[u] = 0$ represents a linear two dimensional elliptic problem, solutions of $L[u] = 0$ are said to have the* Runge approximation property *if, whenever D_1 and D_2 are two bounded simply connected domains and D_1 is a subset of D_2, any solution in D_1 can be approximated uniformly on compact subsets of D_1 by a sequence of solutions which can be extended as solutions to D_2.*

If a complete set of solutions are known on D_2 and these solutions possess the Runge Approximation property, then they also form a complete set of solutions on the bounded simply connected subset D_1.

Colton gives the following brief example. Let D be a bounded simply connected domain in R^2 with analytic boundary ∂D, and consider approximating the solution of Laplace's equation

$$u_{xx} + u_{yy} = 0 \tag{3.48}$$

on D subject to the boundary condition

$$u(x, y) = f(x, y) \tag{3.49}$$

on ∂D. The real and imaginary components of the positive integer powers of $z = x + iy$ are known to possess the Runge approximation property for Laplace's equation in any bounded simply connected domain, and so, using $\Re\{s\}$ and $\Im\{s\}$ to denote the real and imaginary components of the complex value s, the functions

$$u_{2n} = \Re\{z^n\} \tag{3.50}$$

$$u_{2n+1} = \Im\{z^n\} \tag{3.51}$$

form a complete family of solutions of (3.48) on D. Defining the inner product

$$\langle f, g \rangle_{\partial D} = \int_{\partial D} fg, \tag{3.52}$$

if the u_n are orthonormalized over ∂D to form the complete set $\{\varphi_n\}$, so that

$$\langle \varphi_n, \varphi_n \rangle_{\partial D} = 1 \tag{3.53}$$

$$\langle \varphi_m, \varphi_n \rangle_{\partial D} = 0, \tag{3.54}$$

then the solution $u(x, y)$ of (3.48) on D subject to (3.49) on ∂D may be written

$$u(x, y) = \sum_{n=0}^{\infty} \langle f, \varphi_n \rangle_{\partial D} \varphi_n(x, y). \tag{3.55}$$

In practice this sum is only carried to a finite number of terms with error estimates being determined from the maximum principle.

There are two major prerequisites for a solution procedure of this kind. First, it must be demonstrable that the solution of the problem on a domain D may be expressed as a linear combination of solutions defined on some larger region containing D. Secondly, there must exist a means by which the coefficients in this linear combination may be determined.

A procedure of this nature may be formulated for Equation (3.1), based on c–analytic continuation. Let Ω be an arbitrary characteristically convex region which takes as part of its boundary the line $z = 0$, and consider an arbitrary c–form defined on Ω

$$\psi(\xi, \eta) = f(\xi) + g(\eta).$$

Then ψ will possess a c–analytic continuation $\tilde{\psi}$

$$\tilde{\psi}(\xi,\eta) = \tilde{f}(\xi) + \tilde{g}(\eta).$$

defined on the continuation region

$$\tilde{\Omega} \equiv \{(\xi,\eta) \mid t_0 < \xi < t_1,\ t_0 < \eta < t_1\} \tag{3.56}$$

for some appropriate t_0, t_1.

If $\tilde{f}$ and $\tilde{g}$ are elements of some function space $V[t_0,t_1]$ and $\{\phi_n\}$ are $\{\theta_n\}$ are two sets of functions both complete in $V[t_0,t_1]$, then $\tilde{\psi}$ may be represented as

$$\tilde{\psi}(\xi,\eta) = \sum_{n=0}^{\infty} a_n\phi_n(\xi) + b_n\theta_n(\eta),$$

or equivalently

$$\tilde{\psi}(x,z) = \sum_{n=0}^{\infty} a_n\phi_n(x - z/c) + b_n\theta_n(x + z/c), \tag{3.57}$$

for some sets of coefficients $\{a_n\}$ and $\{b_n\}$. Since ψ is just the restriction of $\tilde{\psi}$ to Ω, it must be the case that

$$\psi(x,z) = \sum_{n=0}^{\infty} a_n\phi_n(x - z/c) + b_n\theta_n(x + z/c). \tag{3.58}$$

Note that $\tilde{f}(\xi)$ and $\tilde{g}(\eta)$ are defined on the same domain, and hence it is permissible to choose $\phi_n \equiv \theta_n$. This leads to an important case where the above analysis may be simplified even further. If ψ is identically zero on $z = 0$, then it is possible to construct a $\tilde{\psi}$ that is identically zero on $z = 0$. Choosing $\phi_n \equiv \theta_n$ implies that $b_n = -a_n$ and hence

$$\psi(x,z) = \sum_{n=0}^{\infty} a_n[\phi_n(x - z/c) - \phi_n(x + z/c)]. \tag{3.59}$$

This will prove to be of considerable importance in Chapter 6.

Thus it has been demonstrated that the solution ψ of the inviscid internal tide problem defined on any characteristically convex region Ω may be represented as a linear combination of solutions defined on the continuation region $\tilde{\Omega}$ of Ω.

The connection with the Runge approximation property is evident. In fact it may be demonstrated by a similar argument that a complete family of solutions $\{\varphi_n\}$ of equation (3.1) defined on a characteristically convex region Ω may be used to uniformly approximate a solution ψ of Equation (3.1) defined on any characteristically convex sub–region $\Omega' \subset \Omega$.

The solution procedure becomes complete with the specification of a method of determining the coefficients of this linear combination from the boundary conditions imposed on ψ. This method is of course to some extent dependent upon the form of the boundary conditions, although boundary collocation techniques and the orthogonalization method described by Colton are likely candidates. Further discussion of this topic is postponed until Chapter 6.

3.5.3 Conformal Mapping

This section develops a mapping procedure which leaves the form of Equation (3.1) invariant. The similarities between this procedure and conformal mapping are striking, and hence this procedure is termed *c–conformal mapping.* For classical conformal mapping, the existence of a conformal map from one region to another is guaranteed by the Riemann mapping theorem; later in the section it is demonstrated that the equivalent proposition for c–conformal maps is false, and an important property of maps which preserve the sub/supercritical nature of the boundary is noted. The section concludes by noting that Sandstrom's technique for subcritical topographies is equivalent to an implicit form of c–conformal mapping.

Definition 12 (C–Conformal Map.). *A mapping*

$$r = r(x, z), \qquad s = s(x, z), \tag{3.60}$$

from a region Ω *in the* xz *plane to a region* Ω' *in the* rs *plane is said to be* c–conformal *if* $r(x,z)$ *and* $s(x,z)$ *satisfy*

$$r_x = s_z, \tag{3.61}$$

$$c^2 r_z = s_x \tag{3.62}$$

in Ω. *Equations (3.61) and (3.62) will be called the* c–Cauchy Riemann Equations.

Note that setting $c = i$ reduces these definitions to their classical counterparts. Differentiating Equations (3.61) and (3.62) it is found that these equations imply that both $r(x,z)$ and $s(x,z)$ must satisfy Equation (3.1) on Ω. In turn, this implies that on every characteristically convex subset of Ω, $r(x,z)$ and $s(x,z)$ take the form

$$r(x,z) = g(x + z/c) + f(x - z/c), \tag{3.63}$$

$$s(x,z) = c(g(x + z/c) - f(x - z/c)). \tag{3.64}$$

The same issues of differentiability relating to c–forms and solutions of Equation (3.1) are applicable to solutions of the c–Cauchy Riemann equations. For consistency, the definition of strong and weak solutions of Equation (3.1) will be extended to encompass the c–Cauchy Riemann equations in the obvious manner.

It is now possible to state the major theorem of this section.

Theorem 13 (Conformal Mapping.). *The form of Equation (3.1) remains invariant under a c–conformal transformation of co–ordinates.*

This result is known to Blumen and Sukeyuki[4], who perform a Lie group analysis of (3.1). However these authors fail to fully exploit this knowledge, as they only consider (3.1) in the context of initial value problems where a general transformation of this type is of less utility.

The proof of the theorem consists of a straightforward change of co–ordinates together with an application of the c–Cauchy Riemann equations. It is more

enlightening to examine the effect of a c–conformal transformation in terms of characteristic co–ordinates.

Defining the characteristic co–ordinates ξ' and η' in the rs plane as

$$\xi' = r - s/c, \qquad \eta' = r + s/c, \tag{3.65}$$

a transformation of the form (3.63) – (3.64) may be represented in terms of characteristic co–ordinates as

$$\xi' = 2f(\xi), \tag{3.66}$$

$$\eta' = 2g(\eta). \tag{3.67}$$

That is, a c–conformal transformation has the effect of mapping (straight) characteristics in the xz plane to (straight) characteristics in the rs plane. Consequently, characteristic paths will map to characteristic paths and c–forms will map to c–forms and hence a c–conformal mapping may be regarded as just a repositioning or reshuffling of the characteristics.

As a simple example consider the mapping obtained by setting $c = 1$ and

$$g(\tau) = f(\tau) = \operatorname{sgn}(\tau)\, \tau^{1/2} \tag{3.68}$$

in Equations (3.63) and (3.64), where $\operatorname{sgn}\tau$ denotes the sign of τ. This is the c–conformal mapping which maps a square centred at the origin to a circle, as depicted in Figure 3.7. In this figure the diagram on the upper left represents an xz co–ordinate grid that covers the square, while the diagram on the upper right represents the image of this grid under the mapping. Similarly, the bottom pair of diagrams represents a grid of characteristic co–ordinates and the image of this grid under the mapping. From this second pair of diagrams it is evident that characteristics in the xz plane map to characteristics in the rs plane. For an example of solving of the inviscid model by c–conformal transformation, consult Section 6.6.1, where the inverse of this mapping is used to obtain solutions for a semi-circle.

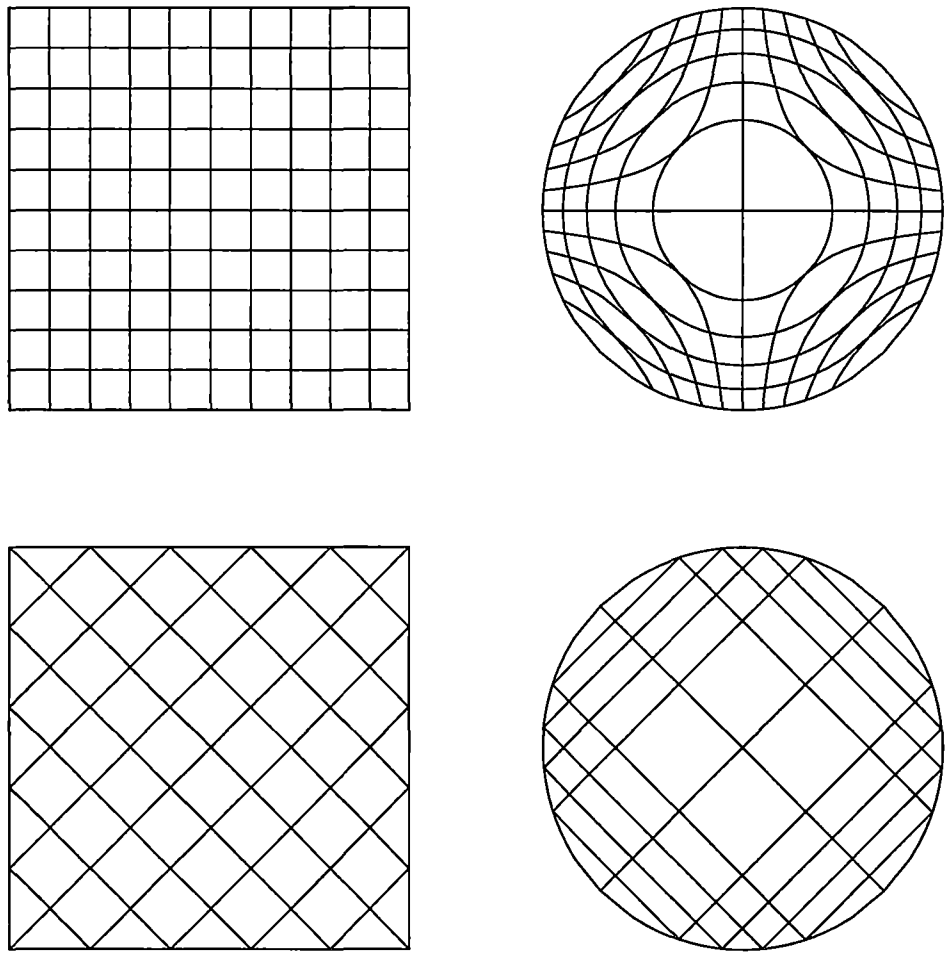

Figure 3.7: C–Conformally Mapping a Square to a Circle.

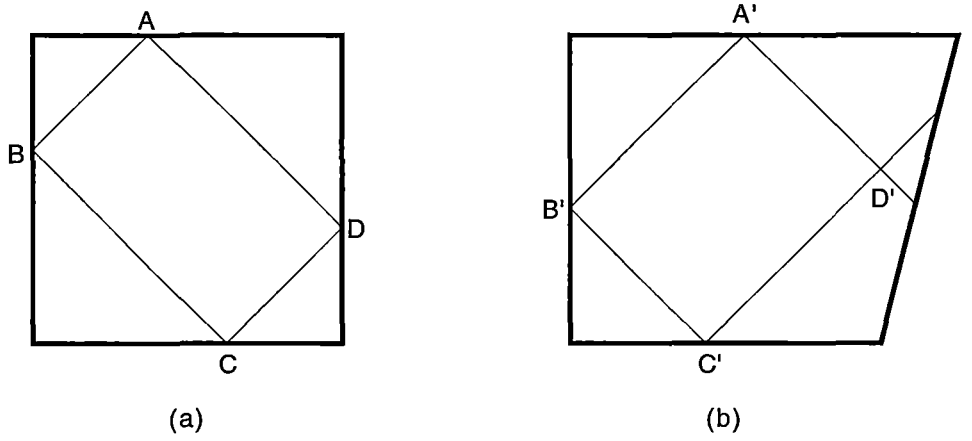

Figure 3.8: Counterexample to Riemann's Theorem for C–conformal Mapping.

For classical conformal mapping, the Riemann mapping theorem (Boas[5]) guarantees the existence of a conformal map from an arbitrary simply connected region with at least two boundary points to any other such region. A simple counter example demonstrates that the equivalent proposition for c–conformal maps does not hold.

Consider the problem of mapping the square region depicted in Figure 3.8(a) to the distended square shown in Figure 3.8(b). Suppose the point A maps to the point A'. Since a c–conformal map preserves characteristic paths and the image of B must lie on the boundary, B must map to B', and similarly C must map to C'. But this implies D maps to D', which does not lie on the boundary. The initial choice of A' is immaterial; it is not possible to map the points A, B, C and D to four points on the boundary of the distended square and preserve the characteristic path $ABCD$. Thus there can exist no c–conformal mapping between these two regions.

This form of argument may be extended to the problem of mapping an arbitrary region Ω to an arbitrary region Ω' . Given an characteristic path $ABCD\ldots Z$ defined on a region Ω, choosing the image A' of A in Ω' determines the images of the points B, C, D, ... Z in Ω'. This will in turn enforce

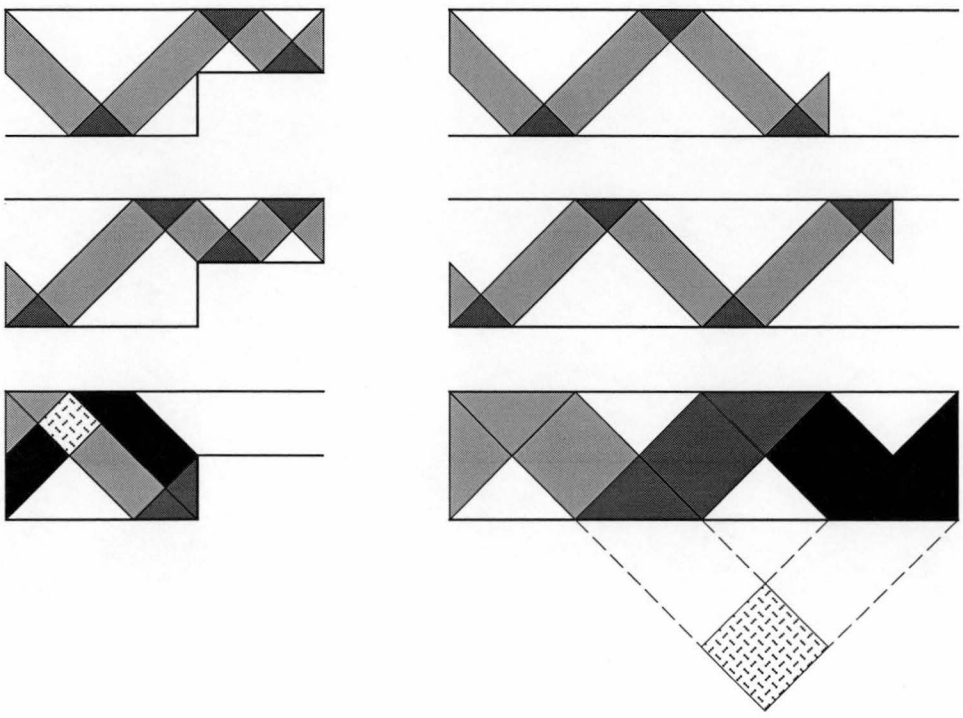

Figure 3.9: Mapping a Step to a Channel

restrictions on the form of the boundary $\partial\Omega'$, since the images of all these points must lie on $\partial\Omega'$.

This condition is extremely restrictive, and as a result there are few closed basins which can be c–conformally mapped to another region on which (3.1) is more conveniently solved. Fortunately the condition does not restrict c–conformal maps between shelf regions, since on a shelf region it is largely irrelevant how the lateral boundaries map — the radiation condition is easily enforced at a boundary of any shape. This topic is discussed further in Chapter 5, where a constructive procedure for generating c–conformal maps between shelf regions is devised.

One final difference between conformal and c–conformal mapping should be noted. It has already been seen that subcritical and supercritical topographies are fundamentally different in nature (Figure 3.4). Yet it is possible to c–conformally map a region bounded below by a topography that consists of both subcritical and

supercritical components to a region bounded by a purely subcritical topography.

Figure 3.9 depicts an example of such a mapping. Recall that characteristic paths must map to characteristic paths; the figure depicts how bands or families of characteristic paths must map in order to transform a step topography to a channel of uniform depth. Each of the diagrams on the left of the figure depicts a family of characteristic paths, shown in grey. The associated diagrams on the right show how these paths must be transformed by the c–conformal map. Differing grey levels are used to indicate more clearly the correspondence between the various components of the paths.

Note that the image of the hatched region in the third diagram on the left lies *outside* the channel. This would not be possible for a conformal map — Darboux's theorem (Carrier[8]) guarantees that under a conformal mapping, the interior of any simply connected region maps to the interior of a simply connected region.

It follows from an examination of Figure 3.4 that this particular property must be shared by any c–conformal transformation which maps a region Ω bounded below by both subcritical and supercritical components to a region Ω' bounded by a purely subcritical topography. For Ω will admit self–intersecting characteristic paths like that depicted in Figure 3.4(b), but Ω' cannot since its bounding topography is subcritical. As characteristic paths must map to characteristic paths, the image of the point of intersection cannot be contained in Ω'.

This same argument implies that the intersection point lies in the unique continuation region of Ω'. So if a c–form is known on Ω', its value can be established at the intersection point by unique c–analytic continuation.

For purely subcritical topographies, c–conformal mapping is closely connected with Sandstrom's technique. Consider mapping a region bounded above by $z = 0$ and below by a purely subcritical topography represented by $z = h(x)$ to a channel of uniform depth, so that $z = 0$ maps to $s = 0$ and $z = h(x)$ maps to

$s = 1/c$. Examining Equation (3.64), this implies that $f(\tau) \equiv g(\tau)$ and that

$$f(x - h(x)/c) - f(x + h(x)/c) = 1. \tag{3.69}$$

This is precisely the functional Equation (3.46) satisfied by the phase function of Sandstrom's method.

In this light the connection between Sandstrom's method and c–conformal mapping is evident. Sandstrom's method effectively performs an implicit c–conformal transformation from a purely subcritical topography to a channel of uniform depth. The natural eigenfunctions on this channel are the travelling wave solutions (3.44) and the eigenfunctions (3.43) proposed by Sandstrom are the inverse images of these solutions under the c–conformal map.

But c–conformal mapping has two advantages over Sandstrom's technique. First, c–conformal mapping separates the mapping procedure from the solution procedure, whereas in Sandstrom's method these procedures are inextricably connected. But more importantly, Sandstrom's technique requires that topographies consisting of both subcritical and supercritical components be split into several characteristically convex sub-regions, introducing a further matching procedure at the interfaces between these sub-regions. In contrast, c–conformal mapping allows such regions to be treated as a unit.

3.6 Non-Uniform Buoyancy Frequencies

Much of the theory developed in this chapter relies on the assumption that the buoyancy frequency N, and hence c, are constant. In this case (3.1) has the obvious first integral (3.21), and it is from this fact that much of the theory is derived. It is not entirely clear how these arguments may be extended to the more general case where N is a function of x and z. It is possible that the work of Vekua[46] on generalized analytic functions could be extended to encompass this case.

Nevertheless, all is not lost. Craig notes that introducing the change of coordinates

$$r(x,z) = x, \qquad s(x,z) = \int 1/c(z)\, dz \tag{3.70}$$

reduces

$$\psi_{xx} - c(z)^2 \psi_{zz} = 0 \tag{3.71}$$

to

$$\psi_{rr} - \psi_{ss} = D(s)\psi_s, \tag{3.72}$$

where

$$D(s) = \frac{1}{N}\frac{\partial N}{\partial s}. \tag{3.73}$$

This equation remains a good candidate for c–conformal mapping. Under a c–conformal map the left hand side of (3.72) will remain invariant, while the right hand side will consist of only first order terms. So although (3.72) is not invariant under the mapping, it is of the same essential form.

It is conjectured that an iterative scheme of the form

$$\psi^{(0)(x,z)} \equiv 0, \tag{3.74}$$

$$\psi_{rr}^{(i)} - \psi_{ss}^{(i)} = \psi_s^{(i-1)}, \tag{3.75}$$

could be used to solve (3.72), although this possibility has not been investigated in any detail. Furthermore, it is surmised that if it could be shown that such a scheme converges independently of Ω, a proof that the solutions of (3.72) possess the Runge approximation property on characteristically convex regions would soon follow.

3.7 Summary

The chapter commenced with a review of the theory of characteristics, and from this a convenient formalism for representing the general solution of the inviscid model was developed. This hinged on the introduction of the notion of a characteristically convex region.

Following this, two new techniques — c–analytic continuation and c–conformal mapping, were developed. These procedures unify the theory of characteristics, the techniques of Craig[14] and Sandstrom[41], and the classical theory of a single complex variable.

Much of the theory presented in the chapter relied heavily on the assumption of a constant buoyancy frequency. The chapter concluded with a brief discussion of the case of non-constant buoyancy frequencies.

The theory discussed in this chapter underpins much of the work of later chapters.

The next chapter investigates the behaviour of the inviscid model on a closed basin, and utilizes many of the tools developed here.

Chapter 5 examines the importance of correctly representing the boundary when solving the inviscid model by finite difference methods. It is shown that the implementation of finite difference methods can be simplified through c–conformal mapping, and a simple procedure for generating the required c–conformal maps is devised.

In this chapter it was outlined how c–analytic continuation in conjunction with the Runge approximation theory can form the basis of an elegant solution procedure for the inviscid model. This topic is pursued further in Chapter 6 where several extremely efficient solution methods for both the inviscid and viscous models of internal tide motion are developed.

Chapter 4

Internal Tide Motion in a Basin

The inviscid model discussed in the previous chapter has been applied to internal tide motion near the continental shelf by a number of authors, and in this context is reasonably well understood. More recently however, Cushman–Roisin *et al.*[17] have applied this same model to internal tide motion in a fjord, modelling the fjord as a closed basin. These authors encounter significant difficulties in obtaining numerical solutions to the inviscid problem, and find it necessary to consider a viscous model to ensure the convergence of the numerical process. They attribute these problems to the existence of resonant solutions, and conjecture that these resonant solutions arise as a consequence of the existence of characteristic circuits within the basin.

In this chapter the purely inviscid model is investigated for basin topographies, with particular reference to resonance phenomena. Although it is almost immediately seen that this problem is not well posed, the insight gained from the inviscid model is invaluable in the analysis of the corresponding viscous model.

The chapter begins with a brief review of the work of Cushman–Roisin *et al.*[17].

The chapter then proceeds by investigating the behaviour of the purely inviscid model for two classes of closed basin — rectangular basins and basins whose underlying topography is everywhere subcritical. Examining closed basins simplifies the analysis, since there is no radiation condition to be considered, yet the resulting conclusions are easily extended to more general regions. These two examples are found to represent the two extremes of behaviour allowed by the model.

For the rectangular basin it is immediately seen that the inviscid problem is not well posed, and the existence of resonant solutions is demonstrated. An important relationship between the problem's eigenfunctions and the geometry of the characteristic circuits is noted. It is shown that the inviscid model is not structurally stable, but that structurally stability is regained with the re–introduction of viscous terms.

The analysis of subcritical basins begins by re–examining an example discussed by Sandstrom[41] in the light of the theory presented in Chapter 3. Singularities at the corners of this basin are identified as point sources and sinks of internal tide motion. It is then demonstrated that unlike the rectangular basin, on a purely subcritical basin the inviscid model can always be solved without recourse to resonant solutions.

The conclusions derived from these two paradigms are then extended to arbitrary basins. It is shown that point sources and sinks are an essential component of internal tide motion near a subcritical corner, and a peculiar property of supercritical corners is noted. Finally the existence and uniqueness of solutions is discussed and it is shown that, as conjectured by Cushman–Roisin *et al.*[17], the presence of characteristic circuits strongly influences the behaviour of the model.

The chapter concludes by discussing several important ramifications of these observations for viscous models of internal tide motion.

4.1 The Method of Cushman–Roisin *et al.*

Cushman–Roisin *et al.*[17] apply the inviscid model (3.1) described in the previous chapter to internal tide motion in fjords. These authors model the fjord as a closed basin, assuming that all internal wave motion is reflected at the lateral boundaries open to the ocean. This work is later extended by Tverberg *et al.*[45] who re–introduce radiation conditions at the lateral boundaries.

Noting certain difficulties associated with applying existing characteristic based techniques to closed basins Cushman–Roisin *et al.*[17] advocate a more traditional finite difference approach. They propose a relaxation scheme derived from a related dissipative problem, but find that the purely inviscid implementation of this scheme does not converge and that viscous terms must be re–introduced to ensure the convergence of the numerical process.

Yet the problems encountered by Cushman–Roisin *et al.*[17] are to be expected. On a closed basin the inviscid model takes the form of a Dirichlet problem for the wave equation, and it has long been recognized that such problems may not be well posed (Tikhonov[44]). Physically, this corresponds to seeking periodic solutions from an externally forced non–damped closed system.

Cushman–Roisin *et al.*[17] conjecture that the existence of characteristic circuits results in resonant internal tide motion on the basin, and attribute the poor convergence of their numerical scheme to the presence of resonant solutions. In support of this conjecture Cushman–Roisin *et al.* provide arguments based on a finite difference representation of (3.1). These arguments are only partially convincing, for as discussed in the previous chapter, the model admits weak solutions of (3.1) which cannot be represented by finite differences in the xz co–ordinate frame.

Furthermore, to simplify the implementation of their finite difference schemes, both Cushman–Roisin *et al.*[17] and Tverberg *et al.*[45] approximate the basin topography by a polygonal path of horizontal and vertical segments constructed

so as to pass through the nodes of the chosen finite difference grid. Later in the chapter it shall be argued that this practice results in an unacceptable level of error.

4.2 Rectangular Basin

This first section of the chapter examines in detail the behaviour of the inviscid model (3.1) on a rectangular basin. The model is examined using both standard eigenfunction methods and a characteristic based technique, and a correspondence between the eigenfunctions and the characteristic circuits of the basin is revealed. This analysis indicates that the problem is not well posed, and in support of the conjecture of Cushman–Roisin *et al.*[17], it is demonstrated that for a rectangular basin the existence of characteristic paths leads to resonant internal tide motion. The section concludes with a brief examination of the corresponding viscous model.

4.2.1 Eigenfunction Analysis

In this section the inviscid model is solved on a rectangular basin by standard eigenfunction methods.

Consider solving Equation (3.1) on a rectangular basin Ω of depth h and width l whose upper left hand corner is located at the origin, subject to the boundary condition

$$\psi = 0 \tag{4.1}$$

on the lower three boundaries, while at the upper boundary, $z = 0$,

$$\psi(x, 0) = B(x) \tag{4.2}$$

for some arbitrary $B(x)$[1].

[1]Note that to preclude a volume flux into the basin, it must be the case that $B(0) = B(l) = 0$

Applying a standard separation of variables technique to (3.1) yields the general solution

$$\psi(x,z) = \sum_{n=0}^{\infty} a_n \sin\frac{n\pi x}{l} \sin\frac{n\pi(z+h)}{lc}, \tag{4.3}$$

where the a_n must be chosen so that the boundary condition (4.2) is satisfied. Assuming that $B(x)$ may be expanded in a Fourier sine series of the form

$$B(x) = \sum_{n=0}^{\infty} b_n \sin\frac{n\pi x}{l} \tag{4.4}$$

and equating coefficients of $\sin(n\pi x/l)$ yields the relation

$$a_n \sin n\pi h/(lc) = b_n \tag{4.5}$$

for the a_n.

There are three distinct cases to be considered.

First suppose the ratio $h/(lc)$ is irrational. Then for all choices of the natural number n,

$$\sin\frac{n\pi h}{lc} \neq 0 \tag{4.6}$$

and the a_n may uniquely determined from the b_n using relation (4.5). Thus the solution (4.3) will be unique and well defined provided the series (4.3) converges. When (4.4) consists of only a finite number of terms it is clear that (4.3) must converge, although convergence is not assured in the more general case.

The other two cases to be considered arise when $h/(lc)$ is rational. Let p and q be the smallest relatively prime integers for which $h/(lc) = p/q$. Setting $n = mq$, for all choices of the natural number m,

$$\sin\frac{n\pi h}{lc} = 0. \tag{4.7}$$

Thus if any of the corresponding b_n are non–zero, by (4.5) the solution (4.3) will be undefined and there will exist no solution of this form. If instead all of the

corresponding b_n are zero, then the associated a_n may be chosen arbitrarily. The solution given by (4.3) is once more well defined but is no longer unique.

As an example consider the case $h/(lc) = 1$. Then (4.7) is satisfied for all choices of the natural number n and thus irrespective of the choice of the a_n, if ψ is of the form (4.3) then

$$\psi(x, 0) \equiv 0. \tag{4.8}$$

Unless $B(x) \equiv 0$ there can be no solution of the form (4.3) which satisfies (4.2), but if $B(x) \equiv 0$ then (4.3) satisfies (4.2) for any choice of the a_n.

Condition (4.7) is equivalent to stating that the eigenfunction

$$\sin \frac{n\pi x}{l} \sin \frac{n\pi(z+h)}{lc} \tag{4.9}$$

is a solution of the corresponding homogeneous problem. Such solutions shall be called *natural modes*, since their presence in the solution is independent of the boundary forcing.

This analysis shows that the internal tide problem for a rectangular basin is not well posed. In many instances the model possesses no unique solution for a given set of boundary conditions, and in those instances where a unique solution does exist this solution is not structurally stable, that is, the solution does not depend continuously on the boundary data.

Before carrying the analysis of this problem any further, it shall be convenient to re–establish the results of this section from the perspective of the theory of characteristics.

4.2.2 Characteristics

The analysis of the previous section is now repeated using characteristic based methods, revealing a correspondence between the periodicities of the eigenfunctions and the geometries of closed circuits.

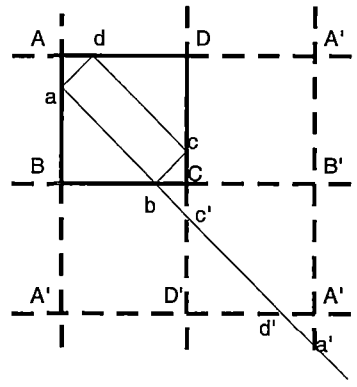

Figure 4.1: Tiling the plane with reflections of the basin.

To solve (3.1) for the rectangular basin via characteristics it will be necessary to trace the trajectory of an arbitrary characteristic path indefinitely. To this end, construct a tiling of the plane from reflections of the basin as depicted in Figure 4.1,

where A' represents a reflection of the point A and so on. Then to determine the trajectory of the characteristic path $abcd\ldots$ it is sufficient to examine the straight line $abc'd'\ldots$.

An arbitrary characteristic path $abcd\ldots$ will form a characteristic circuit if the line ab passes through a point a' that is a reflection of a. Examining Figure 4.1 shows that this will be the case if and only if there exist integers m and n such that

$$mh = ncl, \tag{4.10}$$

that is, if $h/(lc)$ is rational. Since the characteristic path $abcd\ldots$ was arbitrary, all characteristic paths must form circuits when this condition is satisfied. (Paths passing through the corner points may be regarded as limiting cases.)

As was the case with the separation of variables technique, it will be necessary to consider two distinct cases, depending upon whether $h/(lc)$ is rational or not.

The Rational Case

To illustrate the solution technique when $h/(lc)$ is rational, consider the case depicted in Figure 4.1, where $h/(lc) = 1$. In this instance all characteristic paths are characteristic circuits which form diamonds about the diagonals of the basin, as shown in Figure 4.1. Then as discussed in Chapter 3, since the basin is characteristically convex any solution ψ may be represented as a c–form

$$\psi(x,z) = f(x - z/c) + g(x + z/c). \tag{4.11}$$

Denoting the value of ψ at a point p by $\psi(p)$ and the value of a function f on a characteristic pq by $f(pq)$, applying relation (4.11) to Figure 4.1 yields

$$g(cd) + f(da) = \psi(d) \tag{4.12}$$

$$f(da) + g(ab) = 0 \tag{4.13}$$

$$g(ab) + f(bc) = 0 \tag{4.14}$$

$$f(bc) + g(cd) = 0 \tag{4.15}$$

where use has been made of the fact that $\psi = 0$ on the lower three boundaries of the basin. Solving this system yields $\psi(d) = 0$. As the choice of characteristic circuit was arbitrary, this implies ψ must be identically zero on the upper surface of the basin. In agreement with the separation of variables analysis, a solution will only exist when $B(x) \equiv 0$.

When $B(x)$ and hence ψ are identically zero on the surface, the system of equations (4.12) – (4.15) has the solution

$$f(da) = -g(ab) = f(bc) = -g(cd) = k, \tag{4.16}$$

for some arbitrary constant k. Then a solution ψ may be determined by specifying a value of k for each characteristic circuit in the basin. As the choice of these constants is arbitrary, this solution will be non–unique.

But not all such solutions will be physically acceptable. For example, because k may be chosen arbitrarily for each circuit, it is possible to generate a weak

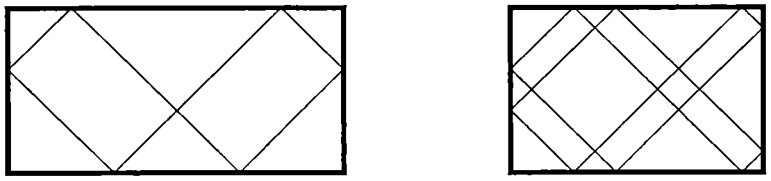

Figure 4.2: Characteristic Circuits for $h/(lc)$ Rational.

solution that is nowhere differentiable. Such a solution is clearly meaningless and must be discarded.

Also, as there exist an uncountably infinite number of characteristic circuits, to determine ψ on Ω from an analysis of characteristics it is necessary to fix an uncountably infinite number of constants. In contrast, the separation of variables analysis required only a countable number of constants be chosen to determine a solution.

This discrepancy arises because (4.3) is effectively a Fourier sine series representation of ψ. Thus the series (4.3) will converge to a solution ψ in the sense of the usual L^2 norm, where L^2 denotes the space of square integrable functions. Since k may be chosen arbitrarily for each circuit, it is possible to generate from the characteristics method multiple c–forms which correspond to a given single series solution, as any two functions which differ at only countably many points are indistinguishable under the L^2 norm. It will be assumed that any two such solutions are physically equivalent.

For the general case when $h/(lc)$ is rational, the solution method proceeds in an identical manner, differing only in the more complicated geometries of the characteristic circuits. Figure 4.2 depicts some typical characteristic circuits for the cases $h/(lc) = 1/2$ and $h/(lc) = 2/3$. In contrast with the example given above, in the general case each characteristic circuit may intersect the upper surface of the basin several times. Thus rather than each characteristic circuit giving rise to a simple restriction on ψ at one point on the upper surface, each characteristic circuit may give rise to a relation between values of ψ at several

points on the upper surface.

This is entirely in agreement with the results of the separation of variables analysis in which it was demonstrated that a solution only exists when $B(x)$ lacks certain harmonics in its sine series expansion. These are precisely the harmonics that violate the conditions imposed by the characteristic circuits. Thus, the geometries of the characteristic circuits reflect the periodicities of the problem's eigenfunction solutions.

The Irrational Case

Consider now the case when $h/(lc)$ is irrational.

Let the ratio $h/(lc)$ be irrational and consider a characteristic path passing through a point $p \in \Omega$. Examining Figure 4.1 it can be seen that this characteristic path will never form a characteristic circuit, for it cannot pass through a reflection p' of p as this would imply the existence of two integers m and n such that

$$mh = ncl. \tag{4.17}$$

In this case the characteristic paths are of infinite length, and "reflect" around inside the basin indefinitely.

Let $\ldots abcde \ldots$ denote one of these characteristic paths. As before, it is possible to generate a system of linear equations relating $f(\xi)$ and $g(\eta)$ on this characteristic path

$$\vdots$$

$$g(ab) + f(bc) = \psi(b) \tag{4.18}$$

$$f(bc) + g(cd) = \psi(c) \tag{4.19}$$

$$g(cd) + f(de) = \psi(d) \tag{4.20}$$

$$\vdots$$

Because the path never forms a circuit, this system of equations is infinite, but in principle can be solved sequentially. Setting $f(bc) = k$, $g(cd))$ may be determined from Equation (4.19) and in turn $f(de)$ may be determined from (4.20) and so on. Similarly, in the reverse direction, $g(ab))$ may be determined from Equation (4.18), and so on. In principle, continuing this process ad infinitum determines f and g for the entire path. Performing this procedure for each path in Ω determines f and g and hence ψ on Ω. This procedure is a straightforward extension of the method of Craig discussed in Section 3.4.1.

Thus when h/cl is irrational a c–form can be constructed that satisfies an arbitrary choice of Dirichlet boundary conditions. However, this c–form may not represent an acceptable solution of Equation (3.1), for it cannot be guaranteed that the f and g generated by this algorithm will not become unbounded and possess non–integrable singularities in Ω. In this event the resulting c–form is singular and must be discarded. Comparing with the eigenfunction analysis, this corresponds to the case when the series solution (4.3) fails to converge.

Again the solution obtained by characteristic methods is not unique as the choice of the constant k is arbitrary and must be chosen independently for each path. For the irrational basin the separation of variables yields a unique solution, this discrepancy is again explained by noting that (4.3) corresponds to the Fourier representation of ψ.

In summary then, it has once more been established that the internal tide problem for the rectangular basin is not well posed, and an important correspondence between the natural modes and the geometries of closed circuits has been noted.

4.2.3 Resonance

In the two previous sections it was seen that there exist instances for which the inviscid model does not possess solutions for all choices of Dirichlet boundary

data. By considering a time dependent form of (3.1) it will now be shown that those instances correspond to resonant internal tide motion. Some familiarity with the Fourier Sine transform is assumed. For additional reference the reader is directed to Özişik[35].

From Chapter 2 the time dependent form of Equation (3.1) is

$$\Psi_{xxtt} + \Psi_{zztt} + N^2\Psi_{xx} = 0, \tag{4.21}$$

where the time dependent stream function $\Psi(x,z,t)$ and the time independent stream function $\psi(x,z)$ are related by

$$\Psi(x,z,t) = e^{-\imath\omega t}\psi(x,z). \tag{4.22}$$

As before, consider a rectangular basin of depth h and width l the upper left hand corner of which is located at the origin. Define the two dimensional Fourier sine transform $f^*_{mn}(t)$ of a function $f(x,z,t)$ as

$$f^*_{mn}(t) = \int_{-h}^{0}\int_{0}^{l} f(x,z,t)\sin\frac{m\pi x}{l}\sin\frac{n\pi z}{h}dxdz, \tag{4.23}$$

where the subscripts m and n should not be confused with derivative notation. The corresponding inversion formula is

$$f(x,z,t) = \frac{4}{lh}\sum_{m=0}^{\infty}\sum_{n=0}^{\infty} f^*_{mn}(t)\sin\frac{m\pi x}{l}\sin\frac{n\pi z}{h}. \tag{4.24}$$

Multiplying Equation (4.21) by $\sin(m\pi x/l)\sin(n\pi z/h)$ and integrating by parts twice and applying the boundary conditions yields

$$\pi^2\left(\frac{m^2}{l^2}+\frac{n^2}{h^2}\right)\Psi^*_{mntt} + \frac{\pi^2m^2N^2}{l^2}\Psi^*_{mn} - \frac{2b_m\omega^2}{l}e^{-\imath\omega t} = 0, \tag{4.25}$$

where it has been assumed that the forcing function $B(x)$ may be expanded as a Fourier sine series of the form (4.4) and that the order of integration and differentiation may be interchanged without effect. Defining

$$\gamma_{mn} = \frac{2h^2l\omega^2}{\pi(m^2h^2+n^2l^2)} \tag{4.26}$$

and

$$\omega_{mn}^2 = \frac{m^2 N^2 h^2}{m^2 h^2 + n^2 l^2}, \tag{4.27}$$

this equation may be written as

$$\Psi^*_{mntt} + \omega_{mn}^2 \Psi^*_{mn} = b_m \gamma_{mn} e^{-i\omega t} \tag{4.28}$$

which has as its general solution

$$\Psi^*_{mn}(t) = c_{1mn} e^{-i\omega_{mn} t} + c_{2mn} e^{i\omega_{mn} t} + P_{mn}(t), \tag{4.29}$$

where the c_{kmn}'s must be determined from the initial conditions, and $P_{mn}(t)$ denotes the particular solution given by

$$P_{mn}(t) = \begin{cases} \frac{-ib_m \gamma_{mn}}{2\omega} t e^{-i\omega t} & \text{if } \omega_{mn} = \omega \\ \frac{b_m \gamma_{mn}}{\omega_{mn}^2 - \omega^2} e^{-i\omega t} & \text{if } \omega_{mn} \neq \omega. \end{cases} \tag{4.30}$$

The solution $\Psi(x, z, t)$ may be obtained from the transform solution $\Psi^*_{mn}(t)$ by means of the inversion formula (4.24).

Applying Equations (3.2) and (4.27), the condition

$$\omega_{mn} = \omega \tag{4.31}$$

may be reduced to

$$\frac{h}{cl} = \frac{n}{m}. \tag{4.32}$$

That is, Equation (4.31) is equivalent to the condition that h/cl be rational.

Thus when h/cl is rational, $\Psi(x, z, t)$ may contain components with a secular time dependence, $te^{-i\omega t}$. Such solutions are clearly at odds with the assumption of periodicity implicit in (4.22) and there can be no time independent solution $\psi(x, z)$ satisfying this relation. Correspondingly, there can exist no solution of Equation (3.1).

Note that this solution implies that the inviscid model is not structurally stable on a rectangular basin — a small perturbation in the dimensions of the basin may lead to a qualitative change in the behaviour of the solution.

The results of this section lend strong support to the conjecture of Cushman–Roisin *et al.*[17] that the existence of characteristic circuits leads to resonant internal tide motion, since for a rectangular basin the condition that h/cl be rational is equivalent to requiring that all characteristic paths be characteristic circuits. In support of their hypothesis, Cushman–Roisin *et al.*[17] have argued from the perspective of a finite difference scheme; the Fourier transform approach adopted here is more direct, but does not readily generalize to arbitrary topographies.

There is an obvious analogy to be drawn with undamped simple harmonic motion. When h/cl is rational, there exist certain natural modes of vibration which exist independently of any boundary forcing. These correspond to the eigenfunctions of the model which satisfy purely homogeneous boundary conditions. If these natural modes remain unforced by the boundary conditions, the problem possesses a periodic solution where the presence of natural modes is determined by the initial conditions imposed on the system. But if a natural mode is excited by the boundary forcing then a resonant solution that exhibits a secular $te^{-i\omega t}$ time dependence results.

4.2.4 A Viscous Model

In the preceding section it was seen that that the inviscid model is not structurally stable on the rectangular basin. In this section the viscous model is examined. To simplify the analysis a zero stress condition (Pond and Pickard[37]) is adopted at the boundary.

From Chapter 2, retaining viscous terms in the time dependent form of

Equation (3.1) yields

$$\Psi_{xxtt} + \Psi_{zztt} + N^2\Psi_{xx} = \nu(\Psi_{xxxxt} + 2\Psi_{xxzzt} + \Psi_{zzzzt}), \tag{4.33}$$

where once again the time dependent stream function $\Psi(x, z, t)$ and the time independent stream function $\psi(x, z)$ are related by

$$\Psi(x, z, t) = e^{-\imath\omega t}\psi(x, z). \tag{4.34}$$

To allow a simple sine transform to be applied, a zero stress condition will be assumed on all boundaries. That is, on the boundary, the normal derivative of the tangential component of velocity will be assumed zero (Pond and Pickard[37]). This is equivalent to assuming that the interaction of the fluid and the boundary is perfectly frictionless.

Again representing $B(x)$ in the form (4.4) and taking the Fourier sine transform of Equation (4.33) yields

$$\Psi^*_{mntt} + \lambda_{mn}\Psi^*_{mnt} + \omega^2_{mn}\Psi^*_{mn} = b_m\gamma_{mn}e^{-i\omega t}, \tag{4.35}$$

where

$$\lambda_{mn} = \nu\pi^2\frac{m^2h^2 + n^2l^2}{l^2h^2}, \tag{4.36}$$

$$\omega^2_{mn} = \frac{m^2h^2N^2}{m^2h^2 + n^2l^2}, \tag{4.37}$$

$$\gamma_{mn} = \frac{i\omega\nu ml(2m^2h^2\pi^2 - l^2) - \omega^2 mh^2l^2}{\pi(m^2h^2 + n^2l^2)}. \tag{4.38}$$

In this instance the solution for the transform function is

$$\Psi^*_{mn} = c_{1mn}e^{-i\mu_{1mn}t} + c_{2mn}e^{-i\mu_{2mn}t} + P_{mn}(t), \tag{4.39}$$

where c_{1mn} and c_{2mn} are arbitrary constants and μ_{1mn} and μ_{2mn} are the roots of the quadratic

$$\mu^2 - i\lambda_{mn}\mu + \omega^2_{mn} = 0. \tag{4.40}$$

The particular solution $P_{mn}(t)$ is given by

$$P_{mn}(t) = \frac{b_m \gamma_{mn}}{\omega^2 - i\omega\lambda_{mn} + \omega_{mn}^2} e^{-iwt}. \tag{4.41}$$

Note that the coefficient of $\exp(i\omega t)$ in $P_{mn}(t)$ is complex, and thus $P_{mn}(t)$ is out of phase with the boundary forcing function by a factor dependent upon ν.

Once again, the original function is calculated from its transform by means of the inversion formula (4.24).

Thus in the presence of viscosity it is always possible to obtain a solution which possesses a time dependence of the form $\exp(-i\omega t)$. In spite of the somewhat unrealistic boundary conditions assumed, it would appear that the viscous model regains the structural stability lost in the inviscid model.

The viscous solution displays resonant peaks in the frequency domain where the amplitude takes a local maximum, rather than the secular time dependence exhibited by the inviscid solution. These peaks are slightly displaced from the resonant frequencies of the undamped case and undergo a sharp π phase change relative to the forcing at the resonant frequency. This behaviour is typical of damped simple harmonic motion, and once again there is a strong analogy with simple harmonic motion.

4.3 Subcritical Basins

Consider now the class of basins whose bounding topography is everywhere subcritical. It will be seen that these basins possess a very different set of properties from those of rectangular basins. In particular, it will be demonstrated that on a subcritical basin Equation (3.1) possesses a solution for any choice of Dirichlet boundary data.

4.3.1 Sandstrom's Example

By way of introduction to subcritical basins consider the example provided by Sandstrom[41].

Let the open region Ω denote the basin bounded above by $z = 0$ and below by the subcritical topography $z = h(x)$, where

$$h(x) = -c(\alpha/2 - \sqrt{\alpha^2/4 - x(1-x)}) \qquad 0 \leq x \leq 1 \tag{4.42}$$

and $\alpha > 1$. (The value suggested for α in Sandstrom[41] is clearly a misprint as this would render $h(x)$ imaginary). Sandstrom notes that the eigenfunctions of (3.1) satisfying a homogeneous boundary condition $\psi = 0$ on $\partial\Omega$, that is the natural modes, are given by

$$\psi_k(x,z) = \exp(2ki\pi S(x - z/c)) - \exp(2ki\pi S(x + z/c)), \tag{4.43}$$

where

$$S(\tau) = \left(\ln \frac{t}{1-\tau}\right) \Big/ \left(\ln \frac{\alpha+1}{\alpha-1}\right). \tag{4.44}$$

In spite of the singularities at the corner points $(0,0)$ and $(1,0)$, both terms of (4.43) are bounded and hence integrable on the open region Ω. Thus the ψ_k constitute non–singular c–forms on Ω.

The existence of the natural modes implies that the general Dirichlet problem for Equation (3.1) on this region does not possess a unique solution. For if $\psi(x,z)$ is a solution satisfying a set of Dirichlet boundary conditions on $\partial\Omega$, then for any choice of the a_k, the solution

$$\psi'(x,z) = \psi(x,z) + \sum_{k=0}^{\infty} a_k \psi_k(x,z) \tag{4.45}$$

will also satisfy these same boundary conditions.

The ψ_k have a natural interpretation in terms of the theory of c–conformal

mapping introduced in the previous chapter. Defining

$$r(x,z) = S(x+z) + S(x-z) \tag{4.46}$$

$$s(x,z) = c(S(x+z) - S(x-z)) \tag{4.47}$$

it can be seen that the phase function (4.44) corresponds to a c–conformal map which maps the basin to a channel of uniform depth in the rs plane. On this channel each of the $\psi_k(x,z)$'s correspond to a travelling wave solution of the form

$$\exp(2ki\pi(r - s/c)) - \exp(2ki\pi(r + s/c)). \tag{4.48}$$

The singularities in the ψ_k arise because the corner points of the basin map to infinity in the channel.

Thus the ψ_k may be interpreted as the natural travelling wave solutions for the subcritical basin described by (4.42). The singularities at the corner points represent wave sources and sinks, similar to the sources and sinks present at infinity on the channel. In the channel, a wave propagating to the left or right does so indefinitely; the topography in the channel is incapable of reflecting the wave. The same is true for the subcritical basin, the subcritical topography is incapable of reflecting a propagating wave. Energy transmitted by the wave is propagated into the corner, and correspondingly, must have originated in the opposing corner.

Of course from a physical standpoint, these solutions are highly idealized and would not be realized in practice. For they imply that approaching either corner of the basin the fluid velocities become unbounded while the local wavelength tends to zero. This clearly violates the assumptions under which the linear inviscid model was derived and would not be observed in practice.

Nevertheless this example is typical of subcritical topographies. The subcritical wedge described by Wunsch[47] provides a similar example.

4.3.2 Arbitrary Subcritical Basins

Consider now the more general Dirichlet problem on an arbitrary subcritical region. An analysis of characteristics shows that Equation (3.1) will possess a solution on a subcritical basin for any choice of Dirichlet boundary data.

Let Ω denote an arbitrary subcritical region bounded above by $z = 0$ and below by the subcritical topography $z = h(x)$ and let P denote an arbitrary characteristic path passing through some point $p \in \Omega$. Since the topography is everywhere subcritical, this path may be extended indefinitely to both the left and the right of p, passing closer to the corner points of the region with each intersection with the boundary $\partial\Omega$.

Thus the subcritical basin corresponds precisely to the case of a rectangular basin with $h/(lc)$ irrational, and can be solved by an identical method. There are, however, two minor differences.

Firstly, the rectangular basin possesses a unique eigenfunction solution when $h/(lc)$ is irrational. Yet Sandstrom's example discussed in the previous section does not possess a unique eigenfunction solution. It is unclear precisely what determines whether a given problem has a unique eigenfunction solution.

Also, for the rectangular basin it is possible that the f and g determined by the method of Section 4.2.2 may exhibit non–integrable singularities in Ω, in which case the c–form determined by these functions does not represent a valid solution of (3.1). This is not possible on a subcritical basin.

The solution procedure described in Section 4.2.2 essentially traces out each characteristic path, determining a new value for f or g at each intersection with the boundary $\partial\Omega$. On the rectangle, each characteristic path wanders through Ω, and so it is possible for a non–integrable singularity to form anywhere in the basin. But on a subcritical basin, each intersection with the boundary brings the path closer to a corner point of the basin. If ψ is bounded on $\partial\Omega$, then a non–integrable singularity can only form in the limit, at a corner point of the

basin. Thus the subcritical basin can only possess a non–integrable singularity at a corner point.

On a subcritical basin the model displays a markedly different behaviour to that of the rectangular basin. On the rectangular basin the existence of natural modes implies the existence of boundary conditions for which the model (3.1) has no solution, corresponding to resonant solutions of the time dependent model (4.21). Here it has been shown that not only must every subcritical basin possess natural modes, but that a solution of the time independent model can be found for any choice of boundary forcing, although this solution is not unique.

4.4 More General Regions

The observations drawn from the examples of rectangular and subcritical basins are easily extended to more general regions. The section begins by investigating the behaviour of solutions at a corner point, and a fundamental distinction between subcritical and supercritical corners is noted. The questions of existence and uniqueness of solutions of the inviscid model on an arbitrary basin are then considered.

4.4.1 Behaviour at a Corner

The solutions of the inviscid model obtained for the rectangular basin and Sandstrom's solutions for the subcritical basin (4.42) exhibit quite disparate properties at their respective corner points. This section examines the behaviour of solutions at an arbitrary corner. It is seen that although Sandstrom's example is indicative of the general case for subcritical corners, the example furnished by the rectangular basin constitutes a special case amongst supercritical corners.

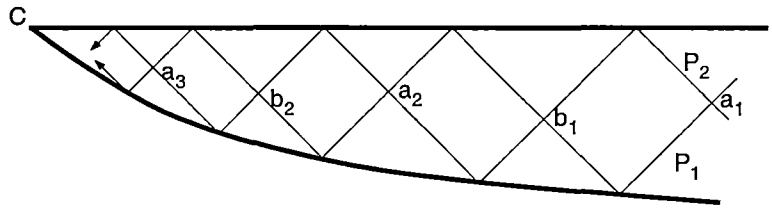

Figure 4.3: Subcritical Corner

Subcritical Corners

Sandstrom's solutions (4.43) for the homogeneous inviscid problem on the subcritical basin described by (4.42) exhibit singularities at the corners of the basin. In Section 4.3.1 it was argued that these singularities represent sources and sinks of internal tide motion. By that same argument it can be expected that all subcritical corners should give rise to such singularities. This fact can be demonstrated through an analysis of characteristics.

Let Ω denote a subcritical region with one open lateral boundary, like that depicted in Figure 4.3. This region might represent the corner of some larger closed basin, or perhaps a shelf region that has been continued onto the coast. Label the corner point C and consider any two distinct characteristic paths P_1 and P_2 in Ω. Since the region is subcritical these paths may be continued indefinitely towards the corner, converging to the corner point C. Define the sequence of points $\{a_n\}$ as the points for which a C^+–segment of P_1 intersects a C^-–segment of P_2, and the sequence$\{b_n\}$ as the points for which a C^+–segment of P_2 intersects aC^-–segment of P_1. Then as $n \to \infty$,

$$a_n \to C,$$

$$b_n \to C$$

and hence

$$a_n - b_n \to 0.$$

Now suppose $\psi = 0$ on the boundary $\partial\Omega$. As Ω must be characteristically convex, ψ may be represented in the form (4.11). Then if $f(\xi) = k_1$ on one C^+–segment of P_1, it must be the case that $f(\xi) = k_1$ on all C^+–segments of P_1, and $g(\eta) = -k_1$ on all C^-–segments of P_1. Similarly, if $f(\xi) = k_2$ on a C^+–segment of P_2 then $f(\xi) = k_2$ on all C^+–segments of P_2, and $g(\eta) = -k_2$ on allC^-–segments of P_2. Thus

$$\psi(a_n) = k_1 - k_2$$
$$\psi(b_n) = k_2 - k_1.$$

Since $a_n \to C$ and $b_n \to C$, this implies that either $k_1 = k_2$ or the limit

$$\lim_{(x,z)\to C} \psi \tag{4.49}$$

is undefined and ψ is discontinuous at C. Since P_1 and P_2 were chosen arbitrarily, the condition $k_1 = k_2$ is equivalent to $\psi \equiv 0$.

Alternatively, as $n \to \infty$, $a_n - b_n \to 0$. Since $\psi(a_n) = -\psi(b_n)$, ψ may be viewed as an oscillatory function the period of which tends to zero approaching the corner.

If it can be assumed that ψ is analytic on Ω then it is clear that C must represent an essential singularity of ψ. The non–existence of the limit (4.49) implies that C cannot be a removable singularity, but nor can it be a pole since ψ remains bounded on Ω. These observations are consistent with the behaviour exhibited by the solutions (4.43) and the solutions given by Wunsch[47] for a subcritical wedge.

Again, it is argued that these singularities correspond to sources and sinks of internal tide motion. The subcritical topography of the corner is incapable of reflecting an incoming wave; energy carried by such a wave must propagate into the corner. For the energy balance of the system to be maintained the corner must act as an energy sink. Correspondingly, wave energy emanating from the region

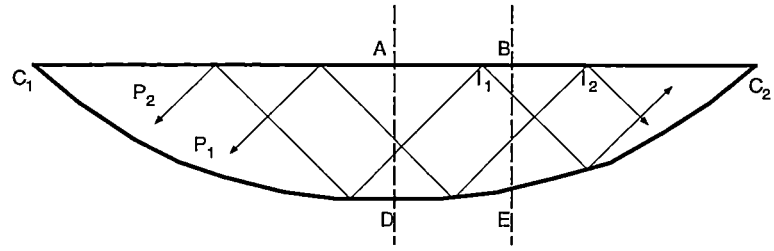

Figure 4.4: Example possessing at least one source or sink.

must have originated at the corner, in which case the corner can be interpreted as a source.

It is important to note that these singularities are not purely a feature of the homogeneous problem, but play an important role in maintaining the energy balance of the inhomogeneous problem as well, as the following example demonstrates.

Consider the region Ω bounded by the purely subcritical topography depicted in Figure 4.4, and suppose $\psi = 0$ everywhere on the boundary $\partial\Omega$ except on the segment AB, where $\psi = 1$. Let P_1 denote a characteristic path in Ω that does not intersect the segment AB, and let P_2 denote a characteristic path that does.

Now consider that component of Ω that is to the left of AD. By the argument presented at the start of this section, ψ will have a singularity at C_1, unless there exists some k_1 such that $f(\xi) = -g(\eta) = k_1$ on those portions of P_1 and P_2 to the left of AD. Similarly, by considering that component of Ω that is to the right of BE, it can be shown that ψ will have a singularity at C_2 unless there exists a constant k_2 such that $f(\xi) = -g(\eta) = k_2$ on those portions of P_1 and P_2 to the right of BE.

But if $f(\xi) = -g(\eta) = k_1$ to the left of AD and $f(\xi) = -g(\eta) = k_2$ to the right of BE, ψ cannot satisfy the boundary conditions at both I_1 and I_2. Thus ψ must possess a singularity at either C_1 or C_2.

Given the physical interpretation of these singularities as sources and sinks,

these results are to be expected, arising from the need to maintain the energy balance in an inviscid system. What is surprising is that it can be shown that discontinuities at corner points are prevalent amongst solutions for supercritical corners too.

Arbitrary Corners

Consider now an arbitrary region Ω with a corner at the origin, bounded above by $z = 0$ and below by a smooth curve parametrised as

$$x = x(\tau) \tag{4.50}$$

$$z = z(\tau) \tag{4.51}$$

such that $x(0) = z(0) = 0$. It can be shown that non–trivial analytic solutions of the homogeneous problem can only exist at such a corner if the corner point is right angled.

Let $\psi = 0$ on both $z = 0$ and $(x(\tau), z(\tau))$. Then in a characteristically convex neighbourhood of the corner, ψ may be represented as

$$\psi(x, z) = f(x - z/c) - f(x + z/c), \tag{4.52}$$

where f satisfies the functional equation

$$0 = f(x(\tau) - z(\tau)/c) - f(x(\tau) + z(\tau)/c). \tag{4.53}$$

In general, this equation cannot be solved by the method of Manton and Mysak[33] described in Section 3.4.2. This procedure assumes the solution is analytic in c, yet it has already been seen that there are cases for which the model is not structurally stable under perturbations of c. Instead, a solution may be obtained by expanding in a Taylor series about the corner point.

Since the lower boundary is smooth, $x(\tau)$ and $z(\tau)$ will possess derivatives of all orders, and without loss of generality it may be assumed that at least one

of $x'(\tau)$ or $z'(\tau)$ is non–zero at the origin. Expanding (4.53) in a Taylor series about the origin and equating coefficients of t yields the system of equations

$$0 = 0 \tag{4.54}$$

$$0 = f'(0)\left[\left(x'(0) - \frac{z'(0)}{c}\right) - \left(x'(0) + \frac{z'(0)}{c}\right)\right] \tag{4.55}$$

$$\begin{aligned} 0 = {} & f''(0)\left[\left(x'(0) - \frac{z'(0)}{c}\right)^2 - \left(x'(0) + \frac{z'(0)}{c}\right)^2\right] \\ & + f'(0)\left[\left(x''(0) - \frac{z''(0)}{c}\right) - \left(x''(0) + \frac{z''(0)}{c}\right)\right] \end{aligned} \tag{4.56}$$

$$\begin{aligned} 0 = {} & f'''(0)\left[\left(x'(0) - \frac{z'(0)}{c}\right)^3 - \left(x'(0) + \frac{z'(0)}{c}\right)^3\right] \\ & + 3f''(0)\left[\left(x'(0) - \frac{z'(0)}{c}\right)\left(x''(0) - \frac{z''(0)}{c}\right)\right. \\ & \left. - \left(x'(0) + \frac{z'(0)}{c}\right)\left(x''(0) + \frac{z''(0)}{c}\right)\right] \\ & + f'(0)\left[\left(x''(0) - \frac{z''(0)}{c}\right) - \left(x''(0) + \frac{z''(0)}{c}\right)\right] \end{aligned} \tag{4.57}$$

$$\vdots$$

$$\begin{aligned} 0 = {} & f^{(n)}(0)\left[\left(x'(0) - \frac{z'(0)}{c}\right)^n - \left(x'(0) + \frac{z'(0)}{c}\right)^n\right] \\ & + F_n(x^{(n)}(0), z^{(n)}(0), x^{(n-1)}(0), z^{(n-1)}(0), \ldots, x'(0), z'(0)) \end{aligned} \tag{4.58}$$

$$\vdots$$

where F_n is a function such that

$$F_n(0, 0, 0, \ldots) = 0. \tag{4.59}$$

Then if for all n

$$\left(x'(0) - \frac{z'(0)}{c}\right)^n - \left(x'(0) + \frac{z'(0)}{c}\right)^n \neq 0, \tag{4.60}$$

the system (4.54) – (4.58) may be solved in sequence to yield

$$f^{(n)} = 0, \tag{4.61}$$

implying $f(t) \equiv 0$.

Since $x'(t)$ and $z'(t)$ must be real, (4.60) is equivalent to

$$x'(0) \neq 0 \quad \text{or} \quad z'(0) \neq 0, \tag{4.62}$$

that is, the corner cannot be a right angle nor can the lower boundary approach the surface $z = 0$ tangentially. (In what follows this second interpretation, being of little physical interest, will be ignored).

When (4.62) is satisfied, the only solution of the homogeneous problem which is analytic at the corner is $\psi \equiv 0$. Given the analysis presented at the beginning of this section, for a subcritical corner this is to be expected. But why a supercritical corner that is not right angled should not possess analytic solutions remains unclear.

Some simple examples of this phenomenon can be generated via c–conformal mapping.

As an example of a right angled corner, the c–conformal map used in the previous chapter to map a square to a circle can also be used to map a rectangle to a semi–circle. Defining

$$r(x, z) = f(x + z) + f(x - z) \tag{4.63}$$

$$s(x, z) = f(x + z) - f(x - z) \tag{4.64}$$

when $c = 1$ the natural modes for a semi–circle bounded above by $z = 0$ and below by $x^2 + z^2 = R^2$ are given by

$$\psi_k(x, z) = \sin \frac{k\pi r(x, z)}{2R^2} \sin \frac{k\pi s(x, z)}{2R^2}, \tag{4.65}$$

where

$$f(\tau) = \tau^2 \operatorname{sgn} \tau. \tag{4.66}$$

In this case the corners $(-R, 0)$ and $(R, 0)$ are right angled and the solutions (4.65) are analytic there.

But consider the quadrilateral with corners

$$\{(0,0),\ (1,0),\ (1/5,-4/5),\ (4/5,-4/5)\}.$$

When $c = 1$ this can be mapped to the the unit square with corners

$$\{(0,0),\ (1,0),\ (0,-1),\ (1,-1)\}$$

by the c–conformal map defined by (4.63) and (4.64), with f defined as

$$f(\tau) = \begin{cases} 5/6\tau & \tau \leq 0 \\ \tau/2 & 0 < \tau \leq 1 \\ (5\tau - 2)/6 & \tau > 1. \end{cases} \tag{4.67}$$

Thus the natural modes for the quadrilateral are given by

$$\psi_k(x,z) = \sin(k\pi r(x,z)) \sin(k\pi s(x,z)), \tag{4.68}$$

in agreement with the solution given by Cushman–Roisin *et al.*[17]. For this example the corners are not right angles, and examining (4.67) it is seen that the ψ_k have discontinuous first derivatives there.

Even given these examples, it remains unclear why the homogeneous problem on a supercritical corner should possess analytic solutions only when the corner is right angled.

4.4.2 Existence and Uniqueness

In the examples presented in the chapter to date, it has been seen that the inviscid model exhibits very different properties depending on the nature of the regions characteristic paths. This idea extends naturally to arbitrary regions.

Consider first an arbitrary closed basin Ω.

For any single characteristic path, there are only two possibilities: either the path forms a characteristic circuit, or it is of infinite length (as before, characteristics passing through a corner can be considered limiting cases). The examples

presented in the chapter to date have all been particularly simple in this respect, in that either all characteristic paths have been characteristic circuits, or all the characteristic paths have been of infinite length. It shall be argued that the number of characteristic paths that form characteristic circuits is a crucial factor in determining the behaviour of the solution.

If the region Ω contains no characteristic circuits then all paths are of infinite length and a c–form satisfying the required boundary conditions may be constructed with the procedure described for the subcritical basin in Section 4.3.2. Then providing the resulting c–form is not singular in Ω, a solution can be found for any choice of Dirichlet boundary data. As discussed in Section 4.3.2, this solution will not be unique, but it is conjectured that if Ω contains only a finite number of characteristic paths then any strong solution will be unique in the sense of its Fourier representation.

When Ω does contain a characteristic circuit, say $ABCD\ldots XYZ$, then as was the case for the example of a rectangular basin, a finite system of linear equations of the form

$$\begin{aligned} g(AB) + f(BC) &= \psi(B) \\ f(BC) + g(CD) &= \psi(C) \\ &\vdots \\ g(YZ) + f(ZA) &= \psi(Z) \\ f(ZA) + g(AB) &= \psi(A) \end{aligned}$$

may be constructed for the values of f and g on $ABCD\ldots XYZ$, where again $f(AB)$ denotes the values of the function f on the characteristic segment AB, and $\psi(B)$ the value of ψ at a boundary point B. This system may be reduced to a constraint of the form

$$\psi(A) - \psi(B) + \psi(C) \ldots + \psi(Y) - \psi(Z) = 0, \tag{4.69}$$

which must be satisfied if the above system is to be consistent and a solution ψ is to exist. If this constraint is satisfied the system of equations is under–determined and the solution is again not unique. Then if all characteristic paths contained in Ω are characteristic circuits, the model can only possess a solution when the constraint (4.69) is satisfied on each circuit.

Obviously this argument extends to the case where there exists some non–trivial subset of Ω in which characteristic circuits are dense. What is not so clear is what occurs when only a few characteristic paths in the basin form characteristic circuits.

Suppose that the number of characteristic circuits is countable. Then these circuits must form a subset of Ω of measure zero, and applying the procedure of Section 4.3.2 to the remaining characteristic paths will define a c–form almost everywhere on Ω that satisfies the required boundary conditions almost everywhere on $\partial\Omega$. Since this c–form is defined almost everywhere, if it is not singular, it will define a weak solution on Ω. Thus it may still be possible to find a weak solution in the presence of a countable number of characteristic circuits, irrespective of whether the boundary conditions satisfy the constraints (4.69) imposed by these circuits or not.

This would suggest that due to its extreme symmetry, the rectangular basin is a special case amongst supercritical basins, and may not be as indicative of the general case as it would first seem.

Although it has been shown that the existence of an uncountable number of characteristic circuits implies the existence of conditions for which the inviscid model has no solution, it has been shown that these solutions correspond to resonant internal tide motion. Thus these arguments lend only weak support to the conjecture of Cushman–Roisin *et al.*[17] that the existence of closed circuits implies resonance, although this has been demonstrated to be the case for a rectangular basin.

These remarks generalize naturally to arbitrary topographies. Characteristic

paths that intersect those portions of the boundary where the radiation condition is applied may be treated with the method of Craig, described in Section 3.4.1. On the remainder of the region the analysis proceeds as above.

4.5 Towards a Viscous Model

The observations of the preceding sections not only imply that the purely inviscid model is numerically intractable, but are also of relevance to a viscous study of internal tide motion.

Summarizing the conclusions of the preceding sections, it has been shown that for the inviscid model (3.1) on a basin:

1. if the basin contains an uncountable number of characteristic circuits, then there will exist boundary conditions for which (3.1) has no solution
2. in those instances where a solution does exist, it is either not unique, structurally unstable, or both.
3. at a subcritical corner, the solution is likely to possess a type of singularity corresponding to a source or sink of internal tide motion.

These factors combined with the vagaries of numerical error clearly indicate the impracticality of obtaining numerical solutions of the purely inviscid model. The inviscid theory can be used to detect resonant solutions, but only through invoking the structural stability of the corresponding viscous model.

Given the conjecture of Cushman–Roisin *et al.*, it will be those instances in which the inviscid model possesses no solution that will be of primary interest, for it is these instances that correspond to resonant solutions, and resonant solutions can be expected to dominate the motion. But it is not possible from the inviscid theory alone to determine numerically whether (3.1) will possess a solution on a given basin, since it is not possible to establish the existence of an uncountable number of characteristic circuits from a numerical analysis.

But suppose the basin contains a characteristic path which almost intersects itself to form a characteristic circuit. By taking small perturbations of the the boundary this path could be made to form a characteristic circuit. But further, since the boundary is continuous, the characteristic paths surrounding this path could also be made to form characteristic circuits by taking small perturbations of the boundary and the basin can be made resonant. If the viscous model is assumed structurally stable, then under this viscous model the original basin must have been near resonant and can be expected to display properties similar to those of the resonant basin. An example of this can be seen in Section 7.2.

However, the structural stability of the viscous model should not be carried too far. When implementing their finite difference schemes, both Cushman–Roisin *et al.*[17] and Tverberg *et al.*[45] represent the boundary only approximately, replacing the true topography by a polygonal path of horizontal and vertical segments constructed so as to pass through the nodes of the chosen finite difference grid.

Cushman–Roisin *et al.* then claim that "multiple resonance is the rule rather than the exception" — but this observation is largely a product of the manner in which they have chosen to represent the boundary. Approximating the boundary by a path that passes through the nodes of a grid greatly increases the regularity of the region, increases the likelihood of characteristic circuits and hence resonant solutions.

As an extreme example, consider a subcritical basin. When the boundary is accurately represented there can be no characteristic circuits. But under the scheme employed by Cushman–Roisin *et al.* and Tverberg *et al.* the boundary is approximated by a stepped topography and characteristic circuits can form. In this example, approximating the boundary introduces characteristic circuits and hence resonant solutions where there were none previously.

The approximation is also deficient regarding the representation of corners. It has been seen that supercritical and subcritical corners are fundamentally

different, and that amongst supercritical corners, right angled corners constitute a further special case. Yet the boundary approximation used by Cushman–Roisin *et al.*[17] and Tverberg *et al.*[45] is only capable of accurately representing one of these three cases — that of right angled corners.

But even when the boundary is accurately represented, subcritical corners may pose difficulties for the numerical solution of a viscous model. It has been seen that the solution of the inviscid model often displays a particular form of singularity at a subcritical corner, becoming increasingly oscillatory approaching the corner. Although the viscous solution cannot be expected to display a singularity at the corner point, it is unclear what level of fine scale structure will be present in the corresponding viscous solution. This structure would need to be resolved by the numerical procedure and poses obvious problems. An analytic solution of the viscous model for a subcritical corner would prove an extremely valuable indicator in relation to this question.

4.6 Summary

This chapter has completely classified the possible behaviours of the inviscid model on a closed basin. This study clearly shows that on a closed basin the inviscid model is numerically intractable, and lends strong support to the conjecture of Cushman–Roisin *et al.*[17] linking characteristic circuits and resonance.

The next chapter digresses to discuss the importance of accurately representing the boundary when solving the inviscid model with finite difference methods, before returning to investigate a viscous model of internal tide motion in Chapter 6.

Chapter 5

Finite Differences – Representation of the Boundary.

Previous chapters have concentrated on characteristic based solution methods for the inviscid model (3.1). Several authors prescribe a more traditional finite difference approach. Amongst these there exists a group that simplify the numerical problem by approximating the topography of the region.

But the results of the previous chapter suggest that for a closed basin at least, such an approximation may be inappropriate. For more general regions the implications remain unclear. The chapter begins by numerically demonstrating that for the inviscid model on a shelf region this approximation results in an unacceptable level of error.

The second half of the chapter demonstrates that the approximation of the boundary may be avoided through c–conformal mapping, and a simple numerical technique for generating the required c–conformal maps is devised. This technique has the advantage that it can be implemented as a preprocessing stage, allowing existing solution techniques to be applied largely unaltered.

5.1 An Empirical Study

Noting certain difficulties associated with the existing characteristics based methods, Cushman–Roisin *et al.*[17] propose a finite difference technique for the solution of the inviscid model (3.1) on a closed basin. But as discussed in the previous chapter these authors find it necessary to re–introduce viscous terms to the model to ensure the convergence of their numerical method. In a later work Tverberg *et al.*[45] extend this same technique to the treatment of shelf topographies and the radiation condition.

When implementing their respective finite difference schemes, these authors approximate the true bathymetry by a polygonal path passing through the nodes of the selected finite difference grid. Although not essential to the finite difference process, this procedure greatly simplifies the calculation of the discretized equations.

The analysis of the previous chapter suggests that for the purely inviscid model on a closed basin such an approximation may be unacceptable — small variations in the shape of the boundary may drastically alter the nature of the purely inviscid solution. This is largely due to the formation of characteristic circuits, and thus for a shelf region the implications of approximating the boundary remain unclear.

In this section an empirical study is made of this approximation in relation to shelf topographies. Two separate finite difference schemes are implemented, one that correctly represents the shape of the boundary and one that implements the approximation described above, and the results of these two schemes are compared.

Approximating the Boundary

When implementing their finite difference schemes both Cushman–Roisin *et al.*[17] and Tverberg *et al.*[45] perturb the boundary so that it passes through the nearest

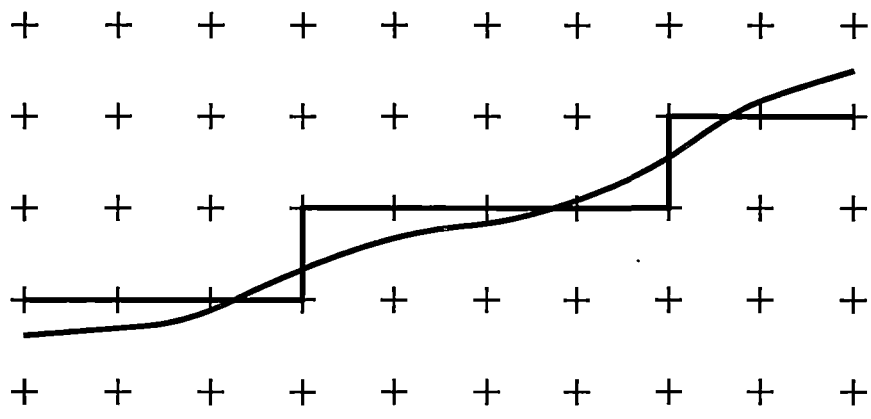

Figure 5.1: Approximating the boundary.

node of the chosen finite difference grid. If, for example, the crosses of Figure 5.1 represent the nodes of the grid, then under this strategy the two topographies depicted in the figure are in effect indistinguishable, and the finite difference scheme will result in the same set of discretized equations for both.

Consider solving this same problem by the method of Craig described in chapter 3. Suppose the smooth topography is everywhere subcritical. Then each characteristic path striking this topography will be "transmitted" as in Figure 3.4(a) of Section 3.4.1. But the stepped topography contains both subcritical and supercritical components, and hence some characteristics striking this topography may be "reflected", as in Figure 3.4(b). Thus the two systems of linear equations constructed from these paths under Craig's technique would be very different, and it therefore seems unlikely that Craig's technique would yield similar solutions for the two topographies.

Arguing from a physical standpoint, the stepped, supercritical topography is capable of reflecting a component of any wave energy incident on the shelf, whereas the smooth subcritical topography is not. Thus in terms of the energy balance of the system it again seems unlikely that these two topographies would yield solutions of a similar character.

The implications of this argument for a finite difference scheme are unclear.

It may be that the differences in the two solutions are on a scale too small to be accurately resolved by the finite difference grid. If this is the case, then within the assumptions of the finite difference model the finite difference solution would represent a valid approximation to both solutions. Under this scenario, any problems associated with the approximation of the boundary could be resolved by sufficiently decreasing the scale of the grid, thereby increasing the resolution of the finite difference scheme.

Nevertheless, it is not clear that the small variations in the boundary will result in small variations in the solution. Indeed, in the previous chapter it was found that for a closed basin this is not the case.

Numerical Methods

To investigate this issue further, a series of numerical experiments was carried out. Two forms of finite difference scheme were implemented. Both schemes were fully implicit, differing only in the manner in which the boundary was represented.

The first scheme — the approximation scheme — was based on standard second order central differences formulae applied in conjunction with the approximation of the boundary described above. Since the approximate boundary passes through the nodes of the grid, the boundary conditions were easily implemented in terms of central differences.

In the second scheme — the interpolation scheme — central differences were used within the body of the region, but at the boundary non central difference formulae were used so that the boundary conditions could be accurately represented without the need to approximate the boundary. In effect this scheme perturbed the outermost nodes of the finite difference grid so they would lie on the boundary, rather than perturbing the boundary itself. For example, when applying the finite difference discretization to the topography depicted in Figure 5.2(a), the two irregularly spaced grid points D' and E' (circled) are introduced and the discretization is performed on $ABCD'E'$ rather than $ABCDE$.

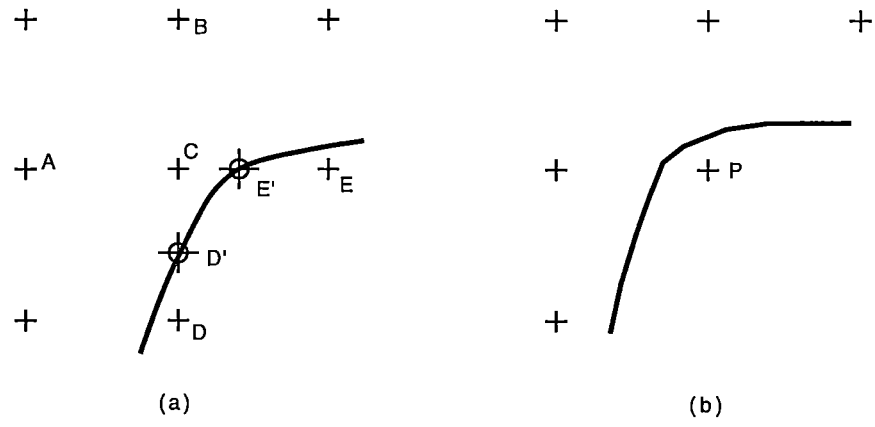

Figure 5.2: Interpolating to the boundary.

The appropriate non central difference formulae required to implement the boundary conditions on this uneven grid may be derived from Taylor's theorem. Since

$$f(x-h_1) = f(x) - f'(x)h_1 + \frac{1}{2}f''(x)h_1^2 + O(h_1^3) \tag{5.1}$$

$$f(x+h_2) = f(x) + f'(x)h_2 + \frac{1}{2}f''(x)h_2^2 + O(h_2^3), \tag{5.2}$$

solving for $f''(x)$ yields

$$f''(x) = \frac{h_2 f(x-h_1) - (h_1+h_2)f(x) + h_1 f(x+h_2)}{h_1 h_2 (h_1+h_2)/2} + O(h_1, h_2). \tag{5.3}$$

Note that the error term in this formula is of order h, rather than order h^2 as in the central differences case. Similarly

$$f'(x) = \frac{-h_2^2 f(x-h_1) + (h_2^2 - h_1^2)f(x) + h_1^2 f(x+h_2)}{h_1 h_2 (h_1+h_2)} + O(h_1, h_2). \tag{5.4}$$

These formulae reduce to the more common central differences formulae when $h_1 = h_2$.

It is not possible to implement the interpolation procedure by retaining a regular grid (Figure 5.2(b)) and calculating differences at the boundary from an external grid point P the value of which is determined by extrapolation. For this

would imply that it is possible to consistently extend the definition of the stream function through the boundary, and it is known from Chapter 3 that this is not possible for an arbitrary domain.

Both schemes were implemented as fully implicit finite difference schemes, and the resulting sparse matrix inverted by standard LU factorization techniques. Although perhaps not as efficient as an explicit stepping procedure like that of Chuang and Wang[9], this approach ensures that the primary difference in the two schemes is the manner in which the boundary is represented, rather than some subtle interaction between the representation of the boundary and the method chosen to solve the resulting discretized equations.

As a preliminary test of the implementations, both procedures were applied to a simple stepped topography chosen so as to pass through the nodes of the selected finite difference grid, and the results compared to the equivalent solution obtained by the boundary collocation method described in Chapter 3. Since the topography does pass through the nodes of the grid, the two finite difference schemes should yield the same solution. All three solutions were found to be in good agreement.

Comparison

Figure 5.3 shows the results of the interpolating scheme for the shelf region bounded below by $z = h(x)$ where

$$h(x) = \begin{cases} -1.0, & \text{if } x \leq 0.2 \\ -0.7 + 0.3\sin(5\pi(2x-1)/6), & \text{if } 0.2 < x \leq 0.8 \\ -0.4, & \text{if } x > 0.8 \end{cases} \tag{5.5}$$

and $c = 0.8$, with the number of grid points in the x direction $n_x = 40$ and the number of grid points in the z direction $n_z = 50$. The boundary conditions were

chosen as

$$\psi(x, h(x)) = 0 \tag{5.6}$$

$$\psi(x, 0) = B(x, 0) \tag{5.7}$$

where $B(x)$ denotes the barotropic forcing function

$$B(x, z) = (x - L)(1 - z/h(x)), \tag{5.8}$$

described by Craig[14]. The topmost diagram in the figure represents the real component $\Re\{\psi\}$, and the bottom–most diagram the imaginary component $\Im\{\psi\}$. The real component $\Re\{\psi\}$ is largely dominated by the barotropic forcing $B(x, z)$ and the middle diagram of the trio shows the difference $\Re\{\psi\} - B(x, z)$.

The corresponding solution obtained by the approximation method is shown in Figure 5.4. The differences in the two solutions are slight.

But a very different situation arises if the same problem is solved with $c = 3$. Figure 5.5 shows the results of the interpolating method when $n_x = 90$ and $n_z = 30$, while Figure 5.6 shows the corresponding results of the approximation method. Figure 5.7 shows the results of the approximation scheme when $n_x = 120$ and $n_z = 45$. In this example there is a quite marked difference between the solutions produced by the two methods.

Comparing Figures 5.5 and 5.6 it can be seen that the approximation of this subcritical topography has introduced a spurious "noise" component to the solution. A comparison of Figures 5.6 and 5.7 shows that this noise component is of a spatial scale comparable to that of the selected finite difference grid, implying that the problem cannot be resolved by increasing the resolution of the grid. These results bear out the reservations expressed above.

These experiments were repeated for several different topographies, and the above behaviour was found to be typical. Solutions for supercritical topographies where largely unaffected whereas approximating a subcritical boundary in this

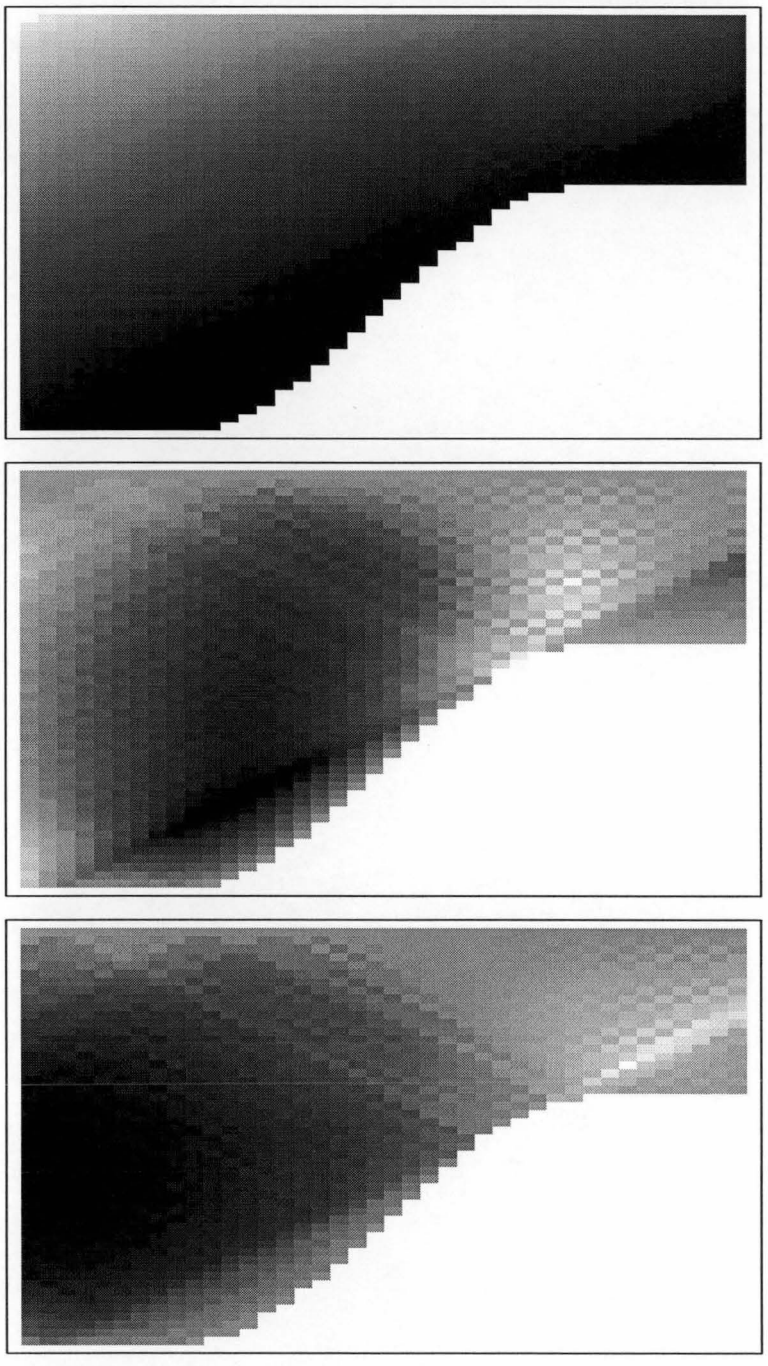

Figure 5.3: Solution generated by interpolating scheme when $c = 0.8$, $n_x = 40$ and $n_z = 50$. Top $\Re\{\psi\}$, middle $\Re\{\psi\} - B(x, z)$, bottom $\Im\{\psi\}$.

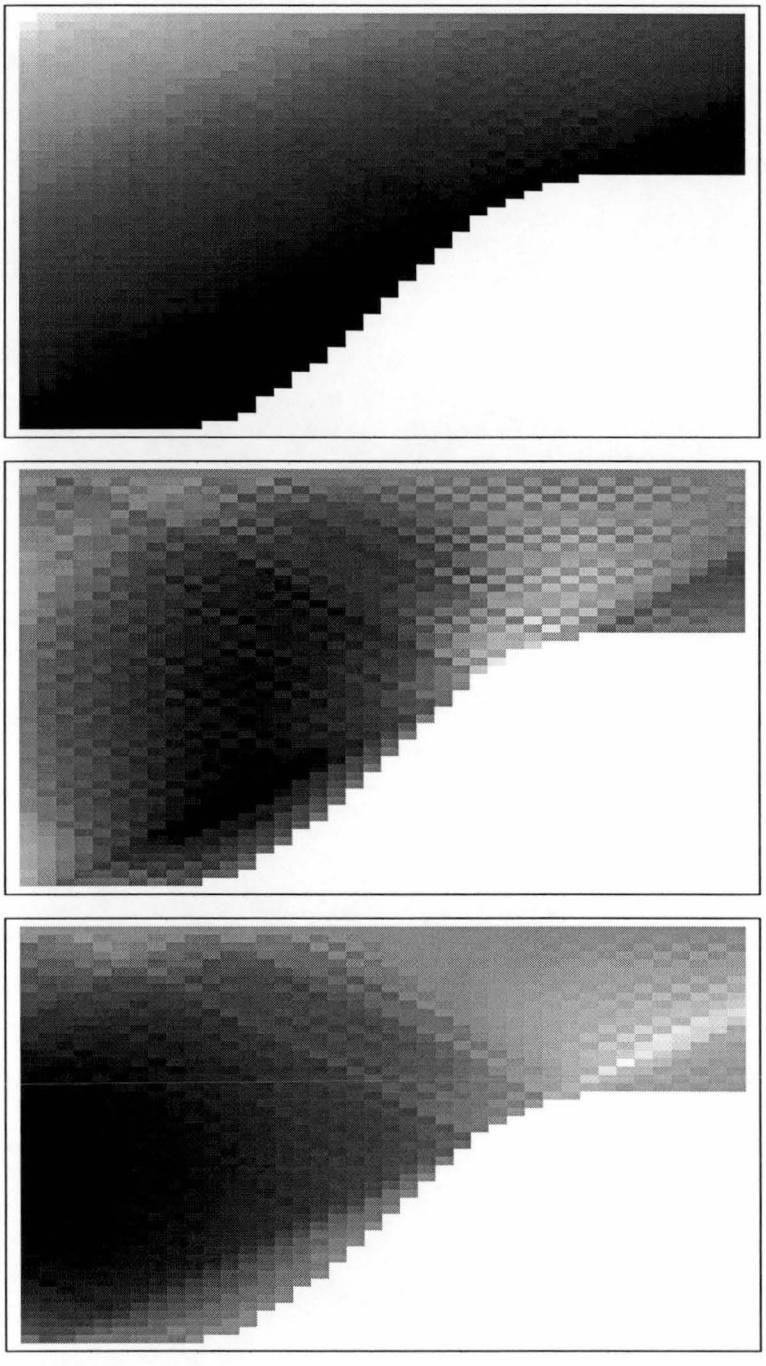

Figure 5.4: Solution generated by approximation scheme when $c = 0.8$, $n_x = 40$ and $n_z = 50$. Top $\Re\{\psi\}$, middle $\Re\{\psi\} - B(x, z)$, bottom $\Im\{\psi\}$.

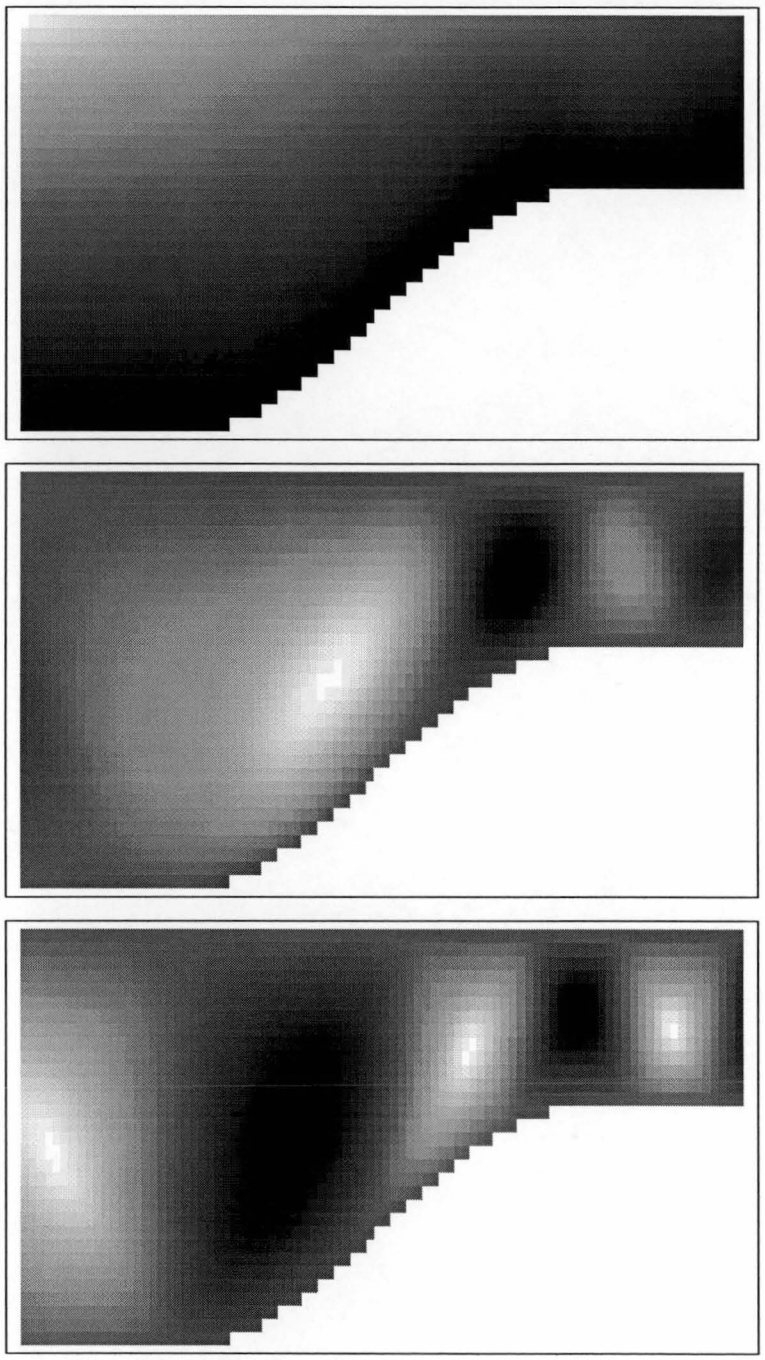

Figure 5.5: Solution generated by interpolating scheme when $c = 3$, $n_x = 90$ and $n_z = 30$. Top $\Re\{\psi\}$, middle $\Re\{\psi\} - B(x, z)$, bottom $\Im\{\psi\}$.

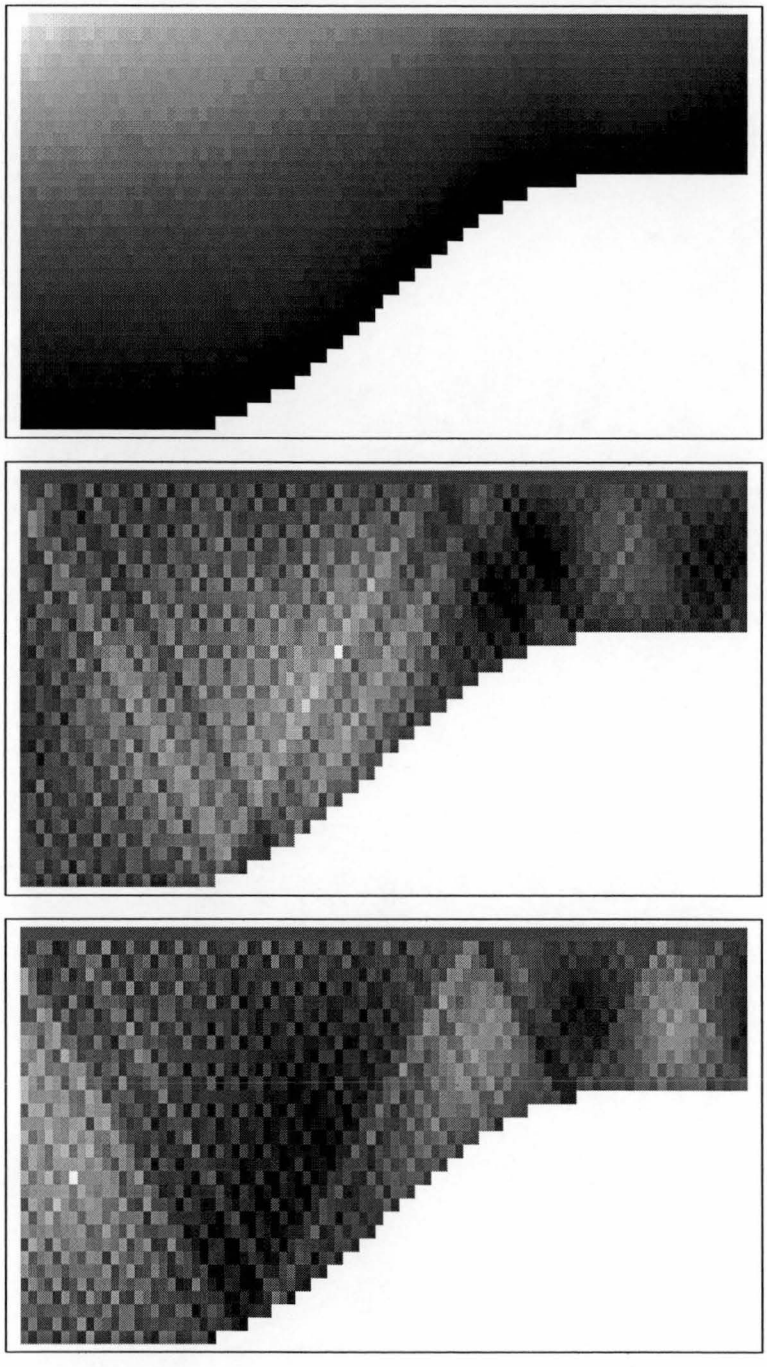

Figure 5.6: Solution generated by approximation scheme when $c = 3$, $n_x = 90$ and $n_z = 30$. Top $\Re\{\psi\}$, middle $\Re\{\psi\} - B(x, z)$, bottom $\Im\{\psi\}$.

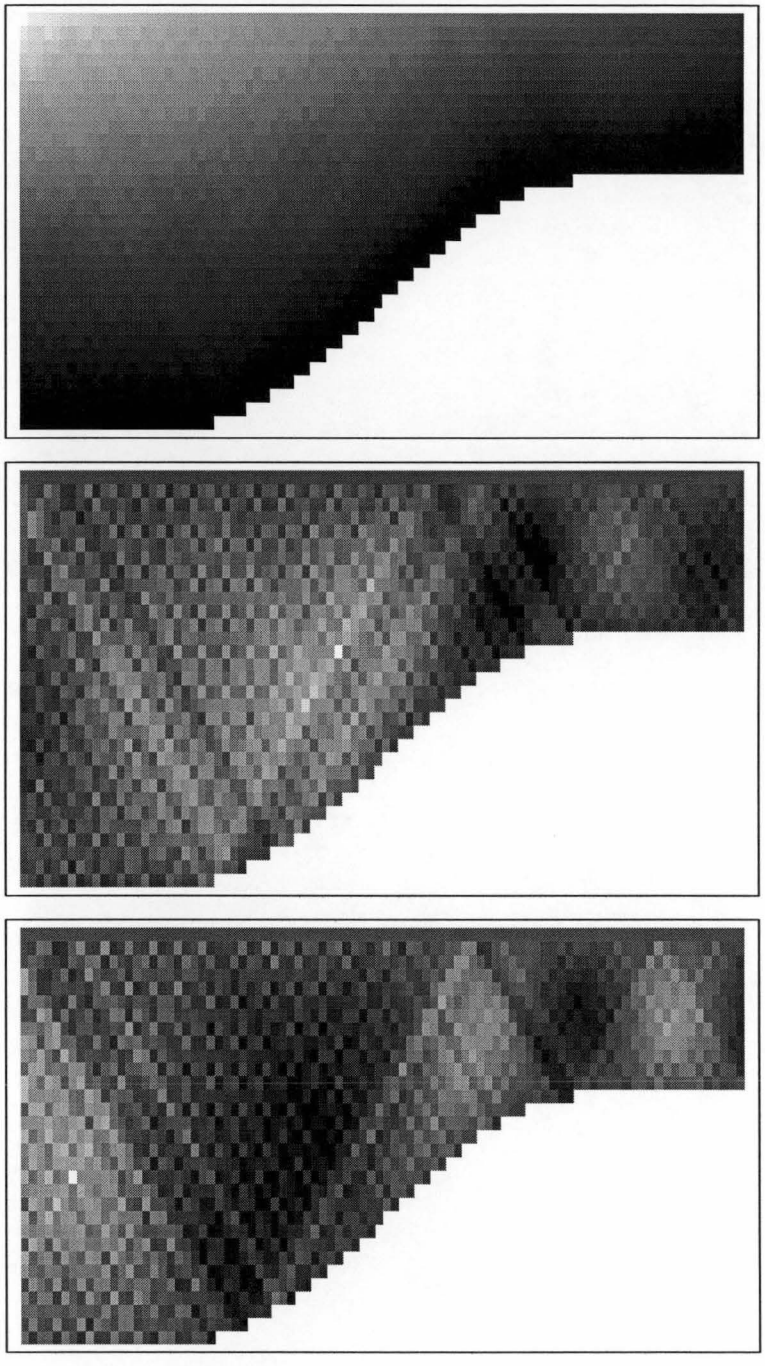

Figure 5.7: Solution generated by approximation scheme when $c = 3$, $n_x = 120$ and $n_z = 45$. Top $\Re\{\psi\}$, middle $\Re\{\psi\} - B(x, z)$, bottom $\Im\{\psi\}$.

manner resulted in the introduction of an extraneous noise component like that observed above.

It is conjectured that subcritical topographies are more susceptible to this problem because approximating the boundary introduces supercritical components where there were none before. In the supercritical case, both the true boundary and the approximate boundary are largely supercritical in nature.

What is perhaps most interesting about this phenomenon is that it is not observed by Cushman *et al.* or Tverberg *et al.* This can only be attributed to the retention of viscous terms in their models. There are two possible mechanisms which could explain the absence of the noise component. Retention of the viscous terms will result in some form of boundary layer phenomenon. This boundary layer could be acting as a buffer, in effect smoothing the form of the boundary. Alternatively, as the noise component is of a particularly short spatial scale it would be heavily attenuated by any viscous interaction. Thus the noise component could still be present, but is less apparent, in the viscous solution.

Nevertheless, it remains the case that approximating the boundary provides an unacceptable source of error. Although the viscous terms may tend to counter the introduced error, this does not justify not eliminating the error in the first instance. For there must exist some point at which viscous effects will fail to dominate and the noise component will re–emerge.

Furthermore, the observations of this section raise question of how accurately the boundary need be represented. It is clearly not practicable to represent a real bathymetry exactly. Although it is reassuring that viscous effects appear to obviate the need to represent the boundary exactly, for a purely inviscid model the question remains.

5.2 Transform Techniques

It is clear from the results of the previous section that the boundary must be accurately represented when solving (3.1) via finite difference techniques. This is not impossible, as the interpolating finite difference scheme of the previous section demonstrates, but such a scheme is more difficult to construct and has the disadvantage of being of only first order accuracy. As an alternative, the finite difference scheme proposed by Chuang and Wang[9] avoids these difficulties by first introducing the change of co–ordinates

$$r = x \qquad s = z/h(x) \tag{5.9}$$

and solving on the resulting flat bottomed domain. This strategy has the disadvantage of greatly complicating the form the the governing Equation (3.1), and requires a high grid resolution where $h'(x)$ or $h''(x)$ is large. A more natural choice of coordinate transformation is provided by c–conformal mapping. In this way the boundary may be transformed to one better suited to a finite difference solution without complicating the form of the governing equation.

Obtaining the Mapping

The difficulty associated with using c–conformal mapping for the co–ordinate transformation is that of determining a suitable c–conformal map. In this section a simple numerical procedure is devised for generating a c–conformal map from a shelf region Ω to some other shelf region Ω', for which a finite difference grid can be easily constructed such that the new boundary $\partial\Omega'$ passes through the nodes of the grid. In this way the simpler, second order accurate, non–interpolating scheme of the previous section can be applied without misrepresenting the form of the boundary.

Consider the problem of mapping a shelf region Ω to some region Ω' for which a regular finite difference grid may be easily constructed. Under a c–conformal

map, characteristic paths map to characteristic paths. Thus the obvious approach to numerically generating a c–conformal map is to trace a number of characteristic paths in Ω and then associate these paths with characteristic paths in Ω' by some simple heuristic. But as this requires tracing characteristic paths in the original region Ω, it would be simpler and more direct just to solve (3.1) by Craig's method. (In fact, following this line of reasoning it can be shown that if the internal tide problem on Ω can be solved by Craig's method, then there will exist a c–conformal map from Ω to a channel of constant depth). A more efficient methodology must be found.

For classical conformal mapping, if M is a map which takes a closed boundary $\partial\Omega$ to the closed boundary $\partial\Omega'$, Darboux's theorem (Boas[5]) guarantees that the interior of $\partial\Omega$ maps to the interior of $\partial\Omega'$. But as was seen in Chapter 3, the same is not true of c–conformal mapping. If a c–conformal map does not preserve the sub/supercritical nature of the boundary it is possible for portions of the interior of $\partial\Omega$ to map to the exterior of $\partial\Omega'$, as was demonstrated in Figure 3.9.

For use in conjunction with a finite difference scheme, it is desirable (although not essential) that the numerically generated map should preserve the boundary, that is, that the interior of $\partial\Omega$ should map to the interior of $\partial\Omega'$ [1]. This can be achieved by requiring that the mapping preserve the sub/supercritical nature of the boundary. That is, if $p' \in \partial\Omega'$ is the image of $p \in \partial\Omega$ under that map, then if $\partial\Omega$ is subcritical at p, $\partial\Omega'$ should be subcritical at p', and if $\partial\Omega$ is supercritical at p then $\partial\Omega'$ should be supercritical at p'. It is this requirement that forms the basis of the numerical procedure for generating an appropriate c–conformal map.

The process is undertaken in two stages. First a c–conformal map is gener-

[1] However, it may be the alternative that is the more profitable scheme. Consider the mapping from a step to a channel depicted in Figure 3.9. On the channel the problem is trivial to solve. Since the "missing" region (hatched) must lie in the continuation domain of the channel, the solution on this region can be determined by c–unique analytic continuation as described in Section 3.5.1.

ated which takes a shelf region Ω to a shelf region Ω' lower boundary of which consists of only horizontal and vertical line segments. In the second stage the dimensions of this new region are adjusted to better suit the requirements of the finite difference procedure.

First Stage Mapping

For the first stage it is assumed that the c–forms representing the c–conformal map are uniform on Ω (in the sense of Section 3.3), and that the line $z = 0$ representing the upper surface of the shelf region in the xz plane maps to the line $s = 0$ in the rs plane. Then, from Section 3.5.3, on Ω the mapping may be represented in the form

$$r(x,z) = f(x + z/c) + f(x - z/c) \tag{5.10}$$

$$s(x,z) = c(f(x + z/c) - f(x - z/c)) \tag{5.11}$$

where f is some function that is yet to be determined. Henceforth this function will be termed the *kernel* of the c–conformal map.

Let $z = h(x)$ represent the lower boundary of Ω and require that the image of this boundary consist of only horizontal and vertical line segments in the rs plane. This, together with the requirement that the mapping preserve the sub/supercritical nature of the boundary, leads to the conditions

$$f(x + h(x)/c) - f(x - h(x)/c) = s_0 \quad \text{if } \|h'(x)\| < c, \tag{5.12}$$

$$f(x + h(x)/c) + f(x - h(x)/c) = r_0 \quad \text{if } \|h'(x)\| > c \tag{5.13}$$

where r_0 and s_0 are constants in a local sense. That is, r_0 remains constant when the topography is subcritical and s_0 remains constant when the topography is supercritical. These conditions lead to a simple method for determining the kernel f from h.

The algorithm is essentially an explicit stepping method based on (5.12) and (5.13). Let $K = [k_1, k_2]$ denote the interval for which f is known. The method

begins by first arbitrarily choosing f on an interval S, and so initially $K = S$, and then repeatedly applies (5.12) – (5.13) extend K to the left and right.

Although in principle this procedure is straightforward, certain subtleties must be observed to avoid inconsistencies arising from the stepping procedure. The algorithm will be first stated, and then explained in more detail.

Let x_M be the point at which $h(x)$ attains its global maximum h_M, that is x_M is the point of minimum depth. Initially, consider only the case for which the shelf region has two open lateral boundaries and so $h_M \neq 0$. Then the algorithm proceeds as follows

1. Define the *seed interval* S as the interval $[x_M + h_M/c, x_M - h_M/c]$, and set

$$f(t) = t \qquad \forall\, t \in S. \tag{5.14}$$

2. Calculate both r_0 and s_0 at x_M from (5.12) and (5.13) and set

$$r_0^{left} = r_0^{right} = r_0,$$
$$s_0^{left} = s_0^{right} = s_0.$$

3. Choose set of points $X = \{x_1, \ldots x_n\}$ so that

$$x_i \neq x_M, \tag{5.15}$$
$$x_i < x_{i+1}, \tag{5.16}$$
$$x_{i+1} - x_i \ll -1/c \min(h(x_i), h(x_{i+1})), \tag{5.17}$$

X contains all the points at which the $h(x)$ changes from subcritical to supercritical or vice versa, and $[x_1, x_n]$ straddles the region of variable topography described by $h(x)$.

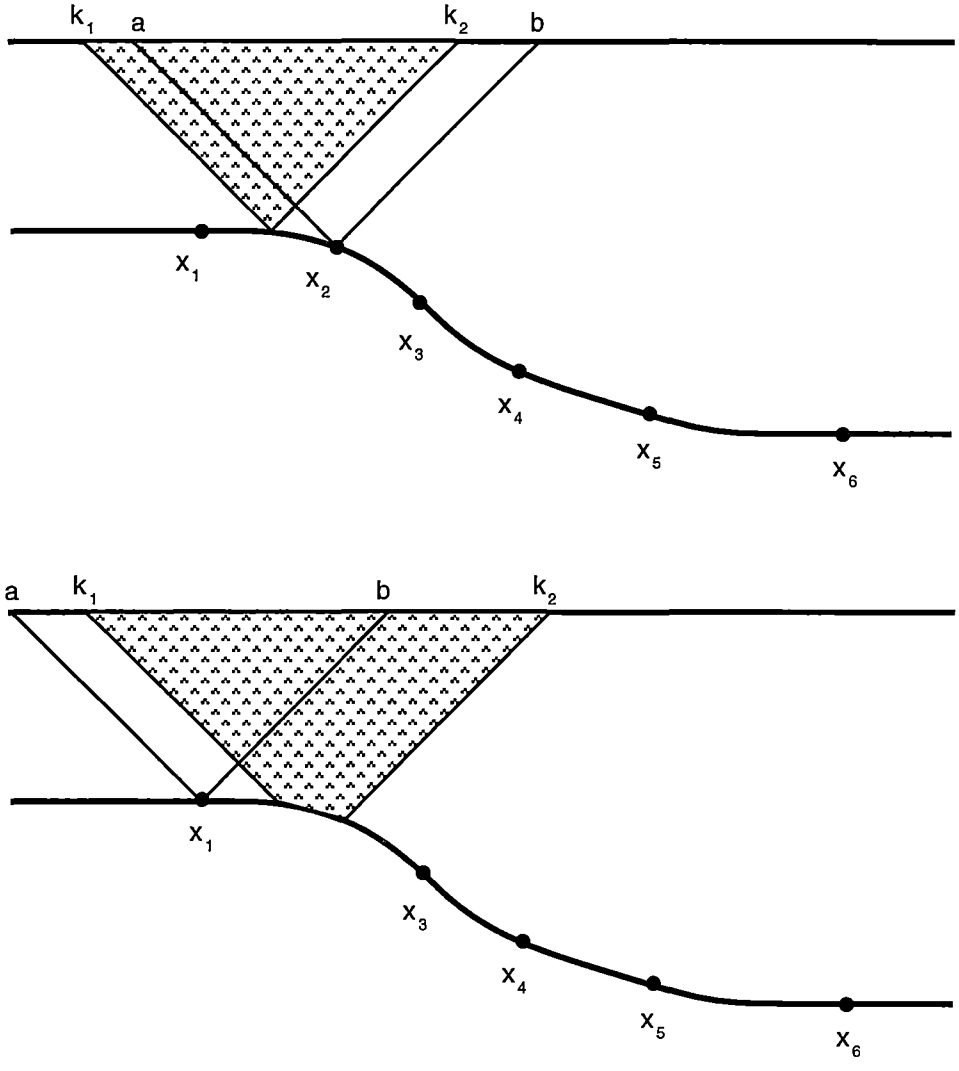

Figure 5.8: Taking the first "step" in the map generating algorithm; top — before, bottom — after. The shaded area indicates the area for which the map is currently known. The next step is taken in the direction which least extends this "known" region.

4. From X construct the set of triples T

$$\{(x_1,\ x_1 + h(x_1)/c,\ x_1 - h(x_1)/c),$$
$$(x_2,\ x_2 + h(x_2)/c,\ x_2 - h(x_2)/c),$$
$$\vdots$$
$$(x_n,\ x_n + h(x_n)/c,\ x_n - h(x_n)/c)\}.$$

5. Select and remove from T the triple (x, a, b) for which $\text{dist}((x, a, b), K)$ is a minimum, where

$$\text{dist}((x,a,b),K) = \begin{cases} \min_{t\in K} |t-b| & \text{if } a \in K; \\ \min_{t\in K} |t-a| & \text{if } b \in K; \\ \infty & \text{otherwise.} \end{cases}$$

6. If $a \in K$,

   (a) Set $r_0 = r_0^{right}$ and $s_0 = s_0^{right}$.

   (b) Calculate $f(b)$ from (5.12) or (5.13), depending upon $h'(x)$ and define f in the interval $[k_2, b]$ by linear interpolation.

   (c) Recalculate both r_0 and s_0 at x with (5.12) and (5.13) and set $r_0^{right} = r_0$, $s_0^{right} = s_0$ and $k_2 = b$.

   Alternately, if $b \in K$,

   (a) Set $r_0 = r_0^{left}$ and $s_0 = s_0^{left}$.

   (b) Calculate $f(a)$ from (5.12) or (5.13) and define f by linear interpolation in the interval $[a, k_1]$.

   (c) Recalculate both r_0 and s_0 at x with (5.12) and (5.13) and set $r_0^{left} = r_0$, $s_0^{left} = s_0$ and $k_1 = a$.

7. Repeat steps 5 – 6 until T is empty.

The heart of the algorithm is step 6, which applies (5.12) or (5.13) to extend K to the left and right. In a sense there are two extension processes occurring simultaneously, one extending K to the left, and one extending K to the right. However, these are not independent — on a strongly supercritical topography one process may require values of f determined by the other, and thus the two must be carried out simultaneously.

Each triple $(x,\ a,\ b)$ corresponds to a pair of function values $f(a)$ and $f(b)$ related by one of (5.12) or (5.13). The algorithm uses this information to build a linear spline representation of f. Extending K with the triple for which $\mathrm{dist}((x,a,b),K)$ is a minimum ensures that the spline is always extended at an endpoint, rather than redefining existing segments of the spline. This, together with the conditions (5.15) – (5.17), guarantees that there will always be at least one triple $(x,a,b) \in T$ for which either $a \in K$ or $b \in K$, but there will never be a triple for which both $a \in K$ and $b \in K$, as this could lead to an inconsistency. It is not essential that the spline process be linear, but a linear spline has the advantage that the inverse of f, and hence the inverse mapping, is easily generated.

Choosing S as described in step 1, makes the initial choice of f arbitrary, as there will exist no triple contained in S other than that used to calculate the initial values of r_0 and s_0. For if such a triple could be constructed, then f would be have to be chosen so as to satisfy one of (5.12) or (5.13) for this triple. The initial form (5.14) of f used in the algorithm is chosen purely for its simplicity, varying this choice gives a limited level of control over the form of the generated c–conformal map.

It is imperative that X contain all the points at which the topography changes between supercritical and subcritical. For this ensures that between any two successive extensions one of r_0 or s_0, depending upon $h'(x)$, will remain constant. (In fact, there are two pairs of r_0 or s_0 — r_0^{left} and s_0^{left}, and r_0^{right} and s_0^{right}, corresponding to the left and right extension processes.)

More general regions

The process for a shelf region with only one lateral boundary is effectively the same, differing only in the initial choice of f and S. There are two cases depending upon whether the topography is subcritical or supercritical at the corner $x = x_M$.

Suppose the topography is supercritical at the corner $x = x_M$ and let x_S denote the transition point closest to the corner at which the topography changes from supercritical to subcritical. If the region to be transformed lies to the right of $x = x_M$ then S must be chosen as $[x_S + h(x_S)/c, x_M]$ and if it lies to the left S must be chosen as $[x_M, x_S - h(x_S)/c]$. This ensures that triples generated from the section of supercritical topography stretching from x_M to x_S will have exactly one ordinate contained in S, and that the extension procedure will expand into the region, rather than away from it. As before f may be chosen arbitrarily on S, and the algorithm proceeds as before.

The procedure is more complicated if the topography is subcritical at the corner. In this case both S and f must be explicitly chosen so as to correctly map a small component of the topography near the corner. In effect the algorithm must be given the correct mapping for a region containing the corner point, and from this it generates the rest of the map. If the topography may be approximated by a linear segment in some interval $[x_M, x_L]$, then S may be chosen as $[x_L + h(x_L)/c, x_L - h(x_L)/c]$ with f chosen as

$$f(t) = \ln(t - x_M). \tag{5.18}$$

The subcritical corner will be of less practical interest, since necessarily the mapping must map the corner to infinity, vastly complicating the implementation of a finite difference scheme on the transformed domain.

A Mathematica script implementing the algorithm described above is given in Appendix A. As an example, Figures 5.10 and 5.9 show the maps generated for the topography represented by (5.5) when $c = 3.0$ and $c = 0.8$.

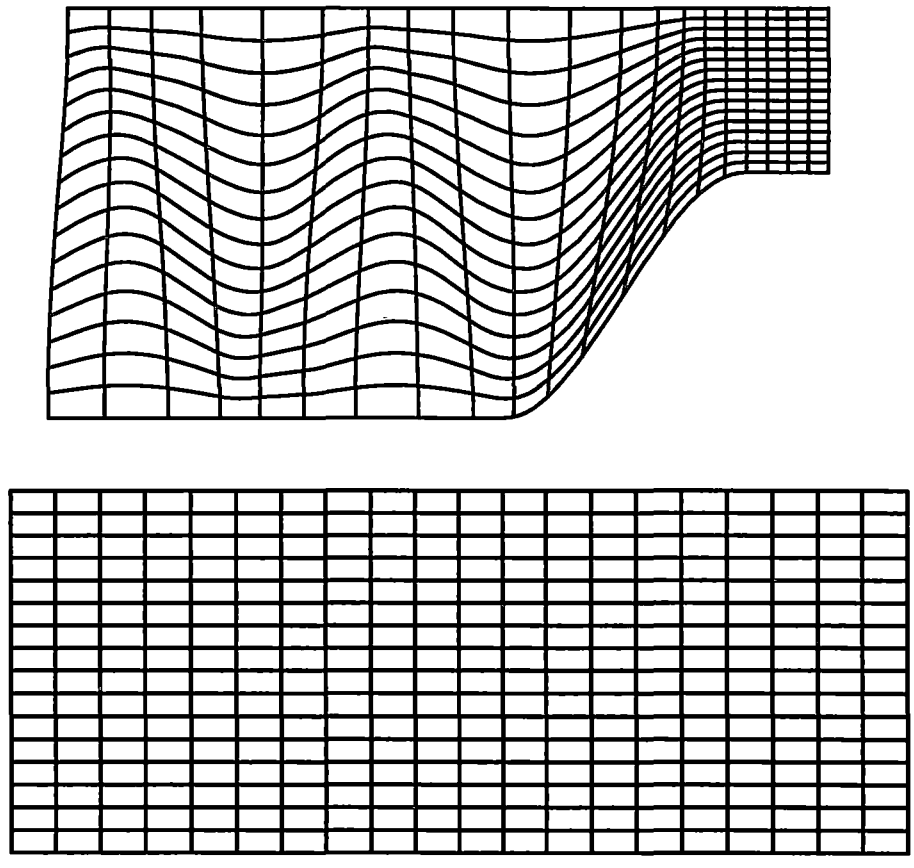

Figure 5.9: When $c = 0.8$ the topography represented by (5.5) is subcritical and maps to a channel.

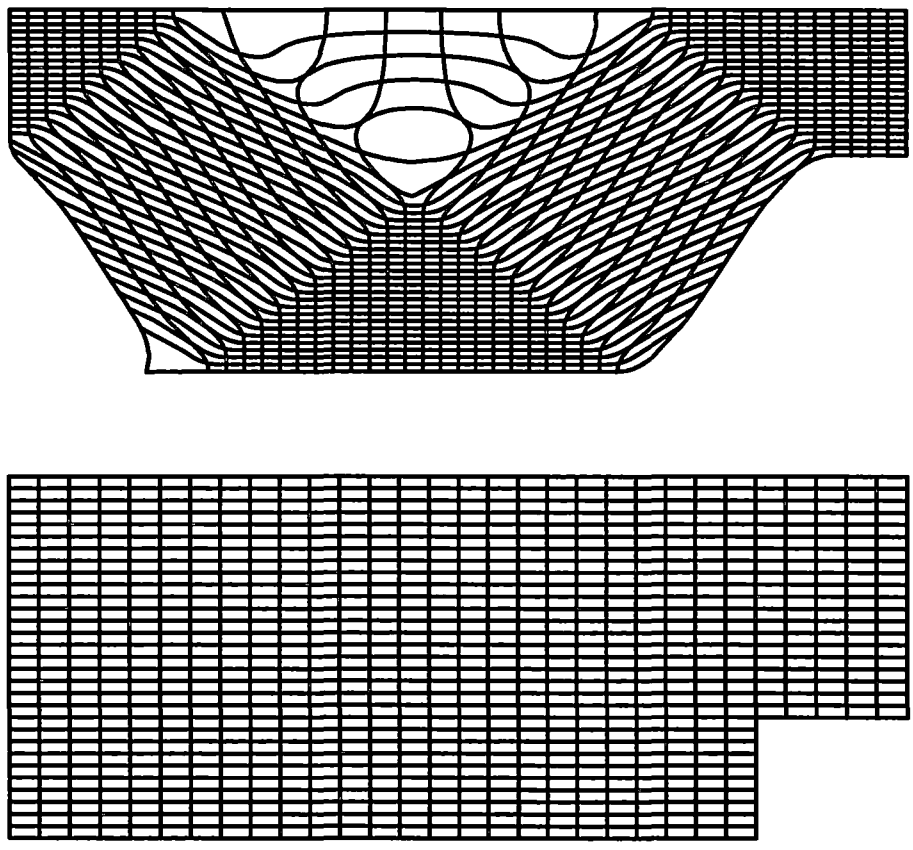

Figure 5.10: When $c = 3.0$ the topography represented by (5.5) is supercritical and maps to a stepped region.

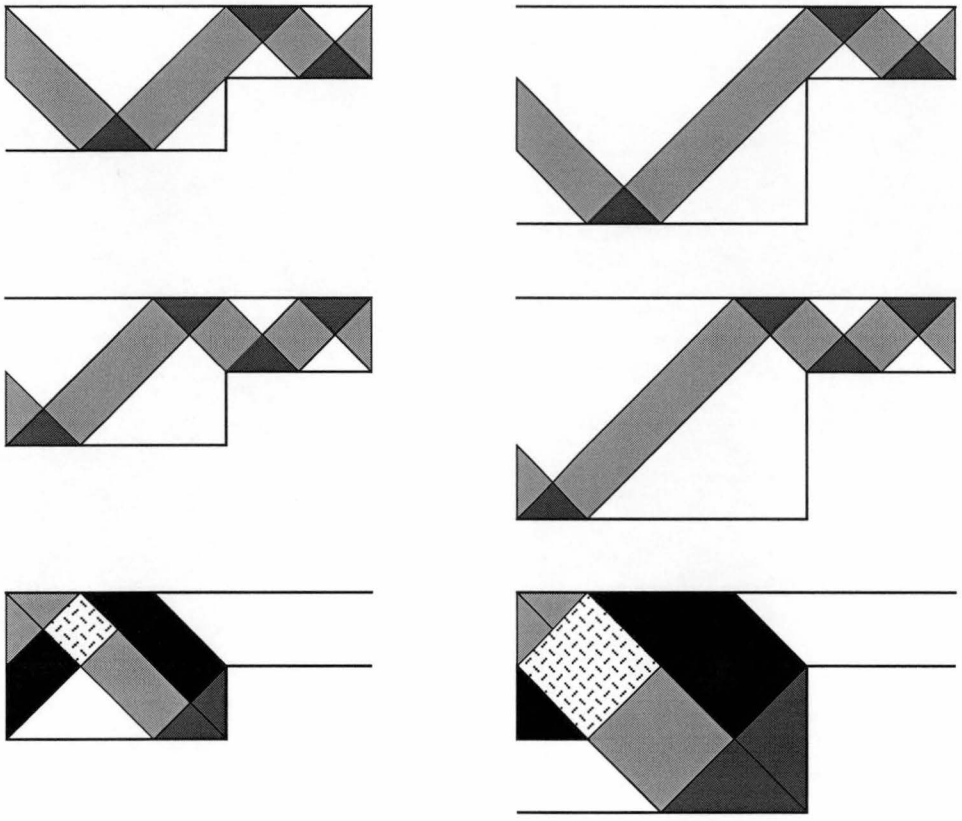

Figure 5.11: Constructing the second stage of the mapping.

Second Stage Mapping

For a purely subcritical region, the second stage of the process is unnecessary, a finite difference scheme can easily be constructed for the resulting flat bottomed region. But for a supercritical region, the dimensions of the resulting stepped topography may still not be ideally suited to the finite differencing, and a second stage transform is required. This second transform maintains the shape of the topography, but alters its relative dimensions.

Figure (5.11) shows how such a transform may be constructed. The shaded regions represent bands of characteristic paths, and how they should be mapped to deepen one side of a stepped topography. Examining this figure it can be seen that the secondary transform is not uniform (again, in the sense of Section

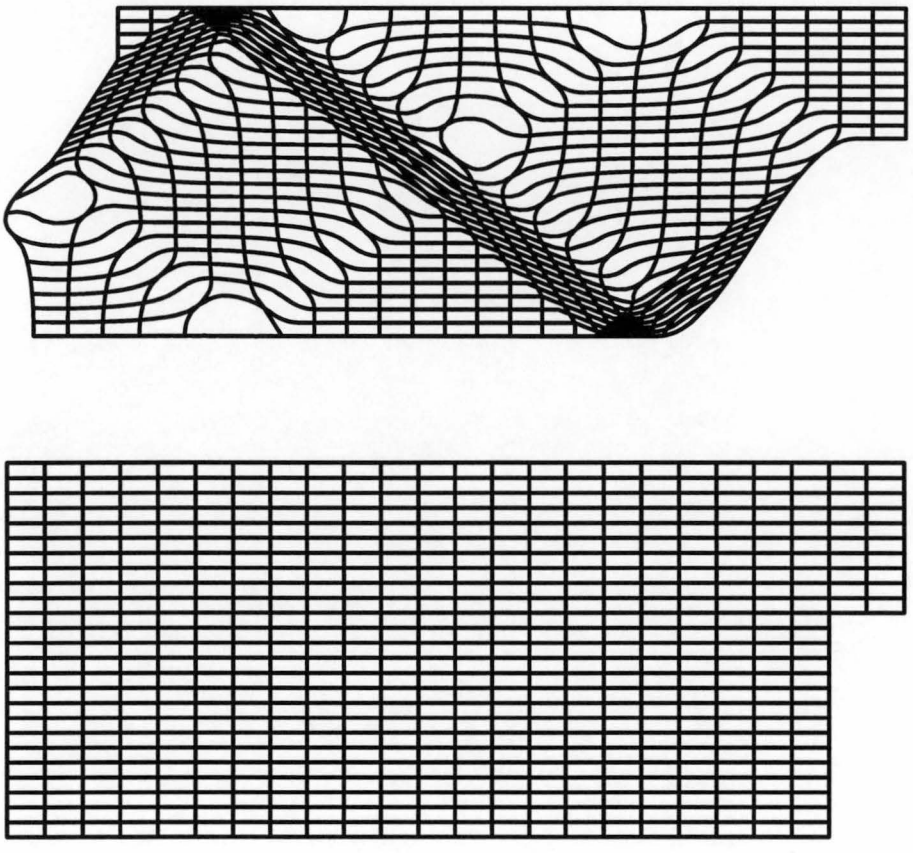

Figure 5.12: The mapping of Figure 5.9 after the second stage transform.

3.3) on its domain. But since this second transform preserves the shape of the topography, a suitable kernel function describing the secondary mapping is easily constructed by hand. The results of applying a transform like that depicted in (5.11) to the topography of Figure 5.9 is shown in Figure 5.12. Obviously, some care must be taken when constructing the secondary transform — redimensioning the topography to grotesque proportions can introduce an unreasonable distribution of nodes in the finite difference grid.

Numerical Comparison

To test the transformation process, a number of test problems were solved using the transform technique described here in conjunction with a standard non–interpolating finite difference scheme. In every case the results were all but identical to those obtained with the interpolating scheme described in the preceding section.

A direct comparison of the results of the two methods is hampered by the markedly different finite difference grids used by each scheme. This is perhaps one of the biggest disadvantages of the transform technique — the inverse image of the finite difference grid is completely irregular, complicating any interpolation scheme used to determine ψ at a point other than a gridpoint. This problem can be avoided by performing the interpolation in the transformed domain.

Nevertheless, the computational advantages of this process are clear. Transforming a complex topography to a simple stepped topography via c–conformal mapping allows the simpler, second order, non–interpolating finite difference scheme to be used while still accurately representing the boundary. Unlike other co–ordinate transformations, c–conformal transformation does not complicate the form of the governing equation, but rather leaves it invariant. Consequently existing solution procedures may be harnessed with a minimum of alteration.

The numerical procedure for determining the c–conformal map is in essence a simple explicit stepping procedure, and hence is both fast and easily implemented. Because the kernel is represented as a linear spline, an explicit representation of the inverse mapping is easily constructed.

The applications of this technique are not just restricted to finite differencing. Preprocessing the topography with a c–conformal map can, for example, greatly simplify an implementation of Craig's technique since the characteristic paths will be easily traced on the resulting stepped topography.

5.3 Summary

This chapter has clearly demonstrated the importance of correctly representing the boundary when solving the internal tide problem by finite difference methods. It has been seen that this can be achieved with an interpolating finite difference scheme, but a simpler method based on c–conformal transformation was also developed. This procedure maps an arbitrary shelf region to a stepped region which can be accurately represented without interpolation. Unlike the transformation of Chuang and Wang[9], since the transformation is c–conformal the form of the governing equation remains invariant, and thus has the advantage that it can be implemented as a preprocessing stage allowing existing solution techniques to be applied largely unaltered.

The following chapter begins a study of a viscous model of internal tide motion.

Chapter 6

A Viscous Model

The analysis of Chapter 4 clearly indicates that any realistic model of internal tide motion on a basin topographies should address viscous effects.

In this chapter, several numerical solution techniques for a viscous model of internal tide motion are devised and compared. Many of these methods do not seek to model the effects of fluid viscosity directly, but instead rely upon a singular perturbation technique described by Craig[15] in conjunction with the theory of the inviscid model described in previous chapters.

Two major approaches are taken, both based on collocation methods:

- an internal collocation technique that fully represents the viscous terms of the model, and
- a number of boundary collocation methods based on the Runge approximation property described in Section 3.5.2; of these only one fully represents the viscous terms of the model, the rest rely on the perturbation technique of Craig.

These methods have been motivated primarily by the tank experiments to be discussed in Chapter 7. Consequently these methods constitute something of an incongruity, in that they are designed for closed basins with an underlying

topography that is shelf–like. It is envisaged that to extend these techniques to shelf regions proper through the incorporation of the appropriate radiation conditions would be relatively straightforward. But due to problems associated with both the collocation method and Craig's perturbation technique, the treatment of more general basin topographies would be more difficult. The motivation for these claims will become apparent as the chapter progresses.

6.1 The Viscous Model

If Coriolis effects are neglected, retaining viscous terms in the model derived in Chapter 2 yields the viscous counterpart of (3.1),

$$\omega^2\nabla^2\psi + N^2\psi_{xx} = -i\omega\nu\nabla^4\psi \tag{6.1}$$

where ν represents (eddy) viscosity and as before ω is the tidal frequency, N the Buoyancy frequency, and x and z are Cartesian co–ordinates oriented in the onshore horizontal and vertical directions respectively. Horizontal and vertical fluid velocities $u(x,z,t)$ and $w(x,z,t)$ are determined from $\psi(x,z)$ by the relations

$$u(x,z,t) = \Re\{-e^{i\omega t}\psi_z(x,z)\} \qquad w(x,z,t) = \Re\{e^{i\omega t}\psi_x(x,z)\} \tag{6.2}$$

where $\Re\{s\}$ denotes the real part of a complex value s.

Performing a standard dimensional analysis for parameter values typical of internal tide motion near the continental shelf shows that those terms which yield the least contribution in the above model are the viscous terms

$$-i\omega\nu\nabla^4\psi = -i\omega\nu(\psi_{xxxx} + 2\psi_{xxzz} + \psi_{zzzz}), \tag{6.3}$$

justifying the inviscid approximation discussed in previous chapters.

For internal tide motion near the continental shelf the intrinsic z scale is of the order of a few hundred metres, and is much shorter than the intrinsic x scale which is typically of the order of hundreds of kilometres. Correspondingly, of

the viscous terms the ψ_{zzzz} term yields by far the largest contribution to the model, and on a shelf the simplest approximation of (6.1) which still retains some viscous terms is

$$-\omega^2\psi_{zz} + (N^2 - \omega^2)\psi_{xx} = -i\omega\nu\psi_{zzzz}. \tag{6.4}$$

For the tank experiments described in Chapter 7 and certain forms of basin, this approximation is less readily justified, but will nevertheless be adhered to for the sake of uniformity and simplicity.

The boundary conditions for this model are effectively the same as those applying to the inviscid model, but must be supplemented by a number of conditions describing viscous effects.

As was the case for the inviscid model, at the upper surface of the fluid co–ordinates are chosen so that $z = 0$ represents the mean position of the free surface, and a "rigid lid" approximation is adopted. As there can be no flow through the bottom boundary $z = h(x)$, the bottom boundary condition takes the form

$$\psi(x, h(x)) = 0, \tag{6.5}$$

while at the upper surface it is again assumed that

$$\psi(x, 0) = B(x, z), \tag{6.6}$$

where $B(x, z)$ represents some appropriate forcing function.

The form of the supplementary conditions required by the viscous model depends upon the intended application. For the tank experiments, the viscosity ν in (6.4) represents kinematic viscosity and it is reasonable to assume that at the lower boundary, the component of velocity tangential to the boundary is zero. At a point where the boundary is not vertical this condition may be represented as

$$\psi_z(x, h(x)) \equiv -u(x, h(x)) = 0, \tag{6.7}$$

since condition (6.5) already implies that the component of fluid velocity normal to the boundary is zero. For oceanographic applications ν represents an eddy viscosity, and to be consistent with the assumptions of an eddy viscosity model (Pond and Pickard[37]) at the lower boundary a linear slip condition (Brink[6]) must be introduced

$$\nu\psi_{zz}(x,h(x)) = r\psi_z(x,h(x)), \tag{6.8}$$

where r represents the coefficient of linear friction. In both cases, at the upper surface it shall be assumed that ψ satisfies a zero stress condition (Pond and Pickard[37]),

$$\psi_{zz}(x,0) \equiv -u_z(x,0) = 0. \tag{6.9}$$

6.2 Collocation Methods

The numerical methods developed in this chapter all rely on some form of collocation. This section gives a brief review of the basic collocation method.

Collocation is a member of the wider class of techniques known as weighted residuals methods(Finlayson[19]), and may take several forms.

Suppose the differential equation

$$L[\psi] = 0 \tag{6.10}$$

defined on a region Ω is to be solved subject to an appropriate set of boundary conditions

$$\mathbf{F}(\psi) = 0 \tag{6.11}$$

imposed on $\partial\Omega$. A weighted residuals method assumes that the true solution ψ may be approximated by a function of the form

$$\psi_T(\mathbf{x}) = b(\mathbf{x}) + \sum_{k=1}^{p} a_k\psi_k(\mathbf{x}) \tag{6.12}$$

where the a_k are to be determined. This function is called the *trial solution*, and the functions $\{\psi_k\}$ are called the *trial functions*. The function $b(\mathbf{x})$ is introduced to aid the trial solution in satisfying the boundary conditions (6.11).

From the trial solution the residuals

$$R_L(\mathbf{x}) = L(\psi_T(\mathbf{x})) \qquad \mathbf{x} \in \Omega \tag{6.13}$$

$$R_B(\mathbf{x}) = L(\psi_T(\mathbf{x})) \qquad \mathbf{x} \in \partial\Omega \tag{6.14}$$

are defined. The undetermined coefficients $\{a_k\}$ in the trial solution are calculated by requiring that these residuals be zero at a number of points, called the *collocation points*, in their respective domains.

It is the choice of $b(\mathbf{x})$ and the trial functions that determines the form of collocation used. There are three cases depending upon the structure of the trial solution.

i). If, for all choices of the a_k, the residual R_L is identically zero on Ω, then the trial solution satisfies (6.10) automatically and the collocation method proceeds by requiring $R_B = 0$ at p collocation points selected from the boundary $\partial\Omega$, resulting in a system of algebraic equations for the unknown coefficients $\{a_k\}$. This procedure is called *boundary collocation*. One example of this has already been given in Section 3.2. Boundary collocation will underlies many of the methods derived later in the chapter.

ii). If, for all choices of the a_k, the residual R_B is identically zero on $\partial\Omega$, then the trial solution satisfies the boundary conditions (6.11) and the a_k are determined by requiring $R_L = 0$ at p collocation points selected from Ω. This procedure is called *internal* or *interior collocation*, and forms the basis of the numerical method developed in the next section.

iii). If neither R_L nor R_B is identically zero on their respective domain then the trial solution satisfies neither (6.10) or (6.11) automatically. In this case the p collocation points must be chosen from both Ω and $\partial\Omega$, with the

condition on the a_k at each point deriving from the appropriate residual in the obvious manner. This is called a *mixed* or *tau method*(Lanczos[26]), and will not be discussed further here.

The success of the collocation method relies strongly on the choice of the trial functions. This point is discussed in some detail by Gottleib and Orszag[22], who provide a number of illuminating examples.

In the most general case, the choice of the collocation points is to a large extent arbitrary. However, Finlayson[19] strongly recommends the use of orthogonal collocation, in which the trial functions are selected from a set of orthogonal functions, and the collocation points are chosen as the zeros of the first neglected element of this set. This has the added advantage that the collocation procedure may often be accelerated by the application of a fast orthogonal transform, such as the fast Fourier or fast Chebyshev transforms. This point is discussed in more detail by Canuto *et. al.*[7].

6.3 The Viscous Model — Interior Collocation

The first method developed in this chapter is a straightforward application of interior collocation methods to the viscous internal tide problem. This method is one of only two considered in the chapter that seek to fully represent the viscous terms of the model. Although this is one of the simplest and perhaps the most general of all the techniques to be discussed, it is almost certainly the most computationally intensive.

The method is directed primarily at modelling the tank experiment described in Chapter 7 and hence it is assumed that the topography is similar to that depicted in Figure 7.1 — consisting of a shelf like component represented as $z = h(x)$ but bounded at each of it's extremities by a vertical section.

For interior collocation the trial solution must be chosen so as to satisfy the imposed boundary conditions. For the tank experiment the boundary conditions

are assumed to be of the form

$$\psi(x,z) = B(x,z) \qquad (x,z) \in \partial\Omega \tag{6.15}$$

$$\psi_{zz}(x,0) = 0 \qquad 0 \le x \le l \tag{6.16}$$

$$\psi_z(x,h(x)) = 0 \qquad 0 \le x \le l, \tag{6.17}$$

where B represents a boundary forcing and l the length of the tank.

The trial solution is based on a Fourier Sine expansion and the transformation

$$r = x \qquad s = z/h(x), \tag{6.18}$$

and is chosen as

$$\psi_T(x,z) = B(x,z) + \sum_{m=1}^{N_m}\sum_{n=1}^{N_n} a_{mn}\psi_{mn}(x,z), \tag{6.19}$$

where the trial functions $\psi_{mn}(x,z)$ are defined by

$$\psi_{mn}(x,z) = \sin\frac{m\pi x}{l}\left(p_n(z/h(x)) + \sin\frac{n\pi z}{h(x)}\right) \tag{6.20}$$

$$p_n(t) = (-1)^n n\pi(t^3 - t)/2. \tag{6.21}$$

The polynomial $p_n(z/h(x))$ ensures that the trial functions satisfy the boundary condition (6.17). Alternatively, the trial functions could have been based on some family of orthogonal polynomials, but (6.20) seems the more natural choice given that $\sin\lambda x \sin\lambda z$ is a solution of the inviscid model.

Defining

$$L[f] = (N^2 - \omega^2)f_{xx} - \omega^2 f_{zz} + i\nu\omega f_{zzzz}, \tag{6.22}$$

the residual R_L is given by

$$R_L(x,z) = L[\psi_T]. \tag{6.23}$$

The coefficients a_{mn} are calculated by requiring that

$$R_L(x_i,z_i) = 0 \tag{6.24}$$

at the collocation points (x_i, z_i) defined by the zeros of

$$\sin(N_m + 1)\pi x/l \sin(N_n + 1)\pi z/h(x). \tag{6.25}$$

A *Mathematica* script implementing the collocation procedure is given in Appendix B. This implementation is greatly simplified by *Mathematica*'s symbolic algebra capabilities, since it is possible to automatically generate the residual $R_L(x, z)$ given (6.19) and (6.22). For constant buoyancy frequency N, the efficiency of this algorithm could be improved by harnessing the orthogonality properties of the trial functions. However, the naive implementation presented in Appendix B has the advantage that it remains valid for both constant and non–constant N.

Two simple test cases were used to compare this procedure with the other methods to be derived later in the chapter.

For the first test case the lower topography was taken as

$$h(x) = -0.6 - 0.1/\pi \arctan 8(x - 1) \tag{6.26}$$

on $0 \leq x \leq 2$, with

$$B(x, z) = \sin \pi x/2(1 - z/h(x)). \tag{6.27}$$

It was necessary to choose so simple a topography to allow a simultaneous comparison for all the methods derived in this chapter. In the following chapter this technique is applied to a more demanding problem.

The solution obtained with $N_m = 40$, $N_n = 20$, $\omega = 0.66$, $N = 1.145$ and $\nu = 2.0 \times 10^{-5}$ is depicted in Figure 6.1. These parameter values are realistic for the tank experiment, except for the value of ν which has been inflated by an order of magnitude.

The success of the collocation procedure may be gauged by examining

$$R_L(x, z) \equiv L[\psi_{N_m, N_n}]$$

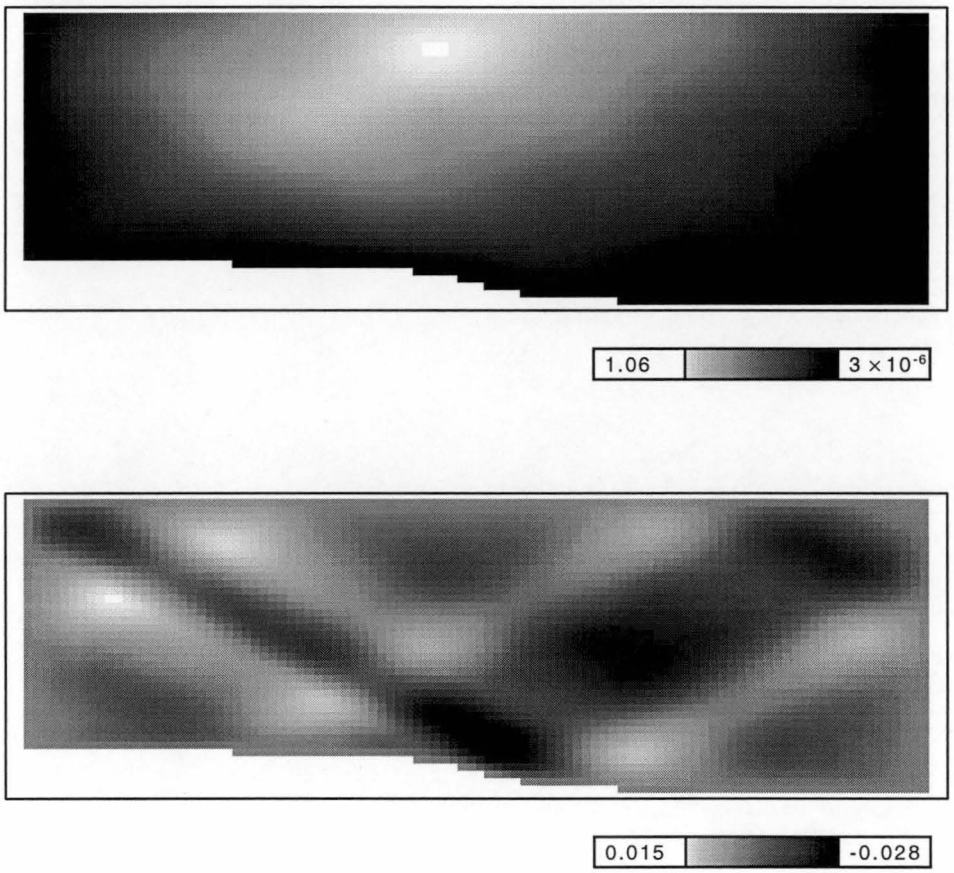

Figure 6.1: Solution of the first test case obtained by interior collocation, with $N_m = 40$, $N_n = 20$, $\omega = 0.66$, $N = 1.145$ and $\nu = 2.0 \times 10^{-5}$. Top — $\Re\{\psi\}$, bottom — $\Im\{\psi\}$.

in relation to $L[\psi_{N_m+1,N_n+1}]$. If the collocation process is converging then it can be expected that $R_L(x,z)$ will be small in relation to $L[\psi_{N_m+1,N_n+1}]$, and indeed this is the case for the solution depicted in Figure 6.1.

For the second test case the lower topography was taken as the semi–circle defined by

$$h(x) = \sqrt{1-(x-1)^2} \tag{6.28}$$

on $0 \leq x \leq 2$, with

$$B(x,z) = \cos(\pi(x-1)^2/2)\left(\frac{3z}{2h(x)} - \frac{z^3}{2h^3(x)} + 1\right). \tag{6.29}$$

With this choice of forcing function the solution of the corresponding inviscid problem can be determined by c–conformal mapping (see Section 6.6.1), providing a useful comparison.

The viscous solution obtained for $N_m = 30$, $N_n = 20$, $\omega = 1$, $N = \sqrt{2}$ and $\nu = 10^{-5}$ is depicted in Figure 6.2.

In this case it is found that $R_L(x,z)$ is much larger than $L[\psi_{N_m+1,N_n+1}]$ in the corners of the region, indicating a breakdown in the solution procedure. This is to be expected given the nature of the trial solution. The trial solution (6.19) is constructed from a Fourier Sine series by performing an implicit transformation of the form (6.18) from the test–region to a rectangle. For the semi–circle this transformation is not well defined at the corner points.

In general it can be expected that the collocation procedure described above will fail if $h(x) = 0$ at some point, due to the failure of the transformation (6.18). Presumably this problem could be overcome by adopting a suitable generalization of (6.18) as a basis for the trial functions but this avenue has not been pursued.

The advantage of the interior collocation method is its genericity. The same technique applies to all regions, characteristically convex or otherwise, and is equally applicable to constant and non–constant buoyancy frequencies. The primary disadvantage of this method is the computational effort required. The collocation procedure results in a matrix problem for $N_m N_n$ unknowns, and thus is prohibitive for large expansions.

In the following sections a variety of solution techniques based on the theory of Section 3.5.2 are developed. These techniques are less general than the internal collocation method described in this section, but are considerably more efficient. Several of these methods rely on a perturbation technique due to Craig[16].

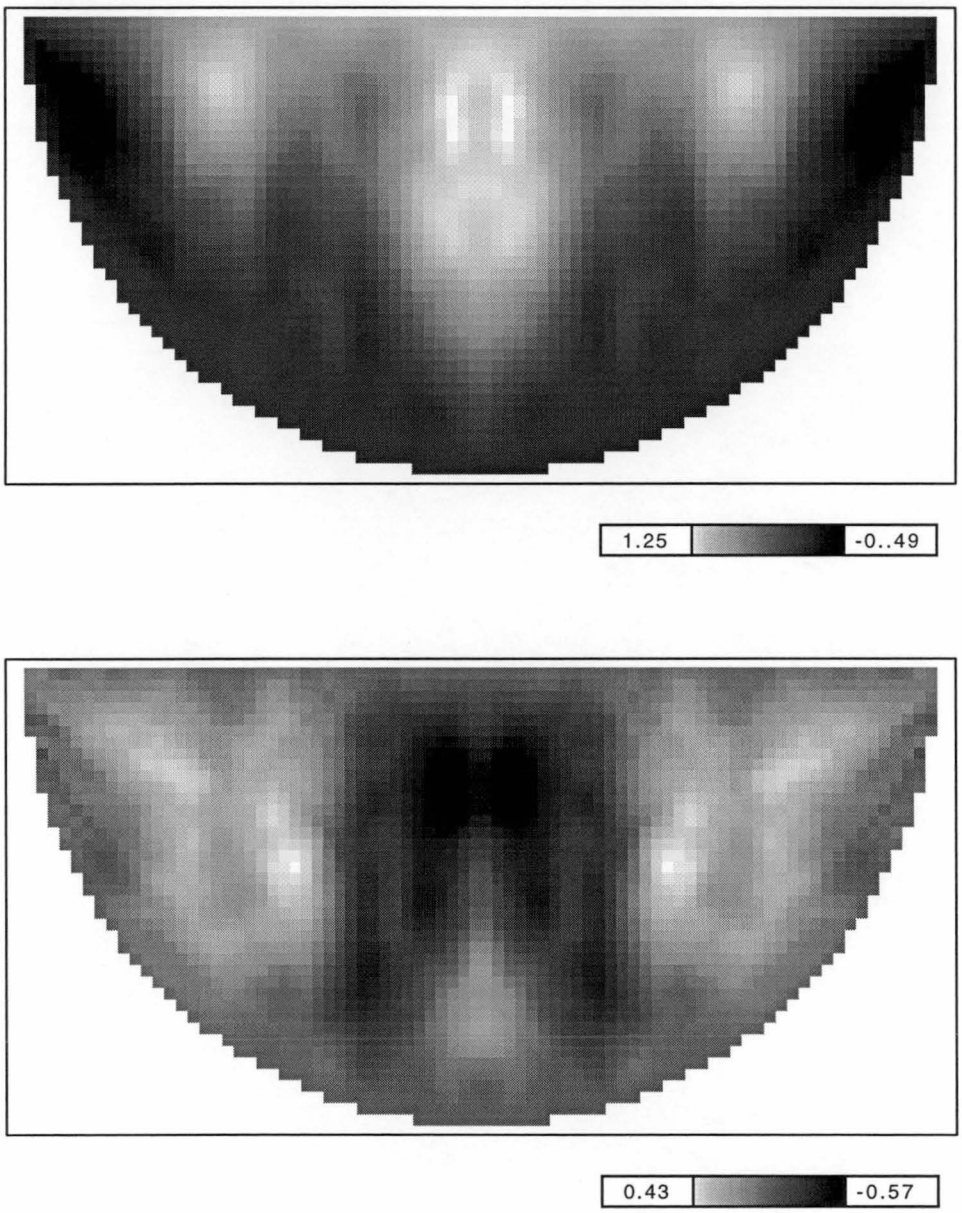

Figure 6.2: Solution of the semi–circular test case obtained by interior collocation, with $N_m = 30$, $N_n = 20$, $\omega = 1$, $N = 1.142$ and $\nu = 10^{-5}$. Top — $\Re\{\psi\}$, bottom — $\Im\{\psi\}$.

6.4 Craig's Perturbation Method

In re–introducing viscous terms to the model, much of the elegance and simplicity of the inviscid form (3.1) has been lost. Craig[16] proposes a two stage procedure based on the work of Brink[6] and Clarke and Brink[10] which allows the viscous model to be solved in terms of the much simpler inviscid model. This has two primary advantages:

- it allows the wide body of theory developed for the inviscid model to be applied to the viscous case, and
- it obviates the need for a numerical solution procedure to resolve a viscous boundary layer.

Craig[16] derives his method under the assumption of a flat bottom topography, and demonstrates validity of this technique for a channel of constant depth. In this section Craig's method is first outlined and then extended to encompass sloping topographies.

Craig's procedure consists of two stages based on the the philosophy of Clarke and Brink[10]. In the first stage the viscous model (6.4) is approximated by its inviscid counterpart (3.1) with the two viscous boundary conditions imposed at the lower boundary replaced by a single condition representing the effects of boundary friction. This first stage solution approximates the viscous solution but does not account for viscous effects in the body of the fluid. The second stage re–introduces internal friction effects to the model by treating them as perturbations of the first stage solution.

First Stage

The form of the new condition imposed at the lower boundary in the first stage of the process is dependent upon the viscous boundary conditions imposed there. Craig[16] derives the new condition corresponding to a linear slip condition (6.7)

imposed on the lower boundary $z = h$ of a flat bottomed ocean. Here, the new condition corresponding to the zero slip condition more appropriate to modelling the tank experiments is derived, again assuming a flat bottomed ocean. In the next section this condition will be extended to better deal with sloping topographies. The new condition is derived as follows.

Returning to a dimensional analysis of the viscous model, in the body of the fluid, the primary balance in (6.4) is between the two terms on the left hand side of the equation, and the inviscid model is a good approximation to (6.4). But, as discussed in detail by Craig[16], in the bottom boundary layer the primary balance in this equation is between the ψ_{zz} and ψ_{zzzz} terms. In the boundary layer, (6.4) may be approximated by

$$-\omega^2\psi_{zz} = -i\omega\nu\psi_{zzzz}, \tag{6.30}$$

and ψ can be expected to behave approximately as

$$\psi(x,z) = e^{\lambda z} \tag{6.31}$$

where

$$\lambda = -\sqrt{\frac{i\omega}{\nu}}. \tag{6.32}$$

Following Clarke and Brink[10], Craig assumes that the boundary layer is small in comparison with the total fluid depth and represents ψ as a sum of two components

$$\psi = Ae^{\lambda(z-h)} + \psi^{(0)}. \tag{6.33}$$

The first term represents the behaviour of ψ inside the boundary layer. Outside the boundary layer this term is small and ψ behaves as $\psi^{(0)}$. Correspondingly, $\psi^{(0)}$ may be assumed to satisfy (3.1).

The form of the new boundary condition follows naturally. Condition (6.5) requires that $A = -\psi$ on $z = h$. Substituting (6.33) into the zero slip condition

(6.7) then yields the new condition for $\psi^{(0)}$,

$$\psi_z^{(0)} - \lambda\psi^{(0)} = 0. \tag{6.34}$$

This new condition replaces both (6.7) and (6.5) at the lower boundary.

At the upper surface there is a zero stress condition and boundary layer effects are negligible. Thus $\psi^{(0)}$ may be determined by solving (3.1) subject to (6.6) and the new boundary condition (6.34).

Craig[16] has demonstrated the validity of this approximation for a flat bottomed ocean. Comparing solutions found by the above method to exact solutions of the full viscous model (6.4), Craig found that even for quite large values of the viscosity ν, the solutions were in excellent agreement.

Similarly, if Craig's method is applied to a rectangular basin, it is found that the first stage solution $\psi^{(0)}$ reproduces the amplitude and phase of the exact solution of the viscous model to a high degree of accuracy, even near resonance.

Second Stage

The second stage of Craig's method further improves the approximation of the first stage by re–incorporating viscous effects in the body of the fluid into the model. These are treated as a perturbation of the first stage solution $\psi^{(0)}$.

In the second stage Craig represents the stream function as

$$\psi = \psi^{(0)} + \psi^{(1)}, \tag{6.35}$$

where $\psi^{(0)}$ is the first stage solution and the viscous correction $\psi^{(1)}$ satisfies

$$-\omega^2\psi_{zz}^{(1)} + (N^2 - \omega^2)\psi_{xx}^{(1)} = -i\omega\nu\psi_{zzzz}^{(0)}. \tag{6.36}$$

and the boundary conditions (6.34) and (6.6). This can be viewed as a perturbation process in ν where $\psi^{(0)}$ represents the zero–th order solution and $\psi^{(1)}$ the first order correction, or alternately, as the first correction in an iterative procedure based on (6.4).

For a flat bottomed ocean, Craig[16] has shown that the solution obtained from the second stage procedure and the exact solution of (6.4) are in excellent agreement.

However, changing to characteristic co–ordinates it is seen that for any given $\psi^{(0)}$, a particular solution $\psi_p^{(1)}$ of (6.36) is given by

$$\psi_p^{(1)} = -\frac{i\omega\nu}{4(N^2-\omega^2)} \iint \psi_{zzzz}^{(0)}\, d\eta\, d\xi. \tag{6.37}$$

If $\psi^{(0)}$ is represented as a Fourier series,

$$\psi^{(0)} = \sum_{j,k}^{\infty} a_{jk} e^{i(j\lambda x + k\mu z)} \tag{6.38}$$

then

$$\psi_p^{(1)} = \sum_{j,k}^{\infty} \gamma_{jk} a_{jk} e^{i(j\lambda x + k\mu z)} \tag{6.39}$$

where

$$\gamma_{jk} = \begin{cases} \frac{i\omega\nu k^4\mu^4}{(N^2-\omega^2)(j^2\lambda^2-k^2c^2\mu^2)} & \text{if } j\lambda \neq \pm ck\mu \neq 0 \\ i\nu(x-z/c)k^2\mu^2/(4\omega) & \text{if } j\lambda = ck\mu \neq 0 \\ -i\nu(x+z/c)k^2\mu^2/(4\omega) & \text{if } j\lambda = -ck\mu \neq 0 \\ 0 & \text{if } k = 0. \end{cases} \tag{6.40}$$

The factor γ_{jk} behaves approximately as k^2, accentuating higher order harmonics of z in the Fourier expansion. This in turn suggests that in general the perturbation (6.36) may be unstable. This argument is only suggestive as the stability of the procedure depends largely on the boundary conditions, which have been ignored in this analysis.

The obvious shortcoming of Craig's approach is the assumption of a flat bottomed ocean. This will be remedied in the following section.

6.4.1 Sloping Topography

In deriving the new boundary condition (6.34), Craig's method assumes that the topography is horizontal. This is obviously too restrictive. Although it is possible to calculate the new boundary condition assuming an arbitrary topography, the form of the condition becomes exceedingly complex. In this section the middle ground is taken: it is assumed that the bounding topography $z = h(x)$ is sloping but locally flat, that is, that terms involving $h''(x)$, $h'''(x)$, $h''''(x)$ ... may be neglected in comparison with terms involving $h(x)$ or $h'(x)$.

The derivation follows that of the previous section, except that it is conducted in the co–ordinate frame defined by

$$r(x,z) = \frac{h'(x)z + x}{\sqrt{1+h'(x)^2}} \qquad s(x,z) = \frac{z - h'(x)x}{\sqrt{1+h'(x)^2}}. \tag{6.41}$$

This effectively constitutes a local rotation of co–ordinate frame so that at any point on the boundary r is tangential and s normal to the boundary.

In the boundary layer it is assumed that ψ displays greatest variation in a direction normal to the boundary, varying much more slowly in the tangential direction. Thus in the boundary layer, derivatives with respect to r may be neglected in comparison with other terms. Expressing (6.4) in terms of rs co–ordinates and neglecting derivatives with respect to r yields

$$((N^2-\omega^2)h'(x)^2 - \omega^2)\psi_{ss} - \frac{i\nu\omega}{1+h'(x)^2}\psi_{ssss} = 0 \tag{6.42}$$

This is the direct counterpart to Equation (6.30). In the boundary layer, ψ can expected to behave as

$$\psi(r,s) = e^{\lambda s}, \tag{6.43}$$

where (in terms of x)

$$\lambda = -\sqrt{\frac{i(\omega^2 + (2\omega^2 - N^2)h'(x)^2 + (\omega^2 - N^2)h'(x)^4}{\nu\omega}}. \tag{6.44}$$

Again, the stream function ψ may be represented as a sum of two components

$$\psi = Ae^{\lambda(s-h(r))} + \psi^{(0)}, \tag{6.45}$$

where the first term represents the behaviour of ψ inside the boundary layer, and the second represents the behaviour of ψ external to the boundary layer and is again governed by the inviscid model (3.1).

Condition (6.5) requires that $A = -\psi$ on $s = h(r)$, and substituting (6.45) into the zero slip condition (6.7) yields the new condition on $\psi^{(0)}$

$$\psi_z^{(0)} - \frac{\lambda}{\sqrt{1+h'(x)^2}}\psi^{(0)} = 0,$$

or equivalently

$$\psi_z^{(0)} - \lambda'\psi^{(0)} = 0, \tag{6.46}$$

where

$$\lambda' = -\sqrt{\frac{i(\omega^2 + (2\omega^2 - N^2)h'(x)^2 + (\omega^2 - N^2)h'(x)^4}{\nu\omega(1+h'(x)^2)}}. \tag{6.47}$$

Again $\psi^{(0)}$ may be determined by solving (3.1) subject to (6.6) and the new boundary condition (6.46).

The second stage procedure remains unaltered.

A number of numerical methods that harness Craig's procedures are developed in the following sections.

6.5 Finite Differences

Craig's perturbation approach, described in the previous section, allows the viscous model (6.4) to be solved in terms of its inviscid counterpart (3.1). Thus a solution method for the inviscid model is required, and the interpolating finite difference scheme developed in Chapter 5 would appear a natural choice. But in spite of its simplicity, implementing Craig's procedure in terms of finite differences proves to be a non–trivial exercise.

The difficulty stems from the fact that the first stage solution is still a solution of the inviscid model. Thus it is necessary to follow the principles outlined in Chapter 5 and require that the finite difference scheme accurately represent the shape of the boundary.

Implementing an interpolatory finite difference scheme for Craig's perturbation method proves to be far more difficult than for the standard inviscid model. Consider again Figure 5.2 from Chapter 5. As was discussed in that chapter, correctly representing the boundary requires the introduction of the two new grid points (circled) at E' and D'. For the inviscid model, constructing the finite difference scheme is simple because the boundary condition is $\Psi = 0$ on the lower boundary — there is nothing to be calculated. But Craig's method requires that Ψ and its derivatives be known at E' and D'. This requires further interpolation, greatly complicating the implementation of the scheme.

Yet neither are the transform techniques discussed in Chapter 5 suited to basin topographies. The transformation (5.9) of Chuang and Wang[9] is open to the same problems encountered in Section 6.3, and, as discussed in Section 3.5.3, for a given basin there may not exist an appropriate c–conformal map.

Although these problems are not insurmountable, finite difference methods will not be considered further in this chapter.

6.6 Runge Approximation Methods

In Section 3.5 it was discussed how c–analytic continuation and the Runge approximation property can form the basis for a solution technique for the inviscid model (3.1). Here, a number of viscous methods based on this technique and Craig's perturbation method are devised. Initially, only characteristically convex regions are considered, the treatment of more complex regions being left to later in the section.

6.6.1 The Inviscid Case

To illustrate both the basic technique and the problems arising from a purely inviscid formulation, consider the semi–circular problem discussed in Section 6.3.

Ignoring the viscous boundary conditions, the general solution of the inviscid model for this problem is easily generated through c–conformal mapping. To simplify the analysis, the basin is translated to the left, so that

$$h(x) = \sqrt{1 - x^2}, \tag{6.48}$$

$$B(x, z) = \cos(\pi x^2/2) \left(\frac{3z}{2h(x)} - \frac{z^3}{2h^3(x)} + 1 \right). \tag{6.49}$$

Noting that the parameters chosen in Section 6.3 imply $c = 1$, the semi–circle (6.48) can be mapped to the rectangle with vertices

$$\{(2, 0), (-2, 0), (-2, -2), (2, -2)\}$$

by the c–conformal map

$$r(x, z) = f(x + z) + f(x - z) \tag{6.50}$$

$$s(x, z) = f(x + z) - f(x - z) \tag{6.51}$$

$$f(t) = t^2 \operatorname{sgn} t. \tag{6.52}$$

On the rectangle, the transformed boundary conditions require that on the surface $s = 0$,

$$\psi(r, 0) = \cos(\pi r/4),$$

with $\psi \equiv 0$ on the remainder of the boundary.

Thus the solution of the inviscid form of the problem is given by

$$\psi(x, z) = \cos(\pi r(x, z)/4) \cos(\pi s(x, z)/4) + \sum_{n=0}^{\infty} c_n \sin(n\pi r(x, z)/2) \sin(n\pi s(x, z)/2), \tag{6.53}$$

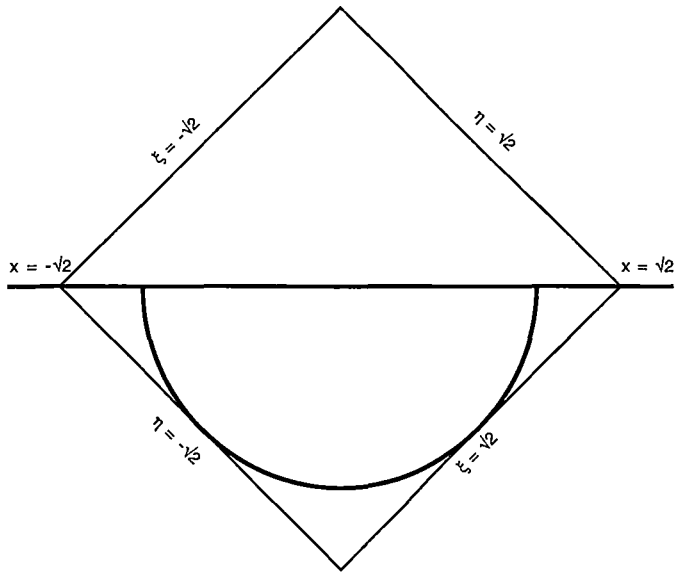

Figure 6.3: Continuation region for the semi–circle

with the first term arising from the forcing (6.49), while the terms in the sum represent the natural modes of the semi–circle (6.48).

This solution can be reproduced from the theory of c–analytic continuation developed in Sections 3.5.1 and 3.5.2 as follows.

As the semicircle is characteristically convex, then, as discussed in Section 3.5.1, the definition of a c–form ψ defined on the semi–circle can be extended into the square region depicted in Figure 6.3 by c–analytic continuation. Consider the c–analytic continuation $\tilde{\psi}$ of ψ, constructed so that

$$\tilde{\psi}(x,0) = \begin{cases} B(x,0) & \text{if } |x| \leq 1 \\ 0 & \text{if } |x| > 1, \end{cases} \tag{6.54}$$

where $B(x,z)$ is the forcing function (6.49). Decompose $\tilde{\psi}$ into a sum of two components,

$$\tilde{\psi} = \psi_0 + \psi_1, \tag{6.55}$$

where ψ_0 is any solution of (3.1) which satisfies (6.54) and ψ_1 is a solution of

(3.1) which satisfies $\psi = 0$ on $z = 0$.

Since ψ_0 need only satisfy the boundary condition (6.54) at the surface, a simple choice of ψ_0 is given by

$$\psi_0(x,z) = \begin{cases} B(x - z/c, 0) & \text{if } |x - z/c| \leq 1 \\ 0 & \text{if } |x - z/c| > 1 \end{cases} \tag{6.56}$$

Note that this is a function of $x - z/c$ alone and is therefore automatically a c–form.

The second component ψ_1 may be represented as a c–form of the form

$$\psi_1(x,z) = f(x + z/c) - f(x - z/c). \tag{6.57}$$

Then, as explained in Section 3.5.2, by expanding f in the form

$$\sum_{n=0}^{\infty} a_n \phi_n(t), \tag{6.58}$$

the second component ψ_1 may be expressed as

$$\psi_1(x,z) = \sum_{n=0}^{\infty} a_n [\phi_n(x - z/c) - \phi_n(x + z/c)], \tag{6.59}$$

where $\{\phi_n\}$ is a set of functions complete in some suitable function space V defined on the interval $[-\sqrt{2}, \sqrt{2}]$.

For the semi–circular example, choose the ϕ_n as

$$\phi_n(t) = \cos \frac{n\pi(t - \sqrt{2})}{2\sqrt{2}} \tag{6.60}$$

which are complete in $L^2[-\sqrt{2}, \sqrt{2}]$, the space of square integrable functions defined on $[-\sqrt{2}, \sqrt{2}]$. The coefficients a_n in (6.59) are then chosen so that (6.55) satisfies the inviscid boundary condition

$$\psi(x, h(x)) = 0 \tag{6.61}$$

on the lower boundary.

Boundary Collocation

This representation of $\tilde{\psi}$ leads naturally to a boundary collocation procedure for the numerical determination of the a_n. The trial solution for the collocation process is chosen as the truncation of (6.55):

$$\psi_T(x,z) = \psi_0(x,z) + \sum_{n=1}^{N_a} a_n[\phi_n(x - z/c) - \phi_n(x + z/c)], \tag{6.62}$$

where the b_n and $\{\phi_n\}$ are defined by (6.56) and (6.60) respectively.

Note that the $n = 0$ term has been dropped from the expansion of ψ_1. This is necessary because when ψ_1 is represented as a c–form (6.57) the function f is only determined up to a constant, and thus to obtain a unique solution, the constant term represented by ϕ_0 must be dropped from the expansion. It is for this reason that the ϕ_n were chosen as the terms of a cosine series rather than a sine series. In a sine series the constant term is not explicit and is more difficult to remove.

The a_n are then determined by requiring that ψ_T satisfy (6.61) at N_a collocation points, chosen from those zeros of

$$\phi_{N_a+1}(x - z/c) - \phi_{N_a+1}(x + z/c) \tag{6.63}$$

which lie on the boundary $z = h(x)$. An example *Mathematica* script implementing this procedure is contained in Appendix C.

This procedure was performed for a number of choices of N_a. Although in each case the process appeared to converge to a solution of the form (6.53), the process was found to be extremely unstable, with small variations in the number and position of the collocation points resulting in vastly different solutions. This is to be expected, for it is the numerical error introduced through truncating (6.55) that governs to which of the solutions (6.53) that the numerical procedure converges.

6.6.2 Choice of Basis

Although the algorithm generalizes naturally to any characteristically convex region, the choice of an appropriate set of ϕ_n is not always clear.

For example, let $c = 1$ and consider the solution

$$\psi(x, z) = z + 1 \tag{6.64}$$

$$= (x - z) + (x + z) + 1 \tag{6.65}$$

defined on the infinite channel bounded above by $z = 0$ and below by $z = -1$. As discussed in Section 4.3.1, this solution can be mapped to the basin defined by (4.42) with the c–conformal map defined by the phase function (4.44). This yields the solution

$$\psi(x, z) = f(x - z) + f(x + z) + 1, \tag{6.66}$$

where

$$f(t) = \left(\ln \frac{t}{1-t}\right) \Big/ \left(\ln \frac{\alpha+1}{\alpha-1}\right) \tag{6.67}$$

which satisfies the boundary conditions

$$\psi(x, 0) = 1 \tag{6.68}$$

$$\psi(x, h(x)) = 0 \tag{6.69}$$

on the basin defined by (4.42).

If this solution is to be reproduced with the procedure described above, the $\phi_n(t)$ must be chosen so that $f(t)$ can be represented in the form (6.58). But for this example $f(t)$ does not lie in L^2 (the space of square integrable functions) and therefore cannot be said to have a convergent Fourier expansion. Thus an appropriate set of $\phi_n(t)$ for this problem is not obvious.

This problem arises from the fact that although (6.64) is itself bounded on the channel, when represented as a c–form (6.65) its components are not.

In spite of these difficulties, the advantages of the method are clear. Of all the solution techniques for the inviscid model examined to date, this is by far the simplest to implement and requires the least computational effort. Several other methods based on the expansion (6.55) were examined, a Galerkin technique and a method based on Gram Schmidt Orthogonalization, but the few observed computational advantages were at the expense of the simplicity of the implementation. In the following sections it is demonstrated how Craig's perturbation technique can be used to extend this method to the viscous model.

6.6.3 Craig's Perturbation Method

The numerical procedure developed in the preceding section for the inviscid model provides a natural vehicle for the implementation of Craig's perturbation method, described in Section 6.4.

First Stage Solution

The first stage of Craig's method is easily implemented in terms of the numerical procedure describe in the previous section. All that is required is that the boundary condition (6.61) of the inviscid model be replaced with either (6.34) or (6.46) as appropriate.

Figure 6.4 shows the results of the method for the semi–circular test case using (6.46) with $N_a = 60$, $\omega = 1$, $N = 1.142$ and $\nu = 10^{-5}$. As might be expected, this solution bears strong resemblance to the inviscid solution (6.53) with $c_n = 0$. Unlike the inviscid implementation, the numerical procedure was found to be stable, producing similar solutions for a variety of choices of N_a. As before, the effectiveness of the collocation procedure can once more be gauged by examining the total residual in comparison to that generated by the first neglected term of the trial solution. In all cases the residual was found to be within acceptable bounds.

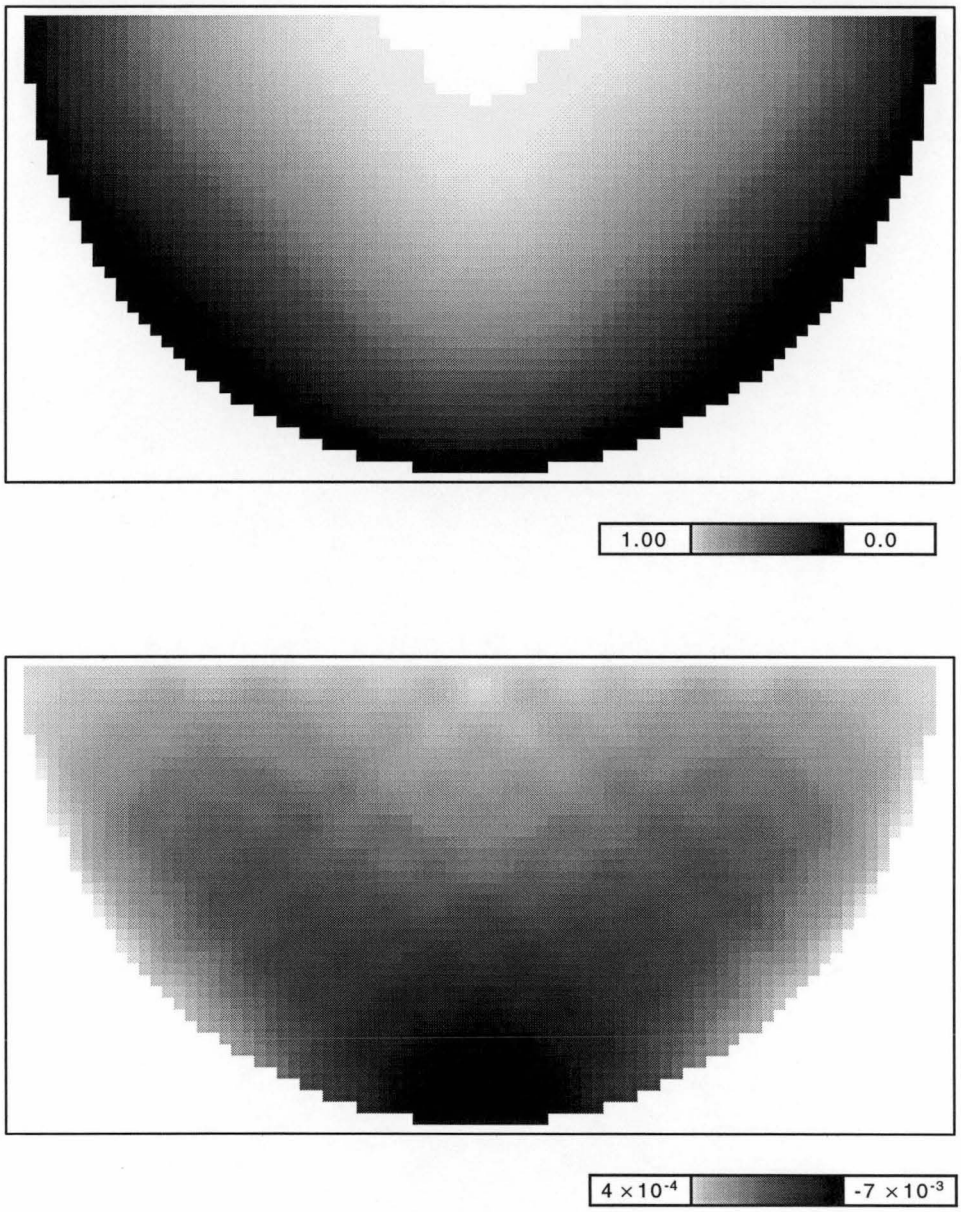

Figure 6.4: Solution of the semi–circular test case obtained by boundary collocation methods, with $N_a = 40$, $\omega = 1$, $N = 1.142$ and $\nu = 10^{-5}$. Top — $\Re\{\psi\}$, bottom — $\Im\{\psi\}$.

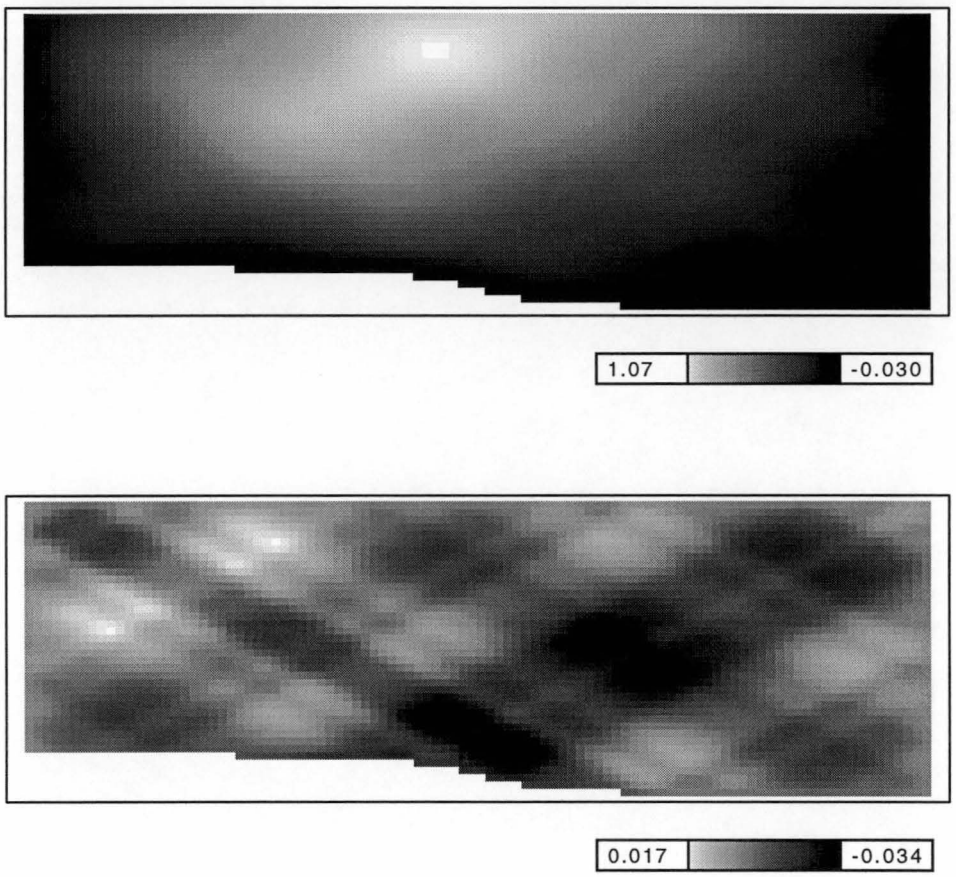

Figure 6.5: Solution of the first test case obtained by boundary collocation methods and Craig's perturbation technique, using the boundary condition (6.46), with $N_a = 60$, $\omega = 0.66$, $N = 1.145$ and $\nu = 2.0 \times 10^{-5}$. Top — $\Re\{\psi\}$, bottom — $\Im\{\psi\}$.

However, when the forcing function $B(x,z)$ was chosen so that

$$B(x,0) = \sin \pi x^2, \tag{6.70}$$

the procedure was once more found to be unstable, yielding an unacceptably large residual for all choices of collocation points tried. Comparing with the inviscid solution (6.53), it can be seen that this choice of $B(x,z)$ excites a natural mode of the inviscid problem, and consequently can be expected to yield a resonant solution.

The failure of the method in this case is most likely due to a breakdown of Craig's perturbation method rather than the collocation procedure. Craig's method assumes that the depth of the boundary layer is small in comparison with the total depth, an assumption that is clearly invalid at the corner of the basin.

The first test case of Section 6.3 may also be solved by the boundary collocation method. First, the continuation domain is determined and the ϕ_n's again chosen as the terms of an appropriate cosine series. The collocation proceeds essentially as before, except the boundary condition (6.15) is applied at collocation points lying on the two ends $x = 0$ and $x = 2$, with (6.46) applied only at collocation points on the lower boundary $z = h(x)$.

The results of this process, again using (6.46), with $N_a = 40$, $\omega = 0.66$, $N = 1.145$ and $\nu = 2.0 \times 10^{-5}$, are shown in Figure 6.5. The numerical procedure was again found to be stable.

In this example the boundary collocation solution bears a strong resemblance to that derived by internal collocation methods (Figure 6.1), although the imaginary component of the solution displays more fine structure than that of the internal collocation solution. This could be due to an insufficient number of harmonics being used in the internal collocation trial solution (6.19), but is more likely due to the fact that the first stage of Craig's technique does not account for viscous effects in the body of the fluid.

As a final test of the procedure, a viscous counterpart to (6.66) was sought.

As discussed previously, the inviscid solution (6.66) cannot be approximated by (6.55) when the ϕ_n are chosen as the terms of a cosine series.

The boundary collocation procedure was applied for several choices of collocation points, but a satisfactory solution could not be obtained. In every case the residual was found to be unacceptably large at the corners of the basin. Once more it would seem that choosing the ϕ_n as the terms of a cosine series is unsatisfactory. It is hoped that this problem might be overcome with a choice of ϕ_n more appropriate to subcritical basins. However, this avenue has not been pursued.

These results indicate that Craig's method in conjunction with the boundary collocation procedure of the previous section yields satisfactory solutions of the model, provided the bathymetry is nowhere shallow. In shallow bathymetry the procedure encounters difficulties due to the failure of both Craig's perturbation method and the eigenfunction expansion on which the procedure is based.

Second Stage Solution

The second stage of Craig's perturbation method is also easily implemented in terms of the boundary collocation method of Section 6.6.1.

Given the first stage solution $\psi^{(0)}$, a particular solution $\psi_p^{(1)}$ of (6.36) can be constructed from (6.37). The c–analytic continuation $\tilde{\psi}$ of the second stage solution $\psi^{(1)}$ is then determined using the method of the previous section by incorporating $\psi_p^{(1)}$ into ψ_0, the component of $\tilde{\psi}$ representing the boundary forcing.

Continuing the example of the semi–circle, it is easily verified that c–analytic continuation $\tilde{\psi}$ of the second stage solution $\psi^{(1)}$ can be represented as

$$\tilde{\psi} = \psi_0 + \psi_1 \tag{6.71}$$

where

$$\psi_0(x,z) = \psi^{(0)}(x,z) - \psi^{(0)}(x - z/c, 0) + b(x,z) \tag{6.72}$$

$$\psi_1(x,z) = \sum_{n=0}^{\infty} a_n[\phi_n(x - z/c) - \phi_n(x + z/c)] \tag{6.73}$$

$$b(x,z) = \begin{cases} B(x - z/c, 0) & \text{if } |x - z/c| \leq -1 \\ 0 & \text{if } |x - z/c| > -1. \end{cases} \tag{6.74}$$

As before, truncating this expansions leads to a straightforward boundary collocation procedure.

Figure 6.6 shows the results of this method for the first test case described in Section 6.3. Again $N_a = 40$, $\omega = 0.66$, $N = 1.145$ and $\nu = 2.0 \times 10^{-5}$. As was suspected in Section 6.4, the procedure appears unstable, accentuating higher order harmonics, and will not be considered further.

6.6.4 A Fully Viscous Model

With the breakdown of the second stage of Craig's perturbation technique, viscous effects within the body of the fluid remain unaccounted for. This section proposes a simple extension to the boundary collocation method of the previous section which allows these effects to be modelled effectively.

The boundary collocation method of the previous section solves the inviscid problem by representing its solution as a sum of the eigenfunctions of the inviscid model on an appropriate domain. The natural progression of this technique is to solve the viscous model by representing the solution as a sum of the eigenfunctions of the viscous model.

Unfortunately, in general this procedure leads to a numerically ill–conditioned collocation problem. Let

$$\psi(x,z) = X(x)Z(z)$$

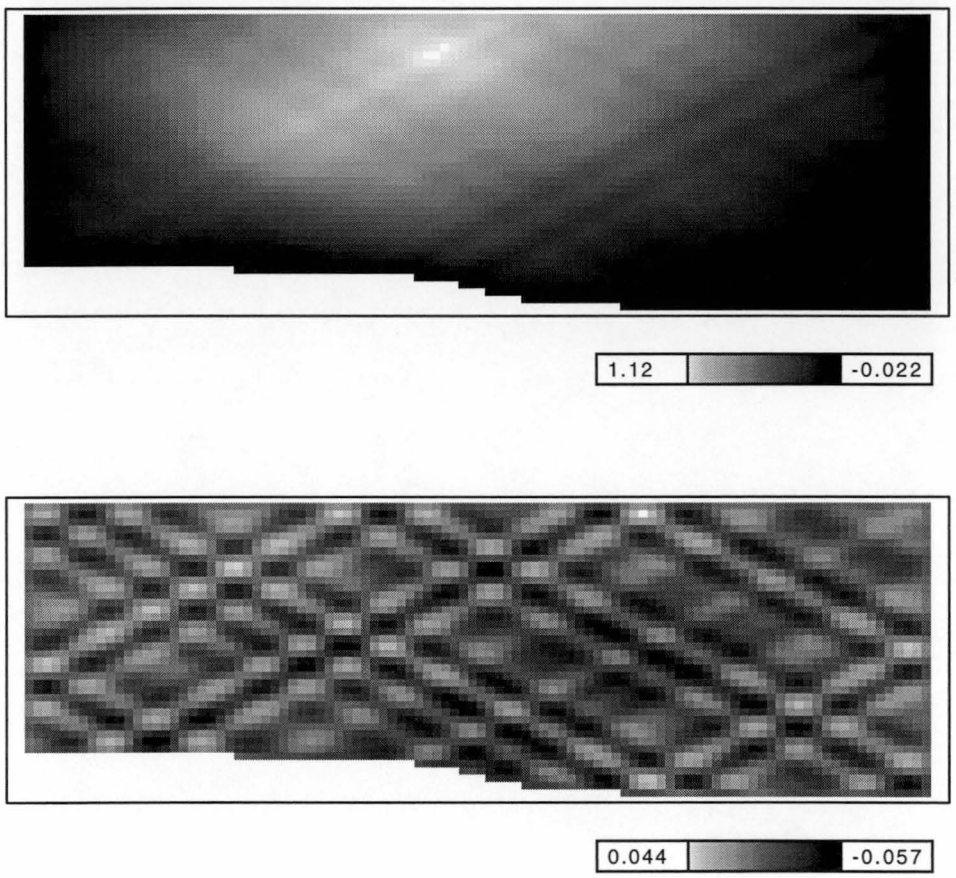

Figure 6.6: Solution of the first test case obtained by boundary collocation methods and Craig's perturbation technique, using the boundary condition (6.34), with $N_a = 60$, $\omega = 0.66$, $N = 1.145$ and $\nu = 2.0 \times 10^{-5}$. Top — $\Re\{\psi\}$, bottom — $\Im\{\psi\}$.

represent the eigenfunctions of the viscous model obtained by a standard separation of variables technique and consider the linearly independent components of $Z(z)$. There are four: one behaves approximately as sine, one as cosine, one is sharply exponentially decreasing with increasing depth, representing the behaviour of the solution in the boundary layer at the upper surface, and one is sharply exponentially increasing with increasing depth, representing the behaviour of the solution in the boundary layer at the lower boundary. It is with this last component of $Z(z)$ that the problem lies. Since its magnitude will vary enormously with depth, if the collocation points are situated at different depths the matrix problem resulting form the collocation will be ill–conditioned.

However, for certain simple examples the problem remains tractable. Consider the first test case discussed in Section 6.3. In the boundary collocation procedure of the previous section, the c–analytic continuation $\tilde{\psi}$ of the solution ψ was formed by continuing the definition of ψ along the surface $z = 0$. Equally well, $\tilde{\psi}$ could have been formed by continuing ψ along the left hand edge $x = 0$. This would result in a c–analytic continuation $\tilde{\psi}$ that satisfied the conditions

$$\tilde{\psi}(0, z) = 0 \tag{6.75}$$

$$\tilde{\psi}(2, z) = 0. \tag{6.76}$$

This in turn suggests that $\tilde{\psi}$ can be expanded as

$$\tilde{\psi}(x, z) = \sin\frac{\pi x}{2}\cos\frac{\pi z}{2c} + \sum_{n=1}^{\infty} a_n \sin\frac{\pi x}{2}\sin\frac{\pi z}{2c}. \tag{6.77}$$

Indeed, using this expansion as the basis of a boundary collocation scheme recovers the solution depicted in Figure 6.5. The advantage of this method is that the expansion (6.77) automatically satisfies the boundary conditions on $x = 0$ and $x = 2$, and thus collocation points need only be chosen from the lower boundary $z = h(x)$.

To obtain a viscous solution, $\tilde{\psi}$ is represented as a sum of the eigenfunctions

of the viscous model (6.4)

$$\tilde{\psi} = b(x,z) + \sin\frac{n\pi x}{2}\sum_{n=1}^{\infty}\sin\frac{n\pi x}{2}\left(a_n \sinh\alpha_{1n}z + b_n\sinh\alpha_{2n}z\right), \qquad (6.78)$$

where

$$b(x,z) = \sin\frac{n\pi x}{2}(\alpha_{2n}^2(\cosh\alpha_{1n}z + \sinh\alpha_{1n}z) - \alpha_{1n}^2\cosh\alpha_{2n}z)/(\alpha_{1n}^2 - \alpha_{2n}^2), \qquad (6.79)$$

and α_{1n} and α_{2n} satisfy the dispersion relation

$$\omega^2\alpha^2 + (N^2 - \omega^2)n^2\pi^2/4 = i\omega\nu\alpha^4. \qquad (6.80)$$

This expansion automatically satisfies the viscous boundary conditions at the surface $z = 0$ and at the two ends $x = 0$ and $x = 2$; the a_n and b_n must be chosen so that the boundary conditions (6.15) and (6.17) are satisfied on the lower surface $z = h(x)$. As before, truncating this expansion leads naturally to a boundary collocation procedure, but in this case at each collocation point the trial solution must satisfy both (6.15) and (6.17).

The fact that the collocation points need only be chosen from the lower boundary $z = h(x)$, coupled with the small depth variation of $h(x)$, makes the procedure numerically viable for this example, as the eigenfunction with exponential behaviour in z need only be evaluated over a relatively small range of depths.

Even with this simplification the problem is poorly conditioned. Figure 6.7 shows the results of this procedure for the first test case of Section 6.3 using 60 terms in the expansion. Even for this very simple bathymetry where the variation in depth is relatively small, with $\nu = 2 \times 10^{-5}$ the procedure is at the limit of typical machine floating point precision. Although the solution gives excellent agreement with the solution obtained by interior collocation, evidence of the instability of the method can be seen in the imaginary component of the solution at the very lower left of the basin.

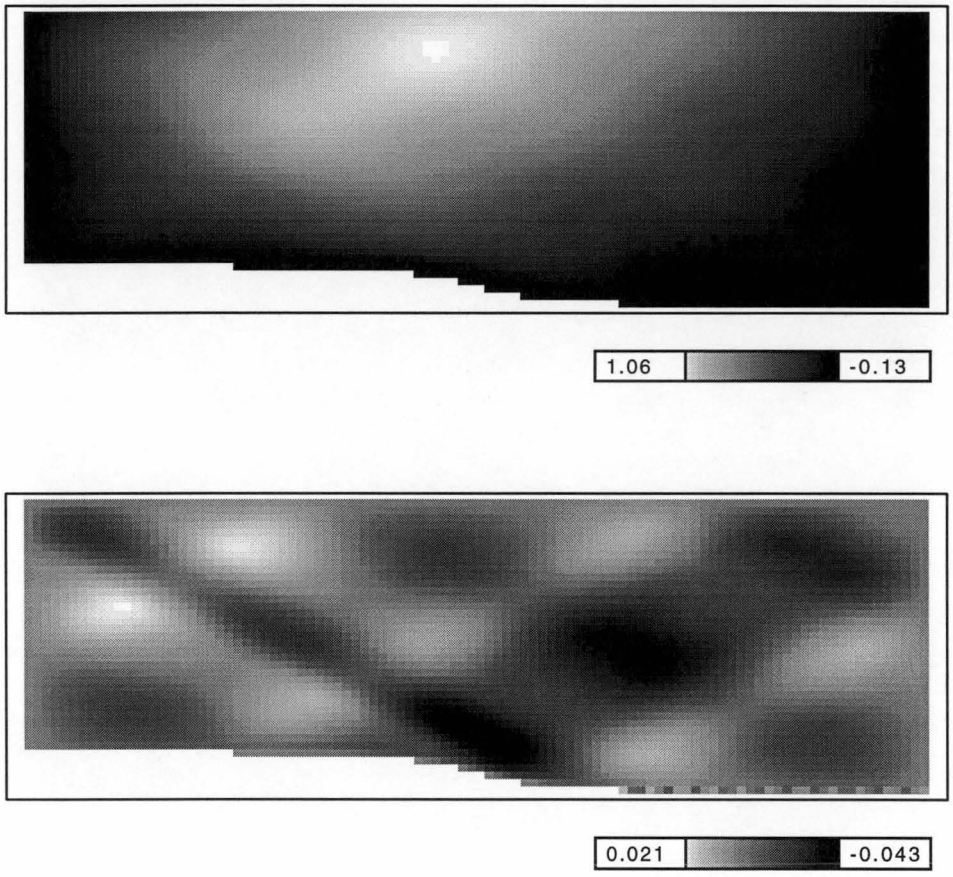

Figure 6.7: Fully viscous solution of the first test case obtained by expanding in terms of the viscous eigenfunctions, with $N_a = 60$, $\omega = 0.66$, $N = 1.145$ and $\nu = 2.0 \times 10^{-5}$. Top — $\Re\{\psi\}$, bottom — $\Im\{\psi\}$.

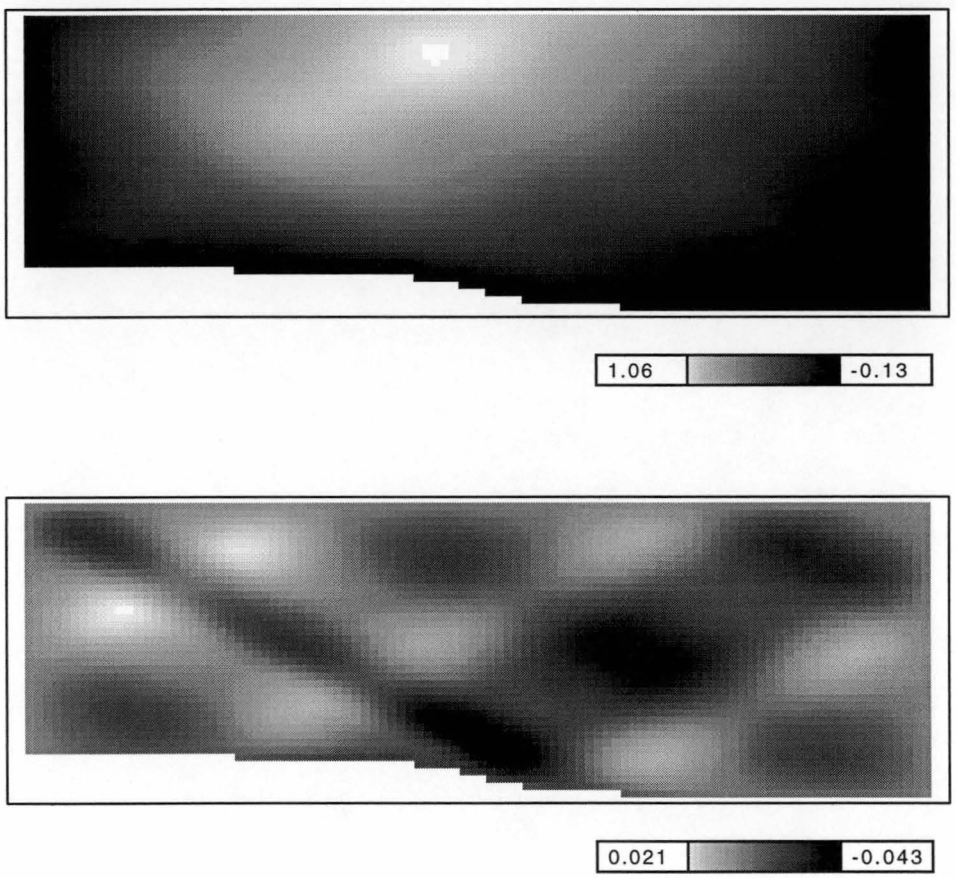

Figure 6.8: Fully viscous solution of the first test case obtained with Craig's boundary condition and expanding in terms of the viscous eigenfunctions, with $N_a = 60$, $\omega = 0.66$, $N = 1.145$ and $\nu = 2.0 \times 10^{-5}$. Top — $\Re\{\psi\}$, bottom — $\Im\{\psi\}$.

Since this ill–conditioning arises as a result of the eigenfunction representing the behaviour of the solution in the bottom boundary layer, the obvious resolution to the problem is to remove this eigenfunction from the expansion, and apply Craig's perturbation method at the bottom boundary. The results of this procedure for the first test case are shown in Figure 6.8. Again, there is excellent agreement with the interior collocation solution.

This procedure is found to be numerically stable for both small ($\nu \sim 10^{-6}$) and large ($\nu \sim 10^{-5}$) values of the viscosity, but surprisingly, was found to be unstable when $3 \times 10^{-5} < \nu < 8 \times 10^{-5}$. The reason for this remains unclear.

It must be stressed that unlike expanding the solution in terms of the inviscid eigenfunctions, no formal justification has been provided for expanding the solution in terms of the viscous eigenfunctions. Nevertheless, this procedure has been tested for a variety of topographies, and in every case has been in excellent agreement with the interior collocation method.

6.6.5 More General Topographies.

The boundary collocation methods developed in the preceding sections all stem from the theory of c–analytic continuation, and hence have assumed that the domain is characteristically convex. These methods are easily extended to more complex regions in a similar fashion to Sandstrom's method (section 3.4.2).

To apply the boundary collocation procedures of the previous sections to a region Ω that is not characteristically convex, first Ω is decomposed into finite union of characteristically convex regions Ω_1, Ω_2 ... Ω_n. On each of the Ω_i, ψ is expanded as before. Collocation points are then chosen from both the original boundary $\partial\Omega$ and the boundaries between the Ω_i. At a collocation point lying on $\partial\Omega$, the collocation proceeds as before. At those collocation lying on a boundary between two Ω_i's, two collocation conditions are applied — one enforcing the continuity of ψ across the boundary, and one enforcing the continuity of $\partial\psi/\partial n$,

the normal derivative of ψ at that boundary.

The main problem associated with this technique lies in choosing an appropriate set of collocation points. For a characteristically convex region the obvious choice was to choose the collocation points as the first neglected mode of the expansion. But in this case, each adjacent pair of Ω_i share collocation points along their common boundary. What proves to be a suitable choice of collocation points for one Ω_i may prove to be unsuitable for its neighbour. In practice, an inappropriate choice of collocation points was found to be a major source of instability, and is a topic for further investigation.

This method described here is effectively the same technique used by Sandstrom to extend his technique to non–characteristically convex regions, and it suffers the same disadvantage — the procedure becomes unwieldy for regions where the topography continually changes from subcritical to supercritical. However, given the simplicity of the boundary collocation method, the procedure remains tractable for most topographies of interest.

But more importantly, the procedure described here can be viewed as the generalization to arbitrary topographies of the Fourier methods used extensively by other authors.

6.7 Summary

This chapter has developed several new solution methods for the viscous internal tide problem on a closed basin. In the next chapter these methods are applied to a practical problem.

Chapter 7

Tank Experiments

To test the models described in the preceding chapters, two laboratory experiments were conducted. This comparison of model and data forms the basis of the current chapter.

The experiments took two forms. In the first experiment, internal waves were generated in a tank configured to loosely resemble a shelf topography. Analysis of the resulting data prompted a second experiment designed to investigate resonance effects more directly. For the second experiment the shelf was removed and the tank fitted with a vertical baffle to form a resonating cavity.

In both cases, resonance effects were seen to play a major role in determining the motion of fluid. However, the strongly resonant motions predicted by the linear models were not observed.

7.1 The Tank

The apparatus used for each experiment was effectively the same, differing only in the configuration of the tank.

The tank was of a glass construction, with dimensions $1.78m \times 0.20m \times 0.39m$ (Figure 7.1), and was fitted with plastic guides to facilitate the placement of the

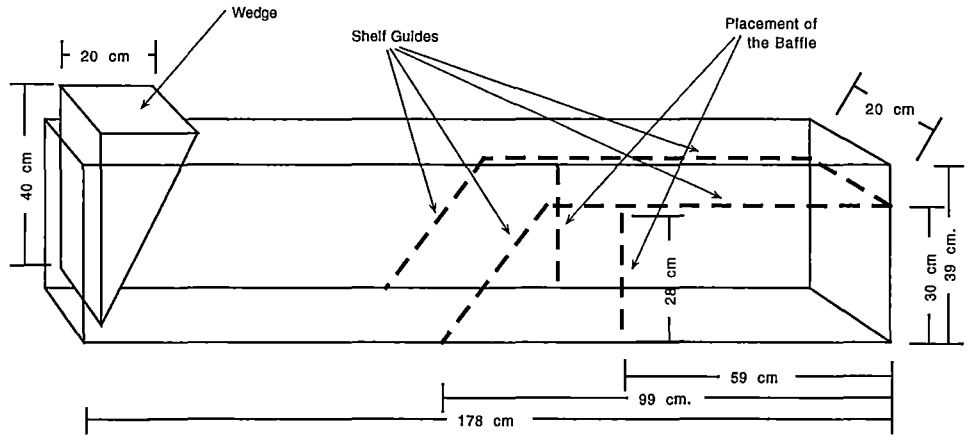

Figure 7.1: This figure shows the outlay of the tank. All measurements internal. The motor assembly used to drive the wedge is not shown.

flexible plastic sheet used to simulate the shelf.

The tank was filled with a continuously stratified brine as follows. Two large ($60l$) supply tanks, joined at the base by a stop–cock, were filled with fresh water, the stop–cock, opened and the fluid allowed to come to rest. The stop–cock was then closed and $10Kg$ of salt dissolved in the first tank. Once dissolved, an equal mass of brine was removed from this tank to equalize the pressure at the stop–cock, and the tap re–opened. Fluid was then pumped from the tank to fill the glass wave tank. As fluid was removed from the second supply tank, brine was drawn through the stop–cock from the first tank and the mixture became increasingly saline.

The wave tank was filled by means of a weighted hose that was gently removed when the tank was full. In the case of the baffle experiment, thin dye layers were injected into the solution as the tank was filled.

The plastic shelf or the baffle were then introduced to the tank as appropriate. Although this resulted in a slight disturbance of the stratification, adding the shelf or baffle after the tank was filled ensured the fluid retained a linear density profile.

Overall, this procedure was found to be very reliable and produced consistent

linear salinity profiles.

The motion was externally forced by a triangular wedge driven by a variable speed electric motor affixed to one end of the tank. The wedge was of side–length $0.20m \times 0.40m$ and had a peak to peak vertical motion of $0.029m$. The wedge was fitted to the tank last of all.

For the baffle experiment, the motion was monitored by means of the dye layers introduced as the tank was filled. For the shelf experiment, beads of varying densities were added to the fluid. The beads remain suspended in the fluid at a height commensurate with their density, allowing the motion of the fluid to be photographically charted. An attempt was also made to monitor the flow with a Schlieren technique(Mowbray and Rarity[34]), but this method was not favoured due to the difficulty in obtaining quantitative data.

7.2 The Shelf Experiment

The shelf experiment was conducted first. It was found that the models do not accurately reproduce the results of the experiment, but this is attributed to the simplistic manner in which the wedge was represented in the models.

The apparatus was set up as described in the previous section. The tank was filled to a depth of $0.38m$ and the buoyancy frequency of the fluid was measured at $1.41s^{-1}$. The experiment was started from rest and run for several minutes to allow any transients to die away. A $35mm$ motor–driven camera was then used to record the positions of the marker beads, shooting 36 frames at $1s$ intervals. The period of the external forcing was noted to be $10.4s$.

It was then attempted to reproduce the observed motion with the models discussed in the preceding chapters.

The main difficulty in modelling the shelf experiment is in accurately representing the action of the wedge. The wedge acts as a moving boundary changing the shape of the tank as it moves. The motion induced by the wedge is vertical,

but is quickly commuted to a largely horizontal motion by the action of the fluid. In the neighbourhood of the wedge the dynamics of the the fluid are extremely complicated.

Rather than attempt to model these complex dynamics, it was assumed that the motion is robust to the exact form of external forcing, and the effect of the wedge was approximated by the barotropic forcing function described by Craig[14]. Under this assumption the boundary conditions are those given by (6.15) – (6.17), with $B(x,z)$ given by

$$B(x,z) = \sin \pi x/2(1 - z/h(x)). \tag{7.1}$$

The motion was modelled under 3 differing sets of assumptions:

- that the motion was inviscid and that the ends of the tank acted as radiating boundaries,
- that the motion was viscous and that the ends of the tank acted as reflecting boundaries, and
- that the motion was viscous and that the ends of the tank acted as reflecting boundaries, but that the action of the wedge shortened the effective length of the tank.

None of these simulations was found to satisfactorily describe the motion observed in the tank. This failure was attributed to the simplistic representation of the wedge.

Figure 7.2 show the result of modelling the experiment with the inviscid model (3.1), assuming a radiation condition at each lateral boundary rather then treating the tank as closed. Although an inaccurate representation of the tank, this gives an useful comparison from which the effects of the end boundaries may be judged.

Figure 7.2 was derived with the collocation procedure described in Section 3.2.

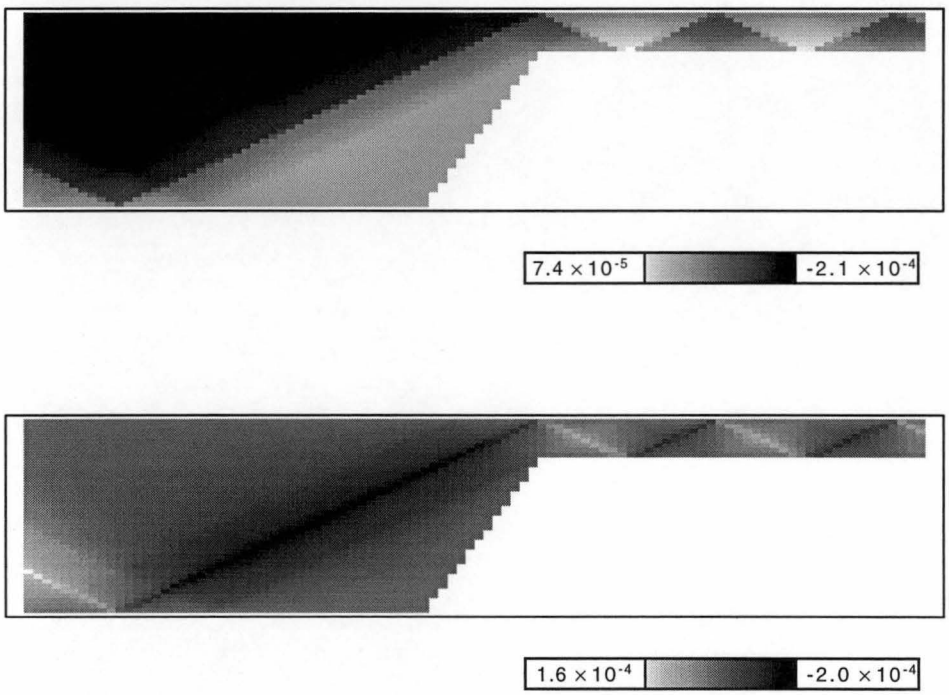

Figure 7.2: Modelling the shelf experiment with the inviscid model 3.1, assuming that the ends of the tank act as radiating boundaries. The top figure depicts $\Re\{\psi\}$ and the lower figure $\Im\{\psi\}$, for $N = 1.41s^{-1}$ and $\omega = 0.6s^{-1}$.

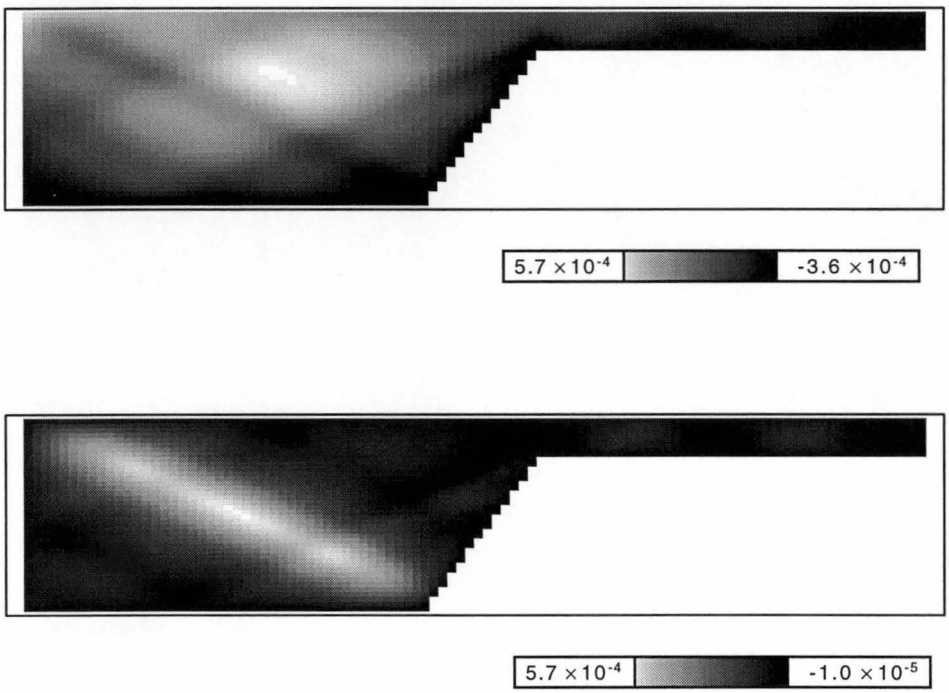

Figure 7.3: Modelling the shelf experiment assuming that the motion is viscous and that the ends of the tank act as reflecting boundaries. The top figure depicts $\Re\{\psi\}$ and the lower figure $\Im\{\psi\}$, for $N = 1.41s^{-1}$, $\omega = 0.6s^{-1}$ and $\nu = 10^{-6}m^2s^{-1}$.

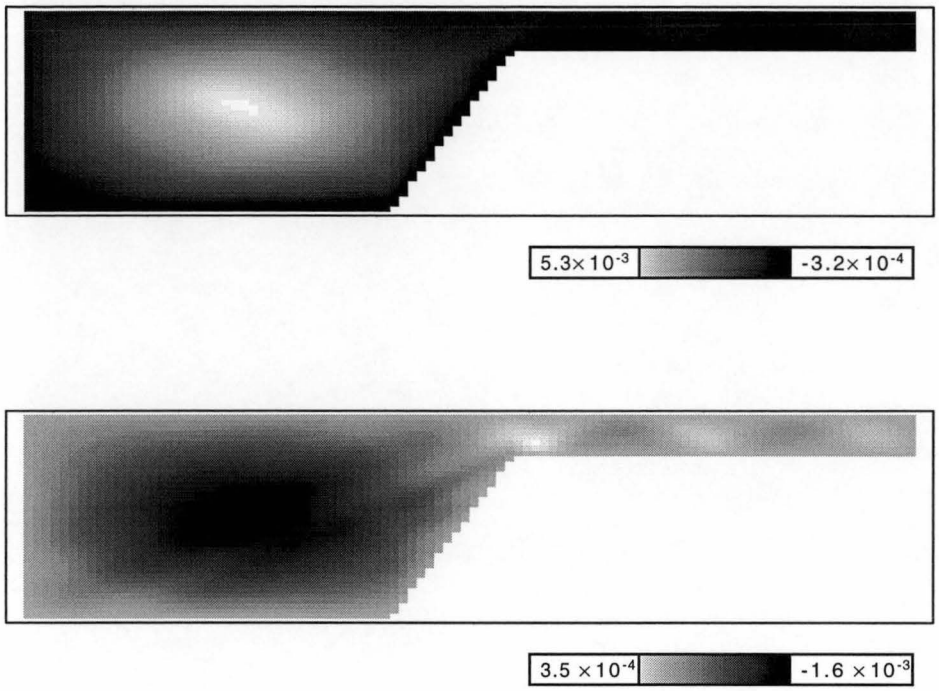

Figure 7.4: Modelling the shelf experiment assuming that the motion is viscous and that the ends of the tank act as reflecting boundaries, but that the action of the wedge shortens the effective length of the tank. The top figure depicts $\Re\{\psi\}$ and the lower figure $\Im\{\psi\}$, for $N = 1.41s^{-1}$, $\omega = 0.6s^{-1}$ and $\nu = 10^{-6}m^2s^{-1}$.

Figure 7.3 shows the result of modelling the experiment with the viscous model (6.4), treating the tank as closed, and assuming a zero slip boundary condition on the bottom surface. The interior collocation method of Section 6.3 and the boundary collocation method of Section 6.6.4 were found to yield almost identical solutions for this problem; Figure 7.3 shows the interior collocation solution.

The strong diagonal feature that dominates in the deeper portion of the tank in Figure 7.3 was not observed in the physical experiment.

In an attempt to explain this discrepancy, it was hypothesized that the action of the wedge may have the effect of shortening the length of the tank. Figure 7.4 shows the result of repeating the simulation of Figure 7.3 for a tank that is

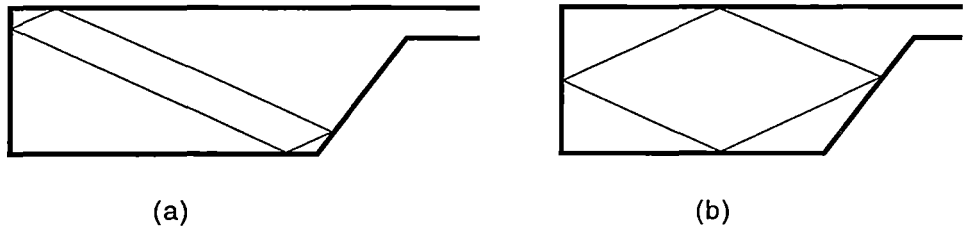

Figure 7.5: Characteristic circuits for the shelf experiment. This figure shows the characteristic circuits corresponding to the resonances seen in Figures 7.3 and 7.4. The diagram on the characteristic circuit for the tank of Figure 7.3, while the diagram on the right show the characteristic circuit for the shortened tank of Figure 7.4.

$0.1m$ shorter at the wedge end. But again, the deeper section is dominated by a strong diagonal feature.

Yet Figures 7.3 and 7.4 are entirely consistent with the discussion of Section 4.5 relating characteristic paths and resonant solutions. The diagonal features present in these figures are clearly resonance phenomena, hence their absence when the ends of the tank are treated as radiating boundaries (Figure 7.2).

Figure 7.5 shows to scale the characteristic circuits of the tank corresponding to Figures 7.3 and 7.4. The correspondence between the characteristic circuits shown in Figure 7.5 and the diagonal features of Figures 7.3 and 7.4 is plain. In each case there exists a single characteristic circuit contained in the deeper portion of the tank. Under the inviscid theory this is insufficient to yield a resonant solution, but as argued in Section 4.5, the viscous model does yield a resonant solution.

Furthermore, examining Figure 7.5 it can be seen that for a tank of this geometry, a single characteristic circuit will exist for a range of dimensions of the tank. So the resonance will be robust to finitely large perturbations in the dimensions of the tank, as Figures 7.3 and 7.4 have shown.

There are two possible explanations as to why the resonance is not observed

in the physical experiment. Nonlinear effects ignored in the linear model (6.4) could be responsible. But the more obvious explanation is that the presence of the wedge alters the geometry of the tank, the characteristic circuits depicted in Figure 7.5 do not occur, and so resonant solutions do not form. Although this second explanation seems the more likely, it is unclear how this hypothesis can be tested. The motion of the wedge is inherently a time dependent phenomenon. But analysis of characteristics is independent of time and so it is unclear how the interaction of the wedge and the characteristics can be represented.

This second hypothesis strongly suggests that geometry simplifying assumptions like those used by Cushman–Roisin *et al.*[17], Tverberg *et al.*[45], and de Young and Pond [18], are not appropriate to an analysis of resonant motions.

Rather than investing more effort to accurately model the action of the wedge, it was decide to investigate resonance effects more directly.

7.3 The Resonant Rectangular Basin

Before discussing the baffle experiment, it is necessary to establish some simple theoretical estimates pertaining to resonant motion on a rectangular basin.

Consider solving the viscous model (6.4) on a rectangular basin of depth h and width l, the upper left hand corner of which is located at the origin. To simplify the analysis, a zero stress condition (Pond and Pickard[37]) is adopted at each boundary, and it is assumed that the external forcing applied at the upper surface $z = 0$ of the basin consists of a single mode

$$\psi(x, 0) = \sin n\pi x/l, \tag{7.2}$$

while

$$\psi = 0 \tag{7.3}$$

on the lower three boundaries.

A solution of (6.4) satisfying these boundary conditions is given by

$$\Psi(x,z) = \sin\frac{n\pi x}{l} Z(z,n), \tag{7.4}$$

where

$$Z(z,n) = \frac{\beta_{2n}^2}{\beta_{2n}^2-\beta_{1n}^2}\,\frac{\sin\sqrt{\beta_{1n}}\,(z-h)}{\sin\sqrt{\beta_{1n}}\,h} - \frac{\beta_{1n}^2}{\beta_{2n}^2-\beta_{1n}^2}\,\frac{\sin\sqrt{\beta_{2n}}\,(z-h)}{\sin\sqrt{\beta_{2n}}\,h}, \tag{7.5}$$

and β_{1n} and β_{2n} are the two roots of the quadratic

$$i\nu\omega\beta^2 - \omega^2\beta + n^2\pi^2(N^2-\omega^2)/l^2 = 0. \tag{7.6}$$

The behaviour of ψ may be characterized purely in terms of $Z(z,n)$ but to further simplify the analysis, only the half depth value $H(n) = Z(-h/2,n)$ will be considered. Expanding sine in multiple angles of $h/2$, $H(n)$ may be written

$$H(n) = \frac{\beta_{2n}^2}{\beta_{2n}^2-\beta_{1n}^2}\sec\frac{\sqrt{\beta_{1n}}\,h}{2} - \frac{\beta_{1n}^2}{\beta_{2n}^2-\beta_{1n}^2}\sec\frac{\sqrt{\beta_{2n}}\,h}{2}. \tag{7.7}$$

The major characteristics of $H(n)$ can be determined from a simple singular perturbation process in the perturbation parameter $\nu_* = i\nu$. First, assume that β_{1n} may be expanded in the form

$$\beta_{1n} = b_{0n} + b_{1n}(\nu_*) + O(\nu_*^2). \tag{7.8}$$

Substituting into (7.6) and equating powers of ν_* yields

$$b_{0n} = \frac{n^2(N^2T^2-4\pi^2)}{4l^2}, \tag{7.9}$$

$$b_{1n} = \frac{n^4T(N^2T^2-4\pi^2)^2}{32\pi l^4}, \tag{7.10}$$

where ω has been replaced by $2\pi/T$. From the expression for the sum of the roots of a quadratic

$$\begin{aligned}\beta_{2n} &= \frac{2\pi}{T}\nu_*^{-1} - \beta_{1n}\\ &= \frac{2\pi}{T}\nu_*^{-1} - \frac{n^2(N^2T^2-4\pi^2)}{4l^2} - \frac{n^4T(N^2T^2-4\pi^2)^2}{32\pi l^4}\nu_* + O(\nu_*^2).\end{aligned} \tag{7.11}$$

Substituting these expressions into (7.7) and collecting higher order terms in ν_* yields

$$H(n) = \sec \frac{h\sqrt{b_{0n} + b_{1n}\nu_*}}{2} + O(\nu^2). \tag{7.12}$$

It is this simplified expression for $H(n)$ that allows several important characteristics of the resonance to be determined.

Let the term *inviscid resonance* denote a period T at which the inviscid model (3.1) has no solution corresponding to the external forcing (7.2), and let the term *viscous resonance* denote a period at which the solution of the viscous model (6.4) is $\pi/2$ out of phase with the external forcing. Note that in general, viscous resonance will not coincide exactly with the period at which $\|\psi\|$ is a maximum.

It is clear from (7.12) that inviscid resonance will occur when

$$h\sqrt{b_{0n}} = k\pi \qquad k = 1, 3, 5 \ldots, \tag{7.13}$$

that is, when

$$T_{kn} = \frac{2\pi\sqrt{k^2l^2 + n^2h^2}}{nNh}. \tag{7.14}$$

As expected, this is strictly equivalent to the condition for inviscid resonance (4.31) determined in Section 4.2.3. The expansion (7.12) only detects resonances corresponding to odd mode numbers k because $H(n)$ represents the the half depth amplitude of the motion. Even order resonant modes will be approximately zero at $h/2$.

At viscous resonance, $\Re\{H(n)\} = 0$. Applying (7.12), an estimate of the viscous resonance period can be obtained by solving

$$\Re\{h\sqrt{b_{0n} + b_{1n}\nu_*}\} = k\pi \qquad k = 1, 3, 5 \ldots. \tag{7.15}$$

for the period T. For typical parameter values, this viscous correction to the resonant period is quite small.

An estimate of the amplitude of ψ at viscous resonance may be obtained from its amplitude at inviscid resonance. Expanding (7.12) in powers of ν_* about an inviscid resonance point yields

$$H(n) = (-1)^{\frac{k+1}{2}} \left[\frac{4k\pi}{b_{1nk}h^2\nu} \nu_*^{-1} + \frac{1}{k\pi} + \left(\frac{k^2\pi^2 - 6}{24k^3\pi^3} \right) b_{1nk}h^2\nu_* \right] + O(\nu^2), \quad (7.16)$$

where b_{1nk} denotes the value of b_{1n} at the k^{th} inviscid resonance and is given by

$$b_{1nk} = \frac{k^4\pi^4\sqrt{k^2l^2 + h^2n^2}}{nh^5N}. \quad (7.17)$$

This representation of $H(n)$ clearly demonstrates the amplitude at resonance varies approximately as $k^{-4}\nu^{-1}$.

Expanding (7.12) in powers of ν_* about a point which is not an inviscid resonance point yields

$$H(n) = \sec\frac{h\sqrt{b_0}}{2} + \frac{b_{1n}\sec\frac{h\sqrt{b_0}}{2}\tan\frac{h\sqrt{b_0}}{2}}{4h\sqrt{b_{0n}}}\nu_* + O(\nu_*^2). \quad (7.18)$$

Since both b_0 and b_1 are real and ν_* is purely imaginary, the real part of this expansion consists of all those terms containing even powers of ν_*, while the imaginary component consists of all those terms containing odd powers of ν_*. Thus $\arg H(n)$ may be written

$$\arg H(n) = \arctan\left[\frac{b_{1n}h/(4\sqrt{b_{0n}})\sec\frac{h\sqrt{b_0}}{2}\tan\frac{h\sqrt{b_0}}{2} + \text{odd powers of } \nu}{\sec\frac{h\sqrt{b_0}}{2} + \text{even powers of } \nu} \right], \quad (7.19)$$

or, by expanding arctan,

$$\arg H(n) = \arctan\left[\frac{hb_{1n}\tan\frac{h\sqrt{b_0}}{2}}{4\sqrt{b_0}}\nu \right] + O(\nu^3). \quad (7.20)$$

Away from a point of inviscid resonance, the argument of the arctan term is small and (7.20) can be further simplified to

$$\arg H(n) = \frac{hb_{1n}\tan\frac{h\sqrt{b_0}}{2}}{4\sqrt{b_0}}\nu + O(\nu^3). \quad (7.21)$$

However, it must be remembered that this is an expansion of arctan and hence must be interpreted modulo π.

This representation of $\arg H(n)$ clearly shows the sharp phase variations exhibited by the system near resonance.

The analysis of this section has assumed a zero stress condition at the boundary. Similar results may be derived for more complex boundary conditions, but the algebra is considerably more tedious.

7.4 The Baffle Experiment

The outcome of the shelf experiment prompted a second experiment aimed at investigating resonance more directly. The intention was to experiment with resonant motion on a simple rectangular basin, but rather than treat the tank as one large basin, a vertical baffle was used to separate the tank into two compartments. It was hoped that in this way the compartment containing the wedge could be neglected and the remaining compartment treated as a resonant cavity, thus avoiding the problems encountered in modelling the wedge in the shelf experiment.

The tank was again filled to a depth of $0.38m$. Dye was introduced to the fluid as the tank was filled, resulting in two well defined dye layers at depths of approximately $0.11m$ and $0.24m$ below the surface. The buoyancy frequency of the fluid was measured to be $1.45s^{-1}$. A vertical baffle of height $0.28m$ was fitted to the tank $0.59m$ from the non–wedge end, separating the tank into two compartments. These compartments will henceforth be referred to as the wedge and non–wedge compartments. The experiment was started from rest and the period T of the external forcing slowly varied between $7s$ and $12s$.

For the observed values of the parameters, the inviscid theory of Chapter 4 predicts a resonance at approximately $T = 7.97s$. This corresponds to a series of characteristic circuits that form about the main diagonal of the non–wedge

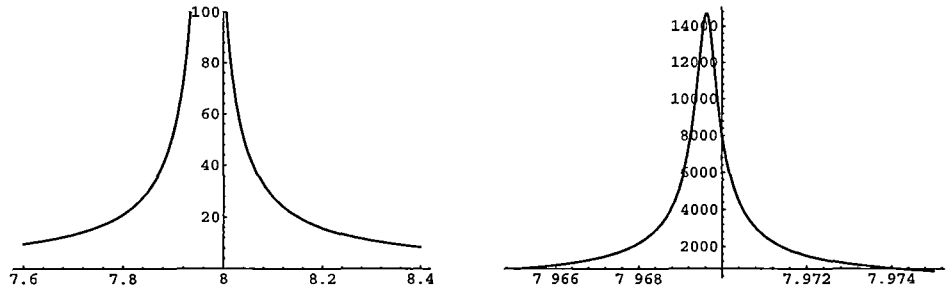

Figure 7.6: $||H(1)||$ versus T for the baffle experiment

compartment, as shown in Figure 7.8(a). These characteristic paths exist independently of the geometry of the wedge compartment, implying that resonance should be observed independently of the wedge compartment.

Yet despite this prediction, no resonance was observed for $T \approx 7.97s$. In fact, at this period the fluid was virtually motionless. However, a spectacular large amplitude motion was noted at $T \approx 9.5s$. For forcing of this period, the vertical oscillation of the dye layers increased slowly from rest to reach a maximum peak to peak amplitude of approximately $0.07m$ in the top layer, and approximately $0.06m$ in the lower layer. At the same time, the displacement of the free surface was observed to be less than $1mm$.

Upon more detailed analysis, it is found that these results are in fact consistent with theory.

To explain the absence of the resonance at $T = 7.97s$ it was hypothesized that the peak may be too sharp to be observed. But if the non–wedge compartment is approximated by a rectangular basin like that described in the previous section, since the model is linear, the ratio $\psi(x,0)/\psi(x,-h/2)$ should behave approximately as $H(1)$, defined by (7.12). Figure 7.6 shows two plots of $||H(1)||$ versus T for the parameter values relevant to the baffle experiment. Although the resonant peak is extremely sharp, $||H(1)||$ is still quite large at the tails of the peak, suggesting that it is unlikely that the peak could pass unnoticed.

It is when the solution of the viscous model (6.4) is examined that the real

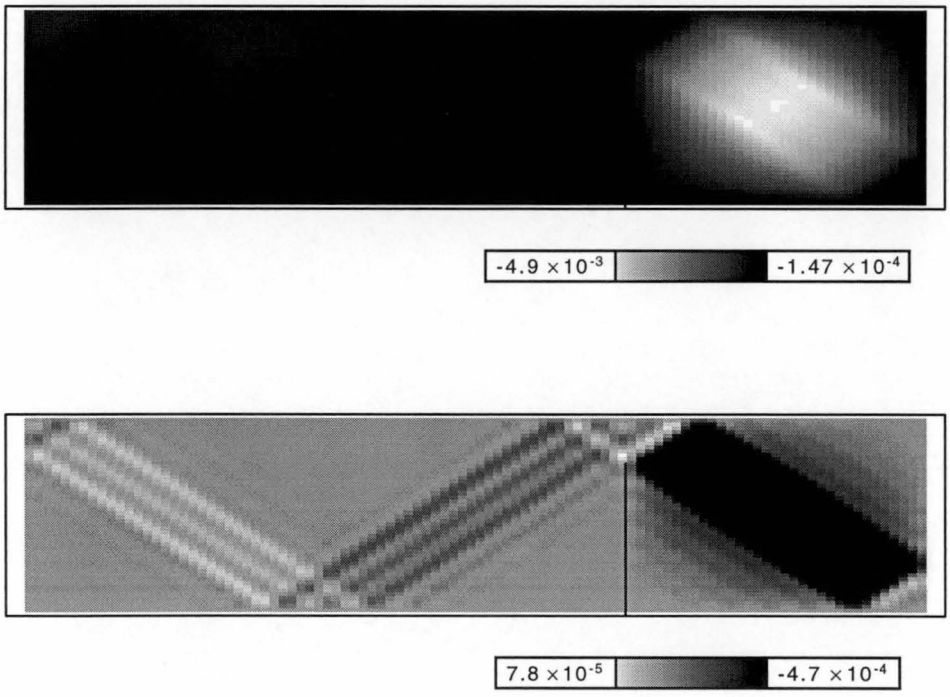

Figure 7.7: Simulating the baffle experiment for $T = 7.97s$, $N = 1.45s^{-1}$ and $\nu = 10^{-6}m^2s^{-1}$. Top — $\Re\{\psi\}$, bottom — $\Im\{\psi\}$.

explanation becomes obvious. Figure 7.9 shows the solution of the model for $T = 7.97s$, assuming a zero slip condition on the bottom of the tank. The fluid velocities predicted by this solution are enormous, representing an increase of several orders of magnitude over the velocity of the wedge. This solution clearly violates the assumption of small amplitude motion under which the linear model (6.4) was derived.

This breakdown of the model at resonance clearly indicates the need for a nonlinear model of resonance. This topic is taken up in the next chapter.

The resonance that was observed at $T \approx 9.5s$ is also predicted by the theory. At $T = 9.47s$ the tank possesses two thin bands of characteristic circuits, as shown in Figures 7.8 (b) and (c). In contrast to the circuits of Figure 7.8 (a), these circuits are dependent upon the geometry of the wedge compartment, implying that the resonance occurs as a result of the interaction between the two compartments.

Figure 7.9 shows the result of modelling the motion with the viscous model (6.4), assuming a zero slip condition on the bottom of the tank. The resonant motion in the non–wedge compartment can be clearly seen. Note also that the characteristic circuits depicted in Figures 7.8 (b) and (c) can be clearly seen in the imaginary component of this solution, and to a lesser extent in the real component.

Furthermore, the model correctly predicts the amplitude of oscillation of the dye layers. If the velocity field corresponding to Figure 7.9 is calculated from (6.2) and then integrated to calculate the path of a fluid parcel, the maximal displacement of a fluid parcel situated in the upper dye layer is found to be approximately $0.07m$, as observed in the experiment.

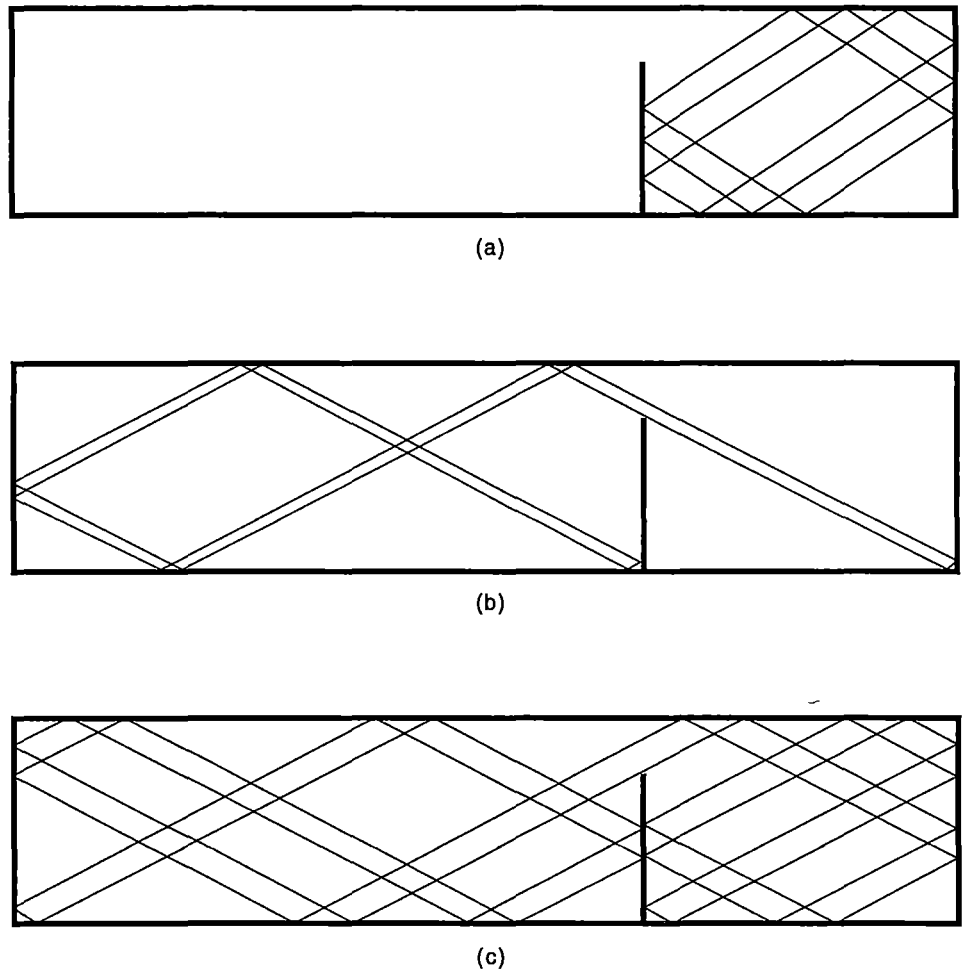

Figure 7.8: Characteristic circuits for the baffle experiment. Figure (a) shows several representative members of the family of characteristic circuits that form at $T = 7.97s$. Figures (b) and (c) show the outermost member of each of the two thin bands of characteristic circuits that form at $T = 9.47s$. In each case, the compartment on the left represents the wedge compartment.

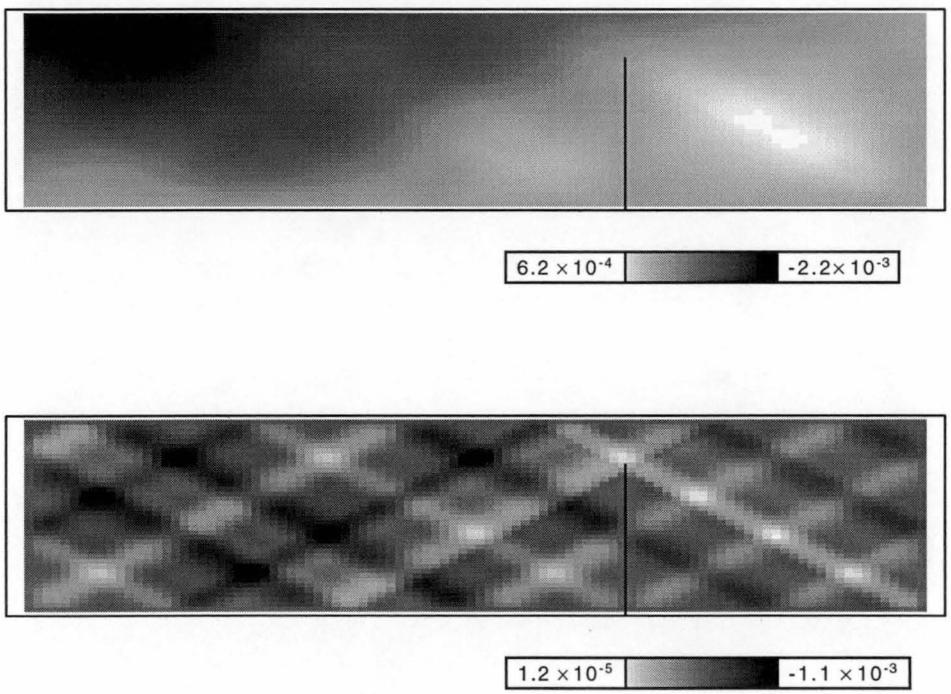

Figure 7.9: Simulating the baffle experiment for $T = 9.46s$, $N = 1.45s^{-1}$ and $\nu = 10^{-6}m^2s^{-1}$. Top – $\Re\{\psi\}$, bottom – $\Im\{\psi\}$.

7.5 Summary

Overall, the experiments cannot be described as an overwhelming success. But this merely serves to highlight the exacting nature of the problem. Although in general the results of the chapter support the conclusions drawn in previous chapters, it has been seen that the linear models may breakdown under strongly resonant motions. The next chapter considers a nonlinear model of internal tide motion.

Chapter 8

A Non-Linear Model

The experiments of the previous chapter clearly demonstrate a breakdown of the linear models of internal tide motion near resonance. In this chapter a non–linear model based on the Navier Stokes equations is considered.

8.1 The Model

As described in Chapter (2), internal tide motion can be completely described with the two dimensional incompressible Navier Stokes equations,

$$u_t + uu_x + wu_z = -\frac{p_x}{\rho} + \nu\nabla^2 u \tag{8.1}$$

$$w_t + uw_x + ww_z = -\frac{p_z}{\rho} + \nu\nabla^2 w + g \tag{8.2}$$

$$u_x + w_z = 0 \tag{8.3}$$

supplemented by the density transport condition

$$\rho_t + u\rho_x + w\rho_z = 0, \tag{8.4}$$

where $\rho(x,z,t)$, $p(x,z,t)$, $u(x,z,t)$ and $w(x,z,t)$ denote respectively the fluid density, pressure and horizontal and vertical fluid velocities, g is the acceleration due to gravity and ν the coefficient of viscosity.

At a solid boundary, the boundary conditions consist of a zero flux condition together with an appropriate viscous condition. At the (upper) free surface, represented as $z = \zeta(x,t)$, a zero stress condition is imposed, indicating the absence of wind induced stresses at the surface, together with the conditions

$$\zeta_t + u\zeta_x = w \qquad \text{on } z = \zeta, \tag{8.5}$$

$$\rho = \rho_0(\zeta_0) \qquad \text{on } z = \zeta, \tag{8.6}$$

$$p = p_0(\zeta_0) \qquad \text{on } z = \zeta, \tag{8.7}$$

where $\rho_0(z)$ and $p_0(z)$ represent the hydrostatic density and pressure distributions, and $z = \zeta_0$ represents the mean position of the free surface.

In this chapter the solutions of this model are be compared with the solutions of its linearized counterpart (also described in Chapter 2)

$$\rho_0 u_t = -p_x + \nu\rho_0\nabla^2 u \tag{8.8}$$

$$\rho_0 w_t = -p_z + \nu\rho_0\nabla^2 w + \rho' g \tag{8.9}$$

$$u_x + w_z = 0 \tag{8.10}$$

$$\rho'_t + w\rho_{0z} = 0, \tag{8.11}$$

where $\rho_0(z)$ again represents the hydrostatic density pressure distribution, and $\rho'(x,z,t)$ is now interpreted as the deviation from this value.

The boundary conditions for the linear model are essentially the same as for the nonlinear model, except at the upper (free) surface where, for consistency with the models of previous chapters, a rigid lid approximation is adopted. Thus at the upper surface (8.5) – (8.7) are replaced by

$$w(x,\zeta_0) = 0 \tag{8.12}$$

$$u_z(x,\zeta_0) = 0 \tag{8.13}$$

where again $z = \zeta_0$ represents the mean position of the free surface.

Since both (8.1) – (8.4) and (8.8) – (8.11) are time dependent models, initial conditions must also be supplied. In every case to be considered, it will be

assumed that the motion starts from rest and that both the initial pressure and density distributions $p_0(z)$ and $\rho_0(z)$ are known.

8.2 The Artificial Compressibility Method

Numerous numerical procedures for integrating the incompressible Navier Stokes equations have been described in the literature, but not all of these are suited to the internal tide problem near resonance. Accuracy is of prime importance. If the numerical procedure is to be used to compare the behaviour of the nonlinear with that of the linear model, it must be capable of accurately reproducing the strongly resonant motions predicted by the linear model. This is an obviously difficult task. If a small forcing at the boundary can induce a large amplitude motion elsewhere in the fluid, presumably a small error at the boundary can also induce a large change elsewhere in the flow. Several numerical schemes were tried, the most successful of these was found to be the artificial compressibility method described by Peyret and Taylor[36].

The artificial compressibility method proceeds by introducing a pseudo–time co–ordinate τ. In terms of pseudo–time τ, the fluid is considered compressible.

To integrate forward in time, the system (8.1) – (8.4) is first discretized in both time t and pseudo time τ. At each time step in t, the system is integrated forward in τ, treating the fluid as compressible, until equilibrium is reached. If the net volume of the fluid has remained constant, at equilibrium the fluid will satisfy the incompressibility condition (8.3).

Each τ time step proceeds as follows. First, new estimates of u, w, ρ and ζ are calculated from the discretized forms of (8.1), (8.2), (8.4) and (8.5). The pressure estimate is then updated according to the relation

$$\Delta p = \lambda(u_x + w_z) \tag{8.14}$$

where λ is a constant that must be chosen to ensure the convergence of the

method. Thus the pressure is increased where the divergence $\nabla \underline{v}$ indicates the fluid is in compression, and decreased where the fluid is in expansion. This procedure is strictly equivalent to treating the fluid as a compressible fluid in the pseudo–time coordinate, satisfying the equation of state

$$p = k^2 \rho \tag{8.15}$$

for some constant k.

Representing (8.1), (8.2), (8.4) and (8.5) as

$$u_t = L_u(u, w, \rho, p) \tag{8.16}$$

$$w_t = L_w(u, w, \rho, p) \tag{8.17}$$

$$\rho_t = L_\rho(u, w, \rho), \tag{8.18}$$

$$\zeta_t = L_\zeta(u, w, \zeta), \tag{8.19}$$

this algorithm may be succinctly expressed as

$$u^{(i+1,j+1)} = u^{(i+1,j)} + u^{(i,*)} + \lambda_u \Delta t L_u(u^{(i+1,j)}, w^{(i+1,j)}, \rho^{(i+1,j)}, p^{(i+1,j)}) \tag{8.20}$$

$$w^{(i+1,j+1)} = w^{(i+1,j)} + w^{(i,*)} + \lambda_w \Delta t L_w(u^{(i+1,j)}, w^{(i+1,j)}, \rho^{(i+1,j)}, p^{(i+1,j)}) \tag{8.21}$$

$$\rho^{(i+1,j+1)} = \rho^{(i+1,j)} + \rho^{(i,*)} + \lambda_\rho \Delta t L_\rho(u^{(i+1,j)}, w^{(i+1,j)}, \rho^{(i+1,j)}, p^{(i+1,j)}) \tag{8.22}$$

$$\zeta^{(i+1,j+1)} = \zeta^{(i+1,j)} + \zeta^{(i,*)} + \lambda_\zeta \Delta t L_\zeta(u^{(i+1,j)}, w^{(i+1,j)}, \rho^{(i+1,j)}, p^{(i+1,j)}) \tag{8.23}$$

$$p^{(i+1,j+1)} = p^{(i+1,j)} + \lambda_p(u_x^{(i+1,j+1)} + w_z^{(i+1,j+1)}) \tag{8.24}$$

when $j > 0$, with

$$u^{(i+1,0)} = u^{(i,*)} \tag{8.25}$$

$$w^{(i+1,0)} = w^{(i,*)} \tag{8.26}$$

$$\rho^{(i+1,0)} = \rho^{(i,*)} \tag{8.27}$$

$$\zeta^{(i+1,0)} = \zeta^{(i,*)}, \tag{8.28}$$

where Δt is the magnitude of the time step, $q^{(i,j)}$ represents the value of a quantity q at the ith time step and the jth pseudo time step and $q^{(i,*)}$ represents the equilibrium value of q at the ith time step. The parameters λ_u, λ_w, λ_ρ, λ_ζ and λ_p relate to the assumed compressibility of fluid in pseudo time τ and the magnitude of a pseudo time step $\Delta\tau$, and are chosen to maximize the rate of convergence to equilibrium in the pseudo time co–ordinate τ. The system is judged to be in equilibrium when the divergence $u_x + w_z$ falls below a suitable threshold and the value of quantity q at the ith time step is then taken as its equilibrium value $q^{(i,*)}$.

Although Peyret and Taylor[36] give theoretical estimates for the best choice of the parameters λ_u, λ_w, λ_ρ, λ_ζ and λ_p, in practice these are best chosen by trial and error.

The artificial compressibility method does not dictate how the spatial derivatives in (8.20) – (8.23) should be calculated. It was decided to implement the scheme using finite differences calculated on a staggered grid (Peyret and Taylor[36]) to improve the stability of the first order derivatives.

The structure of the staggered grid was found to be crucial to the stability of the method, particularly the placement of ρ gridpoints in relation to u and w gridpoints. A typical configuration is shown in Figure 8.1. Letters indicate gridpoints and solid lines the boundary. Only by placing ρ gridpoints on the boundary and aligning them with lines of u and w gridpoints can (8.4) be integrated without boundary conditions.

The one minor complication to the scheme is that Equation (8.5) is imposed on the moving surface $z = \zeta(x,t)$. Since the motion of this surface is small in relation to the grid spacing, this equation is easily implemented by interpolation.

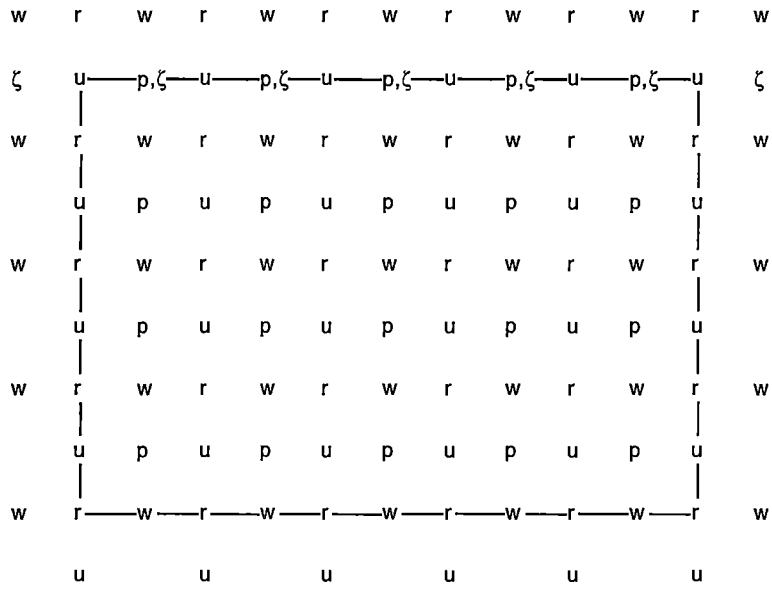

Figure 8.1: The Staggered Grid. This figure shows the structure of the staggered grid. Thick lines represent the boundary and letters indicate the points on the grid at which the corresponding primitive variable u, w, p, ρ or ζ is defined.

8.3 The Rectangular Basin

Given the obvious sensitivity of the problem, it was considered too ambitious to model the baffle experiments of the previous chapter. Instead it was decided to limit the study to a rectangular basin.

The basin was assumed to be of width l and depth h, with the upper left hand corner positioned at the origin. At the leftmost, rightmost, and upper boundaries, the boundary conditions were as described in section 8.1, with a zero stress condition imposed at each boundary. The motion was started from rest and forced on the lower edge $z = -h$, so that

$$w(x,-h,t) = \begin{cases} B_0/R_0 t \sin(\omega t)\sin(n\pi x/l) & \text{if } t \leq R_0 \\ B_0 \sin(\omega t)\sin n\pi x/l & \text{if } t > R_0 \end{cases} \tag{8.29}$$

$$u_z(x,-h,t) = 0, \tag{8.30}$$

where B_0 represents the amplitude of the forcing and R_0 determines the time scale on which the motion is "ramped up" from rest.

It was chosen to force the problem from the lower edge as this was found to be the most stable configuration of the system. Although this example is completely artificial, it does, nevertheless, serve to illustrate the effect of the nonlinear terms on the model.

The dimensions of the basin were chosen to loosely model the baffle experiment of the previous chapter, though for convenience, it was decided to fix the period at $T = 8s$ and vary the length of the basin until resonance was observed.

Upon experimenting with the linear model (8.8) – (8.11) it was found that the exact position of resonance was shifted slightly from that predicted in Section 7.3. This was attributed to small inaccuracies in the finite difference implementation, and lent support to the decision to not model the baffle experiment completely.

An accurate estimate of the resonant length of the basin was obtained with a standard bisection procedure. As the motion undergoes a sharp phase change at

resonance, the precise resonant period of the numerical model can be bracketed by observing the relative phases of the forcing and the induced motion. If N_x and N_z represent the number of pressure gridpoints of the staggered grid in the x and z directions respectively, then for the parameter values $N_x = 30$, $N_z = 30$, $h = 0.38m$, $T = 8s$, $\nu = 10^{-5}ms^{-2}$, $N = 1.45$, $B_0 = 0.001ms^{-1}$ and $R_0 = 40s$ it was found that resonance occurs for a basin of length approximately $l = 0.5855m$. These values loosely model the baffle experiment, except that ν has been increased by an order of magnitude to improve the stability of the numerical scheme. From the results of Section 7.3, this increase in viscosity can be expected to decrease the resonant amplitude by a factor of $\sqrt{10}$.

The motion was started from rest and the maximum fluid velocities in the basin recorded. These were observed to increase steadily, reaching a maximum of the order of $0.13ms^{-1}$ after approximately $946s$ of simulated time, representing a factor of 130 increase over the boundary forcing. The induced motion was observed to be $\pi/2$ out of phase with the boundary forcing, as expected under the linear theory.

Given the complexity of the system it is astounding that this result can be achieved numerically. Although these velocities are significantly smaller than the maximum predicted by the linear theory, this result clearly demonstrates the ability of the numerical model to reproduce, at least in part, the strongly resonant motions predicted by the model. It is expected that larger velocities could be generated by more accurately determining the resonant length l of the basin.

Figure 8.2 shows the horizontal and vertical velocity distributions predicted by the linear model at $t = 1002s$, shown in 3–D relief to emphasize the structure of the solution. The sinusoidal wave configurations predicted by the linear theory can be clearly seen.

In contrast, when the basin was modelled with the fully nonlinear model (8.1) – (8.7), resonance was not observed.

To investigate this further, nonlinear terms were selectively re–introduced

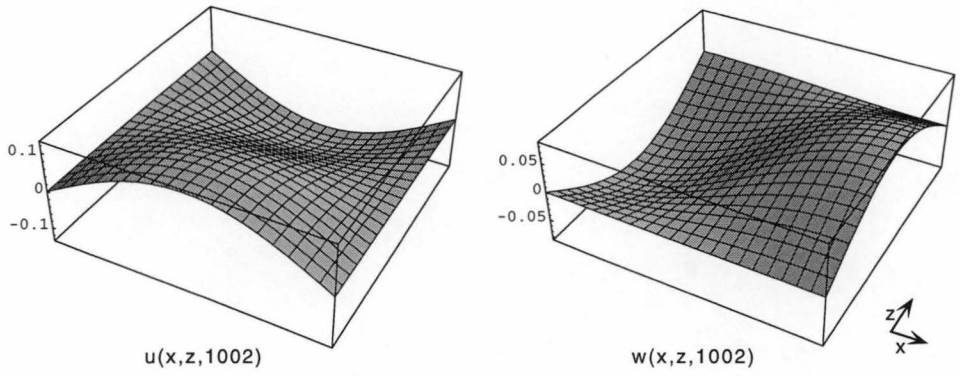

Figure 8.2: Modelling the rectangular basin with the linear model.

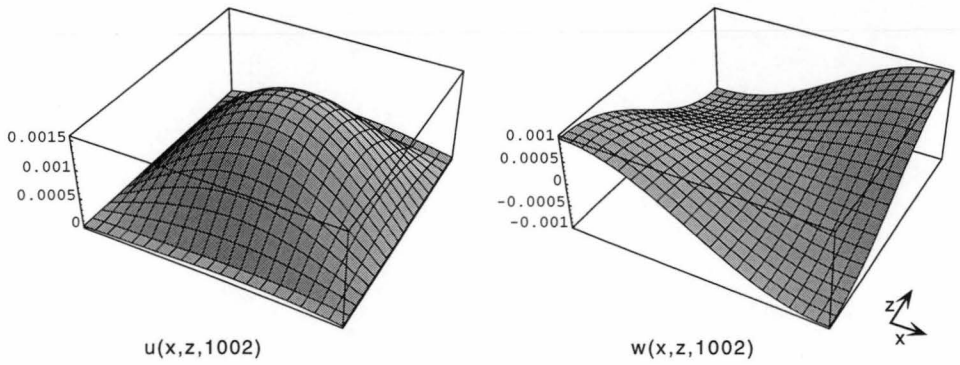

Figure 8.3: Modelling the rectangular basin with the linear model but imposing the nonlinear boundary conditions (8.8) – (8.11) at the surface.

to the linear model to determine those terms that had the greatest effect on resonance. It was found that the discrepancy in the two results could be almost entirely accounted for by augmenting the linear model with the nonlinear surface conditions (8.5) – (8.7). Furthermore, it was found that within condition (8.5), the effect of the term $u\zeta_x$ was negligible.

Figure 8.3 shows the velocity distributions corresponding to those depicted in Figure 8.2, as generated by the linear model with the nonlinear conditions (8.5) – (8.7) imposed at the surface. The maximum amplitude of the motion of the free surface was $0.0012m$.

Comparing this solution with Figure 8.2, it can been seen that with the addition of the nonlinear surface conditions the linear model admits an entirely different mode of vibration, thereby avoiding the strongly resonant motions of the strictly linear model. The motion induced at the free surface is of the order of millimetres, and so superficially it would appear that the rigid lid approximation is valid. But by its very nature, resonance motion is extremely sensitive to the dimensions of the basin, and so it is not surprising that it is also sensitive to the precise form of the boundary conditions.

Stigebrandt[43] has proposed the breaking of internal tides as a means of energy dissipation. No evidence to support Stigebrandt's propsoal was found in this study.

8.4 The Shelf Experiment

The nonlinear and linear models were also applied to the shelf experiment of Chapter 7. Unlike the rectangular basin, in this case the two models were found to be in excellent agreement.

The finite difference methodology described in the preceding sections is easily extended to a shelf topography by introducing the transformation

$$r = x \qquad s = z/h(x), \tag{8.31}$$

to map the shelf to a rectangular basin. Although this transformation complicates the form of the model, the basic structure of the finite difference scheme remains the same. This transformation implicitly requires that $h(x)$ be twice differentiable. For modelling the shelf experiment, $h(x)$ was represented by a linear spline and it was assumed that $h''(x) \equiv 0$. This is equivalent to replacing the non–differentiable points of $h(x)$ with smooth arcs that are of a scale too small to be resolved by the finite difference grid.

The boundary conditions were taken as follows. On the bottom, a zero flux

condition was applied in conjunction with a zero slip condition frictional condition, represented as

$$u(x, h(x), t) = 0, \tag{8.32}$$

$$w(x, h(x), t) = 0, \tag{8.33}$$

while at the two ends the fluid was assumed to satisfy the zero stress conditions

$$w_x(0, z, t) = 0, \tag{8.34}$$

$$w_x(l, z, t) = 0. \tag{8.35}$$

At the rightmost end a zero flux condition was imposed

$$u(l, z, t) = 0, \tag{8.36}$$

while the action of the wedge was modelled as

$$u(0, z, t) = \begin{cases} B_0/R_0 t \sin(\omega t) F(z) & \text{if } t \leq R_0 \\ B_0 \sin(\omega t) F(z) & \text{if } t > R_0 \end{cases} \tag{8.37}$$

where

$$F(z) = \begin{cases} 0 & \text{if } z \leq H_0 \\ 1 & \text{if } z > H_0 \end{cases} \tag{8.38}$$

and H_0 represents the depth the wedge protrudes into the tank, B_0 represents the amplitude of the forcing and R_0 determines the time scale on which the motion is "ramped up" from rest. These conditions are analogous to those used in section 7.2, except for the representation of the wedge.

In this case it was found that the results of the linear and nonlinear models are almost identical. Furthermore, in spite of the minor difference in the representation of the wedge, these solutions were found to be in excellent agreement with those found in section 7.2.

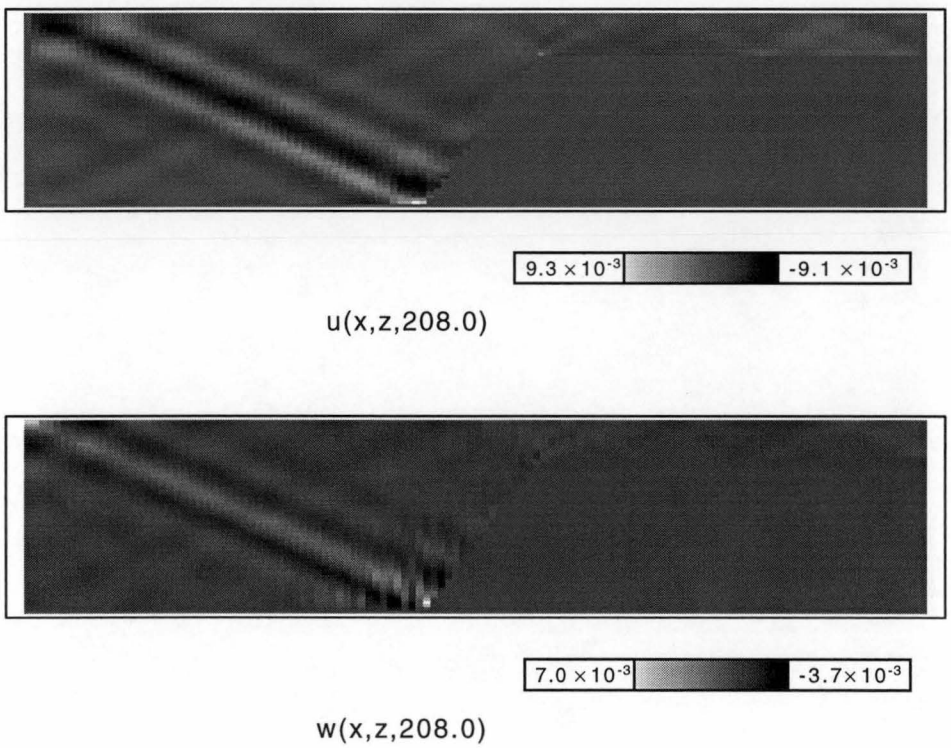

Figure 8.4: Velocity distributions predicted by the fully nonlinear model for the shelf experiment at $t = 208.0s$.

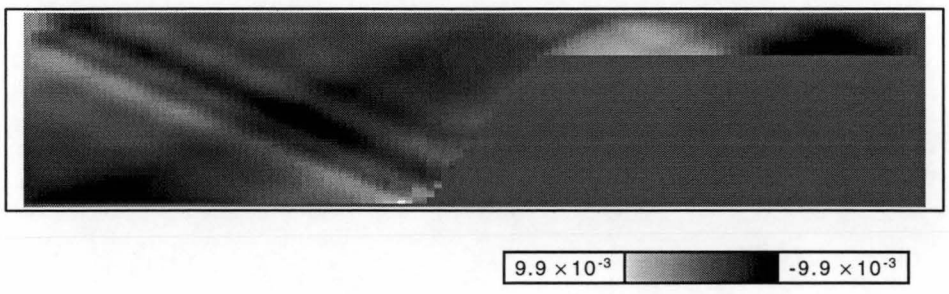

Figure 8.5: Velocity distributions predicted by the fully nonlinear model for the shelf experiment at $t = 210.6s$.

Figures 8.4 and 8.5 depict the horizontal and vertical velocities predicted by the fully nonlinear model for $t = 208.0s$ and $t = 210.6s$ with for $N = 1.41s^{-1}$, $\omega = 0.6s^{-1}$, $\nu = 10^{-5}m^2s^{-1}$, $B_0 = 0.004ms^{-1}$ and $R_0 = 40s$. Again, it was found necessary to inflate ν to improve the stability of the scheme. Note the instability in w at the base of the slope. This was attributed to the low viscosity and the limited resolution of the finite difference grid.

These two figures correspond precisely with the real and imaginary components of the solution found of Section 7.2 (see Figure7.3), and compare favourably with the velocity distributions derived from this solution. The strong diagonal features present in Figure7.3 can be clearly seen in Figures 8.4 and 8.5.

There are two possible explanations as to why resonance is observed in the fully nonlinear model for the case of the shelf, but not the rectangular basin. For the shelf the amplitude of the resonance is considerably smaller than that for the basin, correspondingly the nonlinear terms will be of less effect and the linearized model will represent a more accurate approximation for the shelf than the rectangular basin. Yet also, it was noted in Section 7.2 that for the shelf the resonance can be expected to be robust to variations in the dimensions of the tank. This may in turn translate to a degree of robustness to the form of the surface boundary condition.

Regardless, the most important conclusion to be drawn from the results of this chapter is that, although the presence of a "nearly closed" characteristic circuit appears to be a necessary condition for the existence of resonance, it does not constitute a sufficient condition. Thus it is not possible to determine whether a resonant solution will be observed merely from an examination of characteristics.

8.5 Summary

This chapter has demonstrated that for strongly resonant motions the strictly linear model of internal tide motion breaks down, and it becomes necessary to

introduce a nonlinear boundary condition at the free surface. For this nonlinear model, the existence of a characteristic circuit does not necessarily imply the existence of resonant solutions.

Chapter 9

Summary

Overall, this work supports the conjecture of Cushman–Roisin *et al.*[17] that the existence of characteristic circuits implies resonance. However, it has also been demonstrated that in the strongly resonant case the linear theory breaks down, and the large amplitude motions predicted by the models are not observed.

Chapter 4 completely characterized the behaviour the inviscid model (3.1) on closed basins. It was seen that for topographies for which there exist an uncountable number of characteristic circuits, there exist boundary conditions for which the time independent inviscid model (3.1) has no solution. It was shown, for a rectangular basin at least, that these instances correspond to resonant internal tide motion, and that resonant internal tide motions share many of the properties of damped simple harmonic motion. Invoking the structural stability of the corresponding viscous model, it was argued that the condition of an uncountable number of characteristic circuits could be considerably weakened. This conclusion was later supported by the numerical simulations of Chapter 7. The primary shortcoming of this theory is that although the existence of resonance solutions can be detected by examining characteristics, the method yields no estimate of the magnitude of the resonance.

In Chapter 7 the predictions of the linear models were compared with the re-

sults of laboratory experiments. For the shelf experiment, the agreement between model and data was found to be quite poor. This was attributed to the difficulty of modelling the external forcing, and served to highlight the sensitivity of the problem. These results suggest that the geometry simplifying assumptions often invoked in the treatment of such problems may be inappropriate. The baffle experiment was found to support the predictions of the linear theory for the weakly resonant case. But the extremely large amplitude resonant motions predicted by the linear theory were not observed, suggesting the need for a nonlinear model.

A nonlinear model was examined in Chapter 8, where it was seen that in the strongly resonant case, the common "Rigid Lid" approximation beaks down and a more accurate nonlinear condition must be applied at the surface.

In the course of this study, several new theoretical devices have been developed. C–conformal mapping has proven to be a useful tool with both theoretical (Chapter 4) and practical (Chapter 5) applications. Furthermore, unlike their classical counterparts, for many problems an appropriate c–conformal map may be easily generated with a simple numerical procedure. Chapter 6 developed a new family of solution procedures based on the principle of c–analytic continuation. These procedures represent a natural extension of the Fourier series methods commonly used by other authors, a show much promise.

Bibliography

[1] P. G. Baines. The reflexion of internal/inertial waves from bumpy surfaces. *Journal of Fluid Mechanics*, 46:273–291, 1971.

[2] P. G. Baines. The generation of internal tides by flat bump topography. *Deep–Sea Research*, 20:179–205, 1973.

[3] P. G. Baines. On internal tide generation models. *Deep–Sea Research*, 29(3A):307–338, 1982.

[4] George Blumen and Kumei Sukeyuki. On invariance properties of the wave equation. *Journal of Mathematical Physics*, 28(2):307–318, Febuary 1987.

[5] R. P. Boas. *Invitation to Complex Analysis.* Random House, New York, 1987.

[6] K. H. Brink. On the effect of bottom friction of internal waves. *Continental Shelf Research*, 8(4):397–403, 1988.

[7] C. Canuto, M. Y. Hussaini, A. Quarteroni, and T. A. Zang. *Spectral Methods in Fluid Dynamics.* Springer–Verlag, 1988.

[8] G. F. Carrier, M. Krook, and C. E. Pearson. *Functions of a complex variable.* McGraw Hill, 1966.

[9] W-S Chuang and D-P Wang. Effects of a density front on the generation and propagation of internal tides. *Journal of Physical Oceanography*, 11:1357–1374, 1981.

[10] A. J. Clarke and K. H. Brink. The response of stratified, frictional flow of shelf and slope waters to fluctuating large–scale, low–frequency, wind forcing. *Journal of Physical Oceanography*, 15:439–453, 1985.

[11] David L. Colton. *Solution of boundary value problems by the method of integral operators.* Pitman Publishing Limited, 1976.

[12] David L. Colton. *Analytic Theory of Partial Differential Equations.* Pitman Publishing Limited, 1980.

[13] P. D. Craig. Numerical modelling of internal tides. In J. B. Noye, editor, *Numerical Modelling — Applications to Marine Systems*, pages 107–122. Elsevier, Amsterdam, 1987.

[14] P. D. Craig. Solutions for internal tide generation over coastal topography. *Journal of Marine Research*, 45:83–105, 1987.

[15] P. D. Craig. A numerical study of internal tides on the australian northwest shelf. *Journal of Marine Research*, 46:59–76, 1988.

[16] P. D. Craig. Incorporation of damping into internal wave models. *Continental Shelf Research*, 11(6):563–577, 1991.

[17] B. Cushman-Roisin, V. Tverberg, and E. G. Pavia. Resonance of internal waves in fjords: A finite–difference model. *Journal of Marine Research*, 47:547–567, 1989.

[18] B. de Young and S. Pond. The nternal tide and resonance in indian arm, british columbia. *Journal of Geophysical Research*, 92(C5), 1987.

[19] B. A. Finlayson. *The Method of Weighted Residuals and Variational Principles.* Academic Press, 1972.

[20] P. R. Garabedian. *Partial Differential Equations.* John Wiley and Sons, 1964.

[21] A. Gill. *Atmosphere–Ocean Dynamics*, volume 30 of *International Geophysics Series.* Academic Press, 1982.

[22] D. Gottlieb and S. A. Orszag. *Numerical Analysis of Spectral Methods: Theory and Applications.* SIAM, 1977.

[23] D. G. Hurley. A general method for solving steady state internal gravity wave problems. *Journal of Fluid Mechanics*, 56:721–740, 1972.

[24] A. Jeffrey and T. Taniuti. *Non–Linear Wave Propogation.* Academic Press, 1964.

[25] D. S. Jones. *Generalised Functions.* McGraw Hill, 1966.

[26] C. Lanczos. *Applied Analysis.* Prentice–Hall, 1957.

[27] L. D. Landau and E. M. Lifschitz. *Fluid Mechanics.* Pergammon Press, 1959.

[28] L. H. Larsen. Internal waves incident upon a knife edge barrier. *Deep–Sea Research*, 16:411–419, 1969.

[29] P. D. Lax. *Hyberbolic Systems of Conservation Laws and the Mathematical Theory of Shock Waves.* SIAM, 1973.

[30] P. H. LeBlond and L. A. Mysak. *Waves in the Ocean.* Evsevier, 1978.

[31] M. J. Lighthill. Group velocity. *Journal of the Institute for Mathematics and its Applications.*, 1(1), 1965.

[32] M. J. Lighthill. On waves generated in dispersive systems by travelling forcing effects, with applications to the dynamics of rotating fluids. *Journal of Fluid Mechanics*, 27, 1967.

[33] M. J. Manton and L. A. Mysak. Construction of internal wave solutions via a certain functional equational. *Journal of Mathematical Analysis and Applications.*, 35:237, 1971.

[34] D. E. Mowbray and B. S. H. Rarity. A theoretical and experimental investigation of the phase configuration of internal waves of small amplitude in a density stratified liquid. *Journal of Fluid Mechanics*, 28:1–16, 1967.

[35] M. N. Özişik. *Boundary Value Problems of Heat Conduction.* International Textbook Company, Scanton, Pennsylvania, 1986.

[36] R. Peyret and T. D. Taylor. *Computational Methods for Fluid Flow.* Springer–Verlag, 1983.

[37] S. Pond and G. L. Pickard. *Introductory Dynamical Oceanography.* Pergammon Press, 1991.

[38] S. J. Prinsenberg, W. L. Wilmot, and Maurice Rattray, Jr. Generation and dissipation of coastal internal tides. *Deep–Sea Research*, 21:263–281, 1974.

[39] Maurice Rattray, Jr. On the coastal generation of internal tides. *Tellus*, 22(54-62), 1960.

[40] Maurice Rattray, Jr., Juraj. G Dworski, and Paavo. E. Kovala. Generation of long internal waves at the continental slope. *Deep–Sea Research*, 16:179–195, 1969.

[41] H. Sandstrom. On topographic generation and coupling of internal waves. *Geophysical Fluid Dynamics*, 7:231–270, 1976.

[42] E. A. Spiegel and G. Veronis. On the boussinesq approximation for a compressible fluid. *Astrophysical Journal*, 131:442–447, 1960.

[43] A. Stigebrandt. Vertical diffusion driven by internal waves in a sill fjord. *Journal of Physical Oceanography*, 6:486–495, 1976.

[44] A. N. Tikhonov and V. Y. Arsenin. *Solutions of Ill–Posed Problems.* John Wiley and Sons, 1977.

[45] V. Tverberg, B. Cushman-Roisin, and H. Svendsen. Modelling of internal tides in fjords. *Journal of Marine Research*, 49:635–658, 1991.

[46] I. N. Vekua. *Generalized Analytic Functions.* Pergammon Press, 1962.

[47] C. Wunsch. Progressive internal waves on slopes. *Journal of Fluid Mechanics*, 35(1):131–144, 1969.

Appendix A

Generating C-conformal Maps

This appendix contains the *Mathematica* scripts Map.m and SineMap.m used to create the c–conformal maps depicted in Figures 5.9 and 5.10. Map.m contains the generic code used to calculate the mapping, and SineMap.m calls Map.m with the appropriate parameters to reproduce Figure 5.9.

This implementation is designed to illustrate the algorithm described in Section 5.2, and is actually quite slow largely as a result of the way in which *Mathematica* represents lists. Re–implementing the algorithm in *Common Lisp* was found to yield a performance increase of several orders of magnitude.

```
(* SineMap.m
   Example demonstrating the use of Map.m. Generate a c-conformal map
   for a sine ridge topography. *)

c=0.8;
H1 = 1;
H2 = 0.4;
X1 = 0.2;
X2 = 0.8;

hs[x_]=(H2 + H1 + (H2-H1) Sin[Pi/2 * (2 x - (X1+X2))/(X2 - X1)])/2

h[x_]:=-H1          /; x <= X1
h[x_]:=-N[hs[x]]    /; X1 <= x <= X2
h[x_]:=-H2          /; x >= X2

h'[x_]:=0           /; x <= X1
h'[x_]:=-N[hs'[x]]  /; X1 <= x <= X2
h'[x_]:=0           /; x >= X2

(* Calculate points at which h[x] changes form sub to supercritical or
   vice versa. *)
criticalPts=x /. {FindRoot[h'[x] == c, {x, 0.1,0.4}],
                  FindRoot[h'[x] == c, {x, 0.6,0.9}]};

(* Read Map.m *)
<<Map.m

(* Generate the kernel for x in the range [-3,2.2] taking steps of
   0.02, with h[x] attaining its maximum at 0.8. *)

calcF[0.8,-3,2.2,0.02];


(* Display.
   This code generates the two grids used to display the transform *)
stepGrid[x0_,x1_,x2_,dx_,z0_,z1_,z2_,dz_]:=
    Join[
        Table[{
              If[z >= z1,
                   x0 + t (x2-x0),
                   x0 + t (x1-x0)],
              z},
              {z,z0,z2,dz}],
        Table[{x,
              If[x <= x1,
                   z0 + t (z2 - z0),
                   z0 + t (z1 - z0)]},
              {x,x0,x2,dx}]]

grid=stepGrid[0,2.0,2.0,0.1,0,-0.8,-0.8,-0.05];

(* Show grid in transformed domain *)
ParametricPlot[Evaluate[grid],{t,0,1},Axes->False,AspectRatio->Automatic];

grid1=Map[invcConformal,grid];

(* Show inverse image of grid *)
ParametricPlot[Evaluate[grid1],{t,0,1},Axes->False,AspectRatio->Automatic];
```

```
(* Map.m
   This file implements the explicit stepping algorithm for generating
   c-conformal maps for shelf regions.*)


(* Define some constants.
   linearConst is used to remove collinear points form the spline.*)
$RecursionLimit = 2000;
$linearConst = 10^-10;


(* These functions do the linear interpolation.
   linInterp does the basic linear interpolation and getF determines
   which points form fdata to use in the interpolation process *)
linInterp[x_,{{x1_,y1_},{x2_,y2_}}] :=
                        ((x-x1) y2 + (x2-x) y1)/(x2-x1);


getF[x0_]:=Block[{pos},
            (* Get position in fdata needed for interpolation *)
            pos = First[First[Position[fdata, {x_,y_} /; x > x0, 1,1]]];
            (* Do linear interpolation step *)
            linInterp[x0,Take[fdata,{pos-1,pos}]]];


(* These functions are used to add data pts to the spline
   representation of f. prependPt and appendPt only add a point if it
   is not collinear with the first/last two pts of fdata, if it is
   they do a replace instead. *)


collinear[{x1_,y1_},{x2_,y2_},{x3_,y3_}]:=
              Abs[(x3-x1)/(x3-x2) * (y3 - y2) - (y3 - y1)] < $linearConst;


prependPt[pt_]:=If[collinear[pt,fdata[[1]],fdata[[2]]],
                  fdata[[1]] = pt,
                  PrependTo[fdata,pt]];


appendPt[pt_]:=If[collinear[pt,fdata[[-1]],fdata[[-2]]],
                  fdata[[-1]] = pt,
                  AppendTo[fdata,pt]];



(* mkTriple is used to generate the triples from the xs *)

mkTriple[x_]:={x,x+h[x]/c,x-h[x]/c};


(* inK[x] - checks to see if x is in the known interval K.
   K is stored as a global in the form of a list. *)

inK[x_]:= K[[1]] <= x <= K[[2]];


(* The distance function *)
dist[{x1_,x2_},{x_,a_,b_}]:=If[a < x1, x1-a,b-x2];
```

```
tripleOrder[t1_,t2_]:= dist[K,t1] < dist[K,t2];


extendK[{}]:=fdata;
extendK[triples_List]:=Block[{triple},

      (* Determine which triple to extend with *)
      triple = First[
                  Sort[
                    Cases[triples, {x_,a_,b_} /; inK[a] || inK[b]],
                    tripleOrder[#1,#2]&]];
      (* Do the extension *)
      extendOnce[triple];

      (* Do rest *)
      extendK[DeleteCases[triples,triple,1]]
      ];



extendOnce[{x_,a_,b_}]:=If[Abs[h'[x]] <= c,
                           (* Boundary is subcritical *)
                           subExtend[x,a,b],
                           (* Boundary is supercritical *)
                           superExtend[x,a,b]];

(* Do a supercritical extension *)

superExtend[x_,a_,b_]:=Block[{fa,fb},
        If[inK[a],
          (* Extend to the right *)
          (  fa = getF[a];
             fb = rightR0 - fa;
             appendPt[{b,fb}];
             rightS0 = fa - fb;
             K[[2]] = b;
          ),

          (* Extend to the left *)
          (  fb = getF[b];
             fa = leftR0 - fb;
             prependPt[{a,fa}];
             leftS0 = fa - fb;
             K[[1]] = a;
          )]];


(* Do a subcritical extension *)

subExtend[x_,a_,b_]:=Block[{fa,fb},
        If[inK[a],
          (  fa = getF[a];
             fb = fa - rightS0;
             appendPt[{b,fb}];
             rightR0 = fa + fb;
             K[[2]] = b;
          ),
          (  fb = getF[b];
             fa = leftS0 + fb;
             prependPt[{a,fa}];
```

```
            leftR0 = fa + fb;
            K[[1]] = a;
          )]];

(* Calculate the kernel.
   This function puts it all together to calculate the kernel. *)

calcF[xm_,xmin_,xmax_,step_]:=Block[{xL,xR,triples,xs},


      xL = xm+h[xm]/c;
      xR = xm-h[xm]/c;

      (* Initialize some global vars *)
      K=S={xL,xR};
      rightS0 = leftS0 = 2 h[xm]/c;
      rightR0 = leftR0 = 2 xm;

      fdata={{xL,xL},{xR,xR}};

      (* Generate the list {x1,x2, ... xn} and the list of triples *)
      xs=DeleteCases[
                  Join[criticalPts,
                      Table[x,{x,xmin,xmax,step}]],
                  xm];

      T=Map[mkTriple,xs];
      extendK[T];


      (* Construct the kernel and its inverse *)
      f[t_]=Interpolation[fdata,InterpolationOrder->1][t];
      invf[t_]=Interpolation[
                  Map[Reverse,fdata],InterpolationOrder->1][t];

      ];



(* c-conformal transform and its inverse *)
cConformal[{x_,z_}]:=Block[{fp,fm},
                    fp=f[x+z/c];
                    fm=f[x-z/c];
                    {fp + fm, c (fp-fm)}];



invcConformal[{r_,s_}]:=Block[{fp,fm},
                    fp=1/2 invf[(r+s/c)/2];
                    fm=1/2 invf[(r-s/c)/2];
                    {fp + fm, c (fp-fm)}];
```

Appendix B

Internal Collocation Method

This appendix contains the *Mathematica* scripts IAtan.m and IColl.m. The script IColl.m solves the viscous internal tide problem on a basin with the internal collocation method described in Section 6.3, and IAtan.m calls IColl.m with the appropriate parameters to reproduce the solution of Figure 6.1.

The implementation makes heavy use of *Mathematica*'s symbolic algebra capabilities. To re–implement this algorithm in *Fortran* or *C* would require that the user provide the necessary derivatives of the trial and forcing functions which *Mathematica* generates automatically. The efficiency of the *Mathematica* implementation is vastly improved through the use of Terry Robb's "Optimize" package, which perform common subexpression optimization on arbitrary *Mathematica* expressions. This package is available by ftp from *MathSource* (`ftp mathsource.wri.com`), as numbered item 0205–939.

```
(* IAtan.m
   Solve the viscous internal tide problem by internal collocation.
   This script contains the user definition of the operator L and
   other constants

        Bf              Bouyancy Freq
        period          Period
        om              Angular Freq
        Nu              Viscosity
        l               Length Basin

        Nm              Num coeffs in x expansion
        Nn              Num coeffs in z expansion

  Eqn to be solved is defined by L(Psi)=0

*)


Bf=1.456;
period=9.5;
om=N[2*Pi/period];
nu=2 * 10^-5;
l=2.0;



Nm=42;
Nn=20;
CoeffFile="case3.dat";
SolveMode="Load";

(* Define the lower boundary *)
hc1=-0.6;
hc2=0.05;
hc3=8;
hc4=1.0;
hs[x_]=N[hc1-hc2*2/Pi*ArcTan[hc3*(x-hc4)]];

(* Define the differential operator L *)
L[f_]:=(Bf^2-om^2)*D[f,{x,2}]-om^2*D[f,{z,2}]-I*om*nu*D[f,{z,4}];



(* The definition of the trial and forcing functions. *)

trialPsi[x_,z_,m_,n_]=N[Sin[m*Pi*x/l]*((-1)^n*n*Pi/2*((z/h[x])^3-(z/h[x]))-Sin[
                                                    n*Pi*z/h[x]])];

B[x_,z_]=N[Sin[x*Pi/l]*((3*z)/(2*h[x])-((z/h[x])^3)/2-1)];


(* Call generic component *)

<<IColl.m
```

```
(* IColl.m
   Generic component of program implementing internal collocation
   procedure. Relies on Terry Rob's excellent optimization package,
   Optimize.m, available by anonymous ftp from mathsource.wri.com.
*)


(* Load Terry Rob's excellent package *)
Needs["Optimize`"];

(* Processing this message takes megabytes. Dumb *)
Off[LinearSolve::luc];


(*
   Now define the residuals, one for the trial functions and one for
   the forcing. *)

Ltrial[x_,z_,m_,n_]=L[trialPsi[x,z,m,n]];


Lforce[x_,z_]:=Optimize[L[B[x,z]]];


(*
  This function calculates the matrix A and vector B used by the
  collocation process.  We actually calculate a whole row of the
  matrix, do common subexpression elimination then generate the whole
  matrix.  This may sound like a pain, but gives a massive speed win
  overall, even without compilation. (compilation strikes a problem,
  cause we are working with lists. *)



calcEqs[A_,B_]:=Module[{row,x,z},

  row[x_,z_]:=Optimize[
                Flatten[Table[Ltrial[x,z,m,n],{m,Nm},{n,Nn}]]];

  h[x_]=hs[x];
  A = Flatten[
          Table[(
                Print["stage ",i," ",j];
                x=i*l/(Nm+1);
                z=j*h[x]/(Nn+1);
                row[x,z]),
                {i,Nm},{j,Nn}],
          1];

  B = Flatten[
          Table[(
                x=i*l/(Nm+1);
                z=j*h[x]/(Nn+1);
                -Lforce[x,z]),
                {i,Nm},{j,Nn}]];
];
```

```
(*
   This code does the job.  If SolveMode is "Load", tries to load soln
   from CoeffFile instead of calculating it, otherwise soln is
   calculated from scratch and stored in CoeffFile. *)

If[SolveMode=="Load",
    (* then *)
      (Print["Loading Coeffs From ",CoeffFile];
      Soln=Get[CoeffFile];
      Print["Loaded"];),
    (* else *)
      (Print["Calculating Array Coeffs"];
      Module[{A,b},
            calcEqs[A,b];
            Print["Solving Linear System"];
                  Soln=LinearSolve[A,b];
                  Clear[A,b]];
      Print["Writing Soln to ",CoeffFile];
      Put[Soln,CoeffFile];
      Print["Finished"];)
];


(*
  Calculate Psi from its expansion in terms of the trial functions.
  rawPsi does all the work and is wrapped by Psi which tests if we are
  actually in the region or not. *)

showCoeffs[]:=Module[{cs},
      cs = Partition[Soln,Nn];
      {ListDensityPlot[Abs[cs],PlotRange->All],
      ListDensityPlot[Log[Abs[cs]],PlotRange->All]}];


Print["Compiling"];
Print["Psi"];
Psi = Compile[{{x,_Real},{z,_Real}},
       Optimize[
            B[x,z] +
            Chop[Soln] . Flatten[Table[trialPsi[x,z,i,j],{i,Nm},{j,Nn}]]]]
```

Appendix C

Boundary Collocation Method

This appendix contains the *Mathematica* script IAtan.m. This script solves the viscous internal tide problem on a basin with the boundary collocation method described in Section 6.6.3, to reproduce the solution of Figure 6.5.

The boundary collocation method itself is trivial to implement and can be expressed in a few short line of code. The bulk of the script arises from the need to calculate a suitable set of collocation points.

As in Appendix B, use is made of Terry Robb's "Optimize" package, which is available by ftp from *MathSource* (`ftp mathsource.wri.com`) as numbered item 0205–939.

```
(* BoundColl.m
   Solve the viscous internal tide problem for a basin with an Atan
   like lower boundary, using the boundary collocation technique based
   on the first stage of Craig's procedure.*)


(* Parameters
   Define the various constants used in the process. *)
Bf=1.456;
period=9.5;
w=N[2*Pi/period];
nu=2 10^-5;
c=Sqrt[w^2/(Bf^2-w^2)];



(* Representing the boundary.
   The lower boundary is represented as z=h[x], while bound[t] is a
   parametric representation of the lower boundary plus edges. *)

hc1=-0.6;
hc2=0.05;
hc3=8;
hc4=1.0;

h[x_]=N[hc1-hc2*2/Pi*ArcTan[hc3*(x-hc4)]];

bound[t_]:=Which[
            t < 0.25,           {0, 4 t h[0]},
            0.25 <= t < 0.75,   {4 (t-0.25), h[4 (t-0.25)]},
            t >= 0.75,          {2, 4 (1.0-t) h[2]}];


(* Trial functions and Forcing
   Define the trial functions and forcing function used in the
   collocation process. *)

L=2 - h[2]/c -h[0]/c;
p0=h[0]/c;

trial[n_][{x_,z_}]=N[Cos[n Pi (x+z/c-p0)/L] - Cos[n Pi (x-z/c-p0)/L]];

frc[x_]:=N[If[0 <x < 2,Sin[Pi x/2],0]];
force[{x_,z_}]=frc[x-z/c];

(* Boundary condition.
   BcBottom represents the boundary condition applied on the lower
   boundary while BcEdge is the boundary condition applied at the
   edges. *)

lambda[x_]=Together[Sqrt[I (w^2 +(2 w^2 -Bf^2) (h'[x])^2 + (w^2 - Bf^2) (h'[x])
                                                          ^4)/
              (nu w (1 + (h'[x])^2)) ]];

BcBottom[f_]:=D[f,z]/lambda[x] + f;
BcEdge[f_]:=f;
```

```
(* Load Terry Rob's optimization package *)
Needs["Optimize`"]

(* Calculating the Collocation Points.
   The collocation points or "knots", are calculatated as follows.
   First, using a simple bracketing procedure, calculate a list of all
   the of the roots of the first neglected trial function that lie on
   bound[t].  The requirednumber of collocation points are then chosen
   form this set by deleting points that are too close together. *)


(* getKnots
   Given a set of trial functions and a paramteric rep of the boundary,
   choose collocation points for which first neglected trial func is zero,
   removing knots near z=0 *)

getKnots[trial_,bound_,n_,{t0_,t1_,dt_}]:=
    DeleteCases[Map[bound,
                t /. multipleRoots[trial[n+1][bound[t]]==0,{t,t0,t1,dt}]],
                {x_,z_} /; RmKnotQ[{x,z}]];

(* RmKnotQ
   True if pt is too close to surface to be an unacceptable
   collocation point. *)

RmKnotQ[{x_,z_}]:=(z > -10^-8);


(* mkPairs
   Split a list into pairs.*)

mkPairs[lst_List]:=Transpose[{
                      Drop[lst,-1],
                      Drop[lst,1]}];


(* rBrack
   Bracket possible roots of f[x]==0, based on the partition part.*)

rBrack[f_,fd_,part_List]:=Select[mkPairs[part],
                          (N[f[#[[1]]] * f[#[[2]]]] <= 0 ||
                          N[fd[#[[1]]] * fd[#[[2]]]] <= 0)&];

(* multipleRoots
   Search the interval [x0, x1] for roots of eqn. *)

multipleRoots[Equal[lhs_,rhs_],{x_,x0_,x1_,dx_}]:=Module[{f,find},
  f=Function[Evaluate[x],(lhs - rhs)];
  find[{a_,b_}]:=Check[FindRoot[f[x]==0,{x,a,b}],Null];
  DeleteCases[Map[find,rBrack[f,f',Range[x0,x1,dx]]],Null]
  ];



(* Choosing the Collocation points.
   These functions remove uneeded collocation points from the list.
   Successively picks two closest points and removes the one for which
   the function f is a maximum. f is generally chosen as the second
   neglected trial function. *)
```

```
dist[pt1_,pt2_]:=Sqrt[Apply[Plus,(pt2-pt1)^2]];

minPos[lst_]:=Position[lst,Min[lst]];

rmClosest[f_,knots_,dists_,n_?Negative]:={};
rmClosest[f_,knots_,dists_,0]:=knots;
rmClosest[f_,knots_,dists_,n_]:=Module[{i,j,rm},
  {i,j} = First[minPos[dists]];
  rm=If[Abs[f[knots[[i]]]] < Abs[f[knots[[j]]]], j, i];
  rmClosest[f,Drop[knots,{rm}],Map[Drop[#,{rm}]&,Drop[dists,{rm}]],n-1]];

chooseKnots[f_,knots_,n_]:=Module[{dists},
  dists = DiagonalMatrix[Table[Infinity,{i,Length[knots]}]] +
              N[Outer[dist,knots,knots,1]];
  rmClosest[f,knots,dists,Length[knots]-n]];
```

```
(* Calculate the Collocation Points.
   allknots is a list of all possible knots, from this is selected
   knots, the subset used for the collocation. *)

allknots=getKnots[trial,bound,Nb,{0,1,1/(10*Nb)}];
knots=chooseKnots[trial[Nb+1],allknots,Nb];
```

```
(* Collocation.
   Arow and Brow form a single row of the matrix problem Ax=b that
   represents the collocation. *)

Arow[{x_,z_}]=Table[If[x == 0.0 || x == 2.0,
                          Evaluate[BcEdge[trial[n][{x,z}]]],
                          Evaluate[BcBottom[trial[n][{x,z}]]]],{n,Nb}];

Brow[{x_,z_}]=-If[x == 0.0 || x == 2.0,
                          Evaluate[BcEdge[force[{x,z}]]],
                          Evaluate[BcBottom[force[{x,z}]]]];

A=Map[Arow,knots];
B=Map[Brow,knots];

coeffs=LinearSolve[A,B];
Clear[A,B];
```

```
(* psi
   This code calculates the solution from the list of coeffs and the
   trial and forcing functions.  This is compiled and optimized for
   speed. *)

psi=Compile[{x,z},
  Optimize[
      force[{x,z}] +
        coeffs . N[Table[trial[n][{x,z}],{n,Nb}]]]]
```